Magnesium for biomedical applications as degradable implants : thermomechanical processing and surface functionalization of a Mg-Ca alloy

Olivier Jay

UNIVERSITY OF WATERLOO

UNIVERSITÉ GRENOBLE ALPES

THÈSE

Pour obtenir le grade de

DOCTEUR DE L'UNIVERSITÉ GRENOBLE ALPES

préparée dans le cadre d'une cotutelle entre l'*Université Grenoble Alpes* et l'*Université de Waterloo*

Spécialité : **Matériaux, Mécanique, Génie civil, Electrochimie**

Arrêté ministériel : le 6 janvier 2005 - 7 août 2006

Présentée par

« Olivier JAY »

Thèse dirigée par **« Patricia DONNADIEU »**
codirigée par **« Shahrzad ESMAEILI»**

préparée au sein des **Laboratoires « Laboratoire des Sciences et Ingénierie des Matériaux et des Procédés (SIMaP) » et «Multi-Scale Additive Manufacturing Laboratory (MSAM) »**

dans **les Écoles Doctorale « Ecole Doctorale Ingénierie - Matériaux Mécanique Energétique Environnement Procédés Production (I-MEP2) » et « PhD program of Mechanical & Mechatronics Engineering Department »**

Magnesium for biomedical applications as degradable implants: thermomechanical processing and surface functionalization of a Mg-Ca alloy

Thèse soutenue publiquement le **« 14 Décembre 2015 »**,
devant le jury composé de :

Mr Jean-Jacques BLANDIN
Directeur de recherches CNRS, Grenoble (Invité)
Mr Guy DIRRAS
Professeur, Université de Paris XIII (Président)
Mme Patricia DONNADIEU
Directeur de recherches CNRS, Grenoble (Directeur)
Mme Shahrzad ESMAEILI
Professeur, Université de Waterloo, Canada (Co-directeur)
Mr David FRABOULET
Ingenieur CEA (Représentant industriel)
Mme Anna FRACZKIEWICZ
Professeur, Ecole des Mines de Saint-Etienne (Rapporteur)
Mr Frédéric PRIMA
Professeur, Université de Paris (Rapporteur)

Abstract

Degradable implants for bone fixation have been of significant interest since the last decade. Among different materials, magnesium appears as a promising candidate due to its unique combination of properties. Magnesium is very well tolerated by the body and has a natural tendency for degradation. In addition, its low elastic modulus helps to reduce stress-shielding effect during bone healing. Mg-Ca alloys are particularly of interest for the additional processing and property benefits that Ca addition provides. The potential use of these alloys necessitates multi-faceted studies so that microstructures with an optimal compromise between mechanical properties and degradability kinetics are achieved. This work focuses on Mg-2wt.%Ca alloy and aims to provide a path for future optimization of the alloy for implant applications.

In this work a new bulk/surface processing approach is proposed: i.e. tailoring the bulk microstructure by thermomechanical treatments and surface functionalization by additive manufacturing. Hot rolling, extrusion and equal channel angular pressing (ECAP) have been used for bulk processing. The characterization results show that while different microstructural features (dislocations, twins, grain size) can account for the improvement in the mechanical strength, the improvement in the corrosion resistance appears as primarily affected by grain size and second phase microstructure. It is found that the severe plastic deformation induced by the ECAP process produces the finest grain structure and second phase particle distribution. This influence results from the dispersion of the second phase Mg2Ca and possibly a more stable oxide layer. The ECAP process also appears as the most effective method to improve the mechanical strength.

Surface modification is achieved by designing a surface patterning method that uses silver nanoparticle microdeposition to functionalize the material for antibacterial properties. The deposition is followed by a laser sintering process. A series of depositions are performed to achieve the desired deposition conditions and

a reproducible deposition line of 20 μm width and between few hundreds of nanometres and one micrometre thick. Profilommetry, SEM and TEM are used to characterize the silver deposition and the substrate microstructure. A finite element simulation has been conducted to describe the thermal effect of the laser treatment process. The modelling results show that the thermal impact from the laser sintering process extends deep into the substrate and thus needs to be controlled in order to avoid any evolution of the previously designed bulk microstructure. This model can then provide a basis to investigate the impact of different input parameters for further process optimization in future applications.

Acknowledgements

I would like to express my gratitude and sincerely thank all the people who have participated in the present work and allowed me to accomplish it.

First, I would like to thank my supervisors, Prof. Patricia Donnadieu, Prof. Shahzard Esmaeili, Prof. Jean-Jacques Blandin and Prof. Ehsan Toyserkani. This work would not have been possible without their guidance, assistance and support. Over these years, I had the great opportunity to work with them and discover various science frameworks based on theirs specialities.

I would also like to gratefully acknowledge my thesis examining committee members, Prof. Guy Dirras from "Université de Paris XIII", Mr. David Fraboulet from French Alternative Energies and Atomic Energy Commission, Mrs. Anna Fraczkiewicz from "Ecole des Mines de Saint-Etienne" and Mr. Frédéric Prima from "Université de Paris" for taking the time to review my thesis and provide valuable constructive insights.

I would like to acknowledge Prof. Julie Gough from the University of Manchester and Prof. Maria de Fátima G. da Costa Montemor from "Universidade Técnica de Lisboa" for their collaborations to this work.

I thank my fellow researchers for their many discussions around a cup of coffee which have helped me with this work, including, Souad Benrhaiem, Nicolas Sallez, Fanny Mas, Audrey Lechartier, Kitty Raner, Simon Langlais, Maxime Dupraz, Rozen Ivanov, Laurent Couturier, Saied Mahmoud, Hasan Naser, Eva Gumbmann, Li Hua Liao, Vahid Fallah, Brian Langelier, Ahmad Basalah, Elahe Jabari, Amir Azhari, Esmat Sheydaeian, Richard Liang, Farid Behzadian, Mihaela Vlasea, Evan Wheat, Daniel Prodan. I have spent such good times travelling between France and Canada and I particularly owe you this.

Finally, but most importantly, I would like to thank the International Doctoral School in Functional Materials (IDS FunMat) to have bring this international program at life.

A special thank you to the best family in the world: mine for being so supportive and patient with me especially my sister.

Table of contents

List of figures

List of tables

1. Résumé étendu en français

1.1 Contexte et objectifs

Chaque année, des millions de personnes sont sujettes à des fractures osseuses. Le nombre de ces patients est amené à croître en raison de l'accroissement de la longévité et de la popularité des sports extrêmes. Néanmoins, selon la localisation du trauma, les patients doivent recourir à différents types d'implants. Les implants peuvent ainsi être catégorisés selon leur application, par exemple : les prothèses (hanche, genou et épaule), les plaques et vis de fixation, les disques intervertébraux et les implants dentaires [1]. Dans ces catégories, il est possible de distinguer deux familles d'implants : les implants qui doivent rester en place afin d'assurer le bon fonctionnement de l'os traité (dispositif artificiel de remplacement) et les implants qui permettent de maintenir l'os et d'assurer le support des contraintes mécaniques durant le processus de reconstruction.

De nos jours, les implants de fixation sont réalisés à partir d'acier inoxydable, d'alliages à base de Cobalt et d'alliages de titane [2]. Des nuances spécifiques de ces matériaux ont été optimisées pour ce type d'application et peuvent assurer le support des contraintes mécaniques durant le temps de reconstruction. Cependant, des complications médicales peuvent survenir lors de l'utilisation d'implants réalisés avec ces matériaux : allergie au métal, phénomène de déviation des contrainte couramment appelé « stress-shielding » ou nécrose des tissus autour de l'implant [3]. De plus, dans la majorité des cas et plus particulièrement pour les patients d'un jeune âge, ces implants doivent être retirés après reconstruction de l'os [4]. Cette nouvelle opération fait encourir de nouveaux risques médicaux au patient et nécessite de nouveaux moyens humains et matériels [5]. L'utilisation de matériaux biodégradables est alors

une idée attractive pour le développement d'un nouveau type d'implant qui serait éliminé naturellement et ne nécessiterait plus de seconde opération chirurgicale.

Différents matériaux biodégradables ont été identifiés pour réaliser ce type d'implant, par exemple, des matériaux polymères tels que le polyglycolide, le polylactide et le polydioxanone [6]. Néanmoins, la majorité des matériaux polymères possèdent des propriétés mécaniques insuffisantes pour être utilisé comme un implant de fixation sujet à des contraintes mécaniques. Par exemple, le module élastique (important pour la rigidité) est environ dix fois plus petit que celui des os [7]. À la vue de cette caractéristique, les systèmes métalliques s'imposent. Cependant, un implant dégradable requiert au matériau métallique d'être dégradable et biocompatible. De plus, les produits de dégradation doivent eux aussi être bien tolérés par le corps humain. Il n'y a que peu de systèmes métalliques qui remplissent ces conditions. Le magnésium, avec une bonne tolérance par le corps humain (il est même recommandé d'avoir un apport journalier de 400 mg [8]) et sa tendance naturelle à la dégradation (i.e. sa faible résistance à la corrosion), apparait comme un candidat des plus prometteur. Edward C. Huse a utilisé des fils de ligatures dégradables en magnésium sur un patient en 1878 [9]. Depuis lors, malgré un rythme ralenti durant de nombreuses années concernant la recherche sur les alliages à base de magnésium comme matériau dégradable, la dernière décennie a montré d'important progrès dans ce thème de recherche.

En plus d'être bien toléré et d'être dégradable, les alliages de magnésium possèdent un module élastique (≈ 40 GPa) relativement proche de celui des os (≈ 20 GPa pour l'os cortical [10]). Grâce à cette similitude du module élastique, les implants en magnésium permettraient une meilleure répartition des contraintes durant le processus de reconstruction. Ainsi, le stress-shielding [11], qui peut être un problème majeur lors de la reconstruction d'un os, serait réduit. Aucun autre système métallique ne possède un tel avantage puisque tous les autres métaux possèdent un module élastique plus élevé. Cependant, la limite d'élasticité du magnésium pur est faible (≈ 20 MPa [12]) comparée à celle des os (≈ 120 MPa [13]). Il est ainsi préférable d'utiliser des alliages de magnésium qui peuvent posséder une limité d'élasticité plus élevée [14].

En effet, les propriétés mécaniques des dispositifs en magnésium sont habituellement améliorées par l'utilisation d'alliage de magnésium à la place de magnésium pur. Néanmoins, l'utilisation d'éléments d'alliage dans le cadre d'implants dégradables à base de magnésium possède deux inconvénients : premièrement, ces éléments d'alliage peuvent être toxiques pour le corps humain et deuxièmement, le taux de corrosion d'un alliage de magnésium est généralement plus élevé que celui du magnésium pur. La vitesse de dégradation pour un implant à base de magnésium dépendant de l'application elle-même : le temps de dégradation doit être compatible avec le processus de reconstruction. La Figure 1 illustre les conditions idéales pour la reconstruction d'un os avec, en parallèle, la dégradation graduelle d'un implant. Le temps de dégradation de l'implant dépend de multiples paramètres (taille de l'implant, localisation et caractéristiques du matériau) et est ainsi très variable. En plus du besoin d'une bonne correspondance avec le temps de reconstruction, il faut éviter que le dihydrogène relâché lors de la corrosion du magnésium forme de trop grosses bulles. Le contrôle de la vitesse corrosion est ainsi un point clef des implants dégradables à base de magnésium.

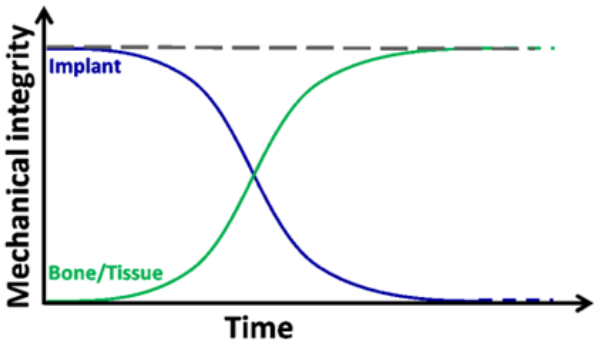

Figure 1 : Evolution de l'intégrité mécanique d'un implant dégradable au cours du processus de reconstruction, adapté de [15].

Les propriétés mécaniques des alliages de magnésium peuvent aussi être améliorées par des procédés thermomécaniques. Par exemple, cela peut être accompli par laminage à chaud ou par des procédés d'extrusion ce qui modifie la microstructure (taille de grain, texture, distribution de la seconde phase). L'impact des procédés thermomécaniques sur la corrosion a été considéré dans différents études [16] [17] [18] [19] [20]. Apparemment, la présence d'une seconde phase, la taille de grain et la texture influencent la vitesse de corrosion [16] [20]. Cependant, la possibilité de

contrôler la vitesse de corrosion par des procédés thermomécaniques est encore sujette à de nombreuses études. Ainsi, bien que le magnésium apparaisse comme le métal le plus prometteur pour réaliser des implants biodégradables, il nécessite encore d'être amélioré concernant ses propriétés mécaniques et son comportement à la corrosion avant de pouvoir être utilisé.

Il est important de noter que le traitement de surface est intéressant dans le cadre de l'amélioration d'un matériau en vue de la fabrication d'implants car la surface de l'implant est le premier domaine à être en contact avec l'environnement humain. Ainsi, un traitement de surface adéquat peut améliorer les réactions biologiques suite à l'implantation. Par exemple, l'argent peut être utilisé afin d'ajouter un effet antibactérien à l'implant [21], une fonctionnalisation particulièrement intéressante dans le cas présent en raison de l'intervention chirurgicale.

Le but général de ce projet est le développement de stratégies pour améliorer la microstructure interne et la surface du matériau pour développer un alliage de magnésium pour une utilisation en tant qu'implant biodégradable. Dans ce contexte, les voies d'amélioration seront centrées sur l'application de traitements thermomécaniques et la modification de la surface par une technique de fabrication additive sur un alliage de magnésium-calcium. Pour la présente thèse, il a été choisi de travailler avec un alliage de Mg-2pds.%Ca en raison de la biocompatibilité ainsi que des effets bénéfiques complémentaires du calcium [22] [23]. Les objectives de ce projet peuvent ainsi être décrit comme suit :

- Impact de trois procédés thermomécaniques sur les propriétés mécaniques et le comportement en corrosion de l'alliage sélectionné.
- Fonctionnalisation de la surface du matériau par un dépôt d'argent en utilisant une technique de fabrication additive.

Afin de réaliser le premier objectif, du laminage et de l'extrusion conventionnels, ainsi qu'un procédé non-conventionnel, i.e. l'extrusion coudée à aires égales (ECAE), ont été choisis. Le comportement mécanique et à la corrosion ont été évalués par des méthodes classiques : tests de micro-dureté, tests de compression, tests d'immersion, spectroscopie d'impédance électrochimique (SIE). Une étude multi-échelle de la microstructure a été réalisée par microscopie optique, microscopie électronique à

balayage (MEB) et microscopie électronique en transmission (MET). Ces investigations peuvent permettre de mettre en évidence un possible lien entre le design de la microstructure produite par les procédés thermomécaniques et l'amélioration des propriétés mécaniques et du comportement à la corrosion.

Pour réaliser le second objectif, une technique de fabrication additive, habituellement utilisée en microélectronique, utilisant une machine de microdéposition (LAMM) [24] a été utilisée afin de déposer des nanoparticules d'argent à la surface de l'alliage. La déposition a été suivie d'un traitement thermique par laser. Cette méthode de déposition dispose de nombreux paramètres à régler, ainsi, une première phase de test a été nécessaire afin d'optimiser les conditions de dépôt et d'obtenir un pattern régulier à la surface du matériau. Ces conditions optimales ont été déterminées en réalisant des images par MEB et par profilométrie. La microstructure des échantillons patternés et la qualité de l'interface dépôt-substrat ont été caractérisées par observation MEB et TEM sur des sections transverses au dépôt et au substrat. L'impact thermique du traitement laser a été modélisé en utilisant le logiciel COMSOL Multiphysics. Le but de cette simulation étant de définir de futures conditions de traitement laser (intensité, vitesse) afin d'optimiser l'impact de ce traitement thermique sur le substrat et la déposition de nanoparticules d'argent.

1.2 Impact des traitements thermomécaniques

1.2.1 Microstructure et propriétés mécaniques

Les paramètres microstructuraux les plus pertinents concernant les propriétés mécaniques sont la taille de grain, la texture, la densité de dislocation, la morphologie et la densité des précipités. Grâce aux caractérisations par microscope optique, SEM et TEM, certains de ces paramètres ont pu être déterminés. Le Tableau 1 récapitule les principales caractéristiques microstructurales et les propriétés mécaniques pour l'échantillon brut de coulée et pour les échantillons après traitements thermomécaniques.

Tableau 1 : Caractéristiques microstructurales des échantillons après traitements thermomécaniques et leur propriétés mécaniques associées.

	Taille de grain	2de phase	Texture	Dureté	Résistance maximale (MPa)	Déformation à rupture
Brut de coulée	Plusieurs mm	Squelette connecté	-	40 ± 7	186	0.14
Laminé à 400 °C	≈ 25 µm + macles	Squelette fragmenté	Fibre	64 ± 7	-	-
Extrudé à 200 °C	Plusieurs mm + macles	Squelette étiré et fragmenté	-	70 ± 6	277	0.02
Extrudé à 400 °C	≈ 8 µm	Fragments + particules	Faible	46 ± 8	359	0.14
ECAE	≈ 2 µm	Particules [100–600 nm]	Faible	72 ± 3	325	0.20

La grande taille de grain de l'échantillon brut de coulée est une caractéristique typique d'une microstructure de solidification et est compatible avec la faible dureté mesurée. Il est possible de noter que tous les traitements thermomécaniques ont permis d'augmenter la dureté du matériau. Concernant l'échantillon laminé, différents mécanismes peuvent expliquer l'augmentation de la dureté. Les macles sont connues pour réduire la mobilité des dislocations dans le plan basal [25]. Ainsi, la présence de macles peut contribuer à l'augmentation de la dureté. L'échantillon laminé présente aussi une forte texture avec les plans basals parallèles au plan de laminage qui correspond à la surface d'indentation. Cela a aussi pu contribuer à augmenter la dureté, en effet, il a été reporté que les plans basals sont plus durs que les autres plans [26]. L'échantillon laminé a aussi subi un court recuit qui peut avoir permis un processus de recristallisation. Cependant, le recuit n'était que de 2 min et aucun recuit n'a été effectué après la dernière passe de laminage. Il peut ainsi être envisagé que d'autres effets peuvent aider à cette augmentation de dureté.

L'échantillon extrudé à 200 °C ne montre aucune recristallisation. Cet échantillon possède la plus haute valeur de dureté et la plus faible déformabilité. Ainsi, dans ce cas, l'écrouissage peut être considéré comme un facteur majeur dans l'augmentation de la dureté. Grâce aux observations par MEB, il a aussi été noté qu'une élongation

du squelette de seconde phase s'est produite durant l'extrusion. Cette élongation a mené à une réduction de l'espace inter-dendritique. La mobilité des dislocations peut ainsi être aussi restreint par la proximité des zone riche en seconde phase.

L'échantillon extrudé à 400 °C présente une faible augmentation de la dureté comparé à l'échantillon brut de coulée. La caractérisation microstructurale suggère qu'une recristallisation du matériau a mené à une taille de grain assez petite. L'augmentation de la dureté peut ainsi être expliquée par un effet Hall-Petch.

En utilisant l'ECAE, une taille de grain encore plus petite, que par l'extrusion à 400 °C, a été obtenue. Ainsi, la plus forte dureté de l'échantillon ayant subi l'ECAE est en accordance avec la loi de Hall-Petch. Cependant, dans le cas de l'échantillon ayant subi l'ECAE, la seconde phase est dispersée en petites particules d'une taille inférieure au micron. Dans le cas présent, les particules d'intermétallique, Mg_2Ca, peuvent être assimilées à des particules de renforcements.

La plus grande déformabilité de l'échantillon ayant subi de l'ECAE peut aussi être relié à une combinaison entre un effet de la taille de grain et un effet de la texture. Dans le magnésium, il y a peu de plans où la mobilité des dislocations est possible lors de la déformation à température ambiante (basal et prismatique). À cause de la faible taille de grain de l'échantillon ayant subi de l'ECAE, les mécanismes de déformation sont rapidement bloqués. Un autre mécanisme de déformation doit alors être activé sous une contrainte suffisante. Le maclage durant un test de compression sur des alliages de magnésium est bien connu et se produit tout d'abord selon le plan $\{10\bar{1}2\}$ [27]. Ainsi, le maclage peut se produire tout d'abord dans les grains favorablement orientés. Ce maclage est responsable de l'inflexion observé aux alentours de 125 MPa sur la courbe de compression de l'échantillon ayant subi de l'ECAE. Une fois que le maclage se produit, il y a une réorientation des cristallites (une rotation de 86 °) avec une orientation des plans moins favorable au glissement [28]. Afin de permettre à de nouveaux mécanismes de déformation de se produire, un niveau de contrainte plus élevé doit être obtenu. Koike et al. [29] ont rapporté un glissement aux joints de grains durant de la déformation à température ambiante sur un alliage AZ31 avec une taille de grain moyenne de 8 µm. Ainsi, grâce à la faible taille de grain de l'échantillon ayant subi l'ECAE, en plus du mouvement des

dislocations et du maclage, du glissement aux joints de grains peut se produire. Cette combinaison de différents mécanismes de déformations peut prendre part à l'augmentation de la résistance et de la déformabilité de cet échantillon.

Pour résumer, les investigations microstructurales ont permis d'identifier les éléments clefs qui interviennent dans l'amélioration des propriétés mécaniques. Ces éléments sont les suivant : la réduction de la taille de grain et la dispersion de la seconde phase en fines particules. Ces deux éléments peuvent être ajustés par les procédés thermomécaniques qui apparaissent comme un outil très efficace pour améliorer les propriétés mécaniques de l'alliage Mg-2wt.%Ca étudié. Il est intéressant de noter que le traitement par ECAE est particulièrement puissant car il permet de raffiner la taille de grain et en même temps la distribution de particules de seconde phase.

1.2.2 Microstructure et comportement en corrosion

Le Tableau 2 présente les mesures de corrosion de l'échantillon brut de coulée ainsi que des échantillons après traitement thermomécaniques ainsi que les observations microstructurales associés.

Tableau 2 : Caractéristiques microstructurales des échantillons après traitements thermomécaniques et leur comportement à la corrosion associé.

	Texture	Taille de grain	2^{de} phase	Taux de perte de masse ($mg.cm^{-2}.day^{-1}$)	R_{tot} à t = 1H ($\Omega.cm^2$)
Brut de coulée	-	Plusieurs mm	Squelette connecté	3.6	200
Laminé à 400 °C	Fibre	≈ 25 µm + macles	Squelette fragmenté	1.5	150
Extrudé à 200 °C	-	Plusieurs mm + macles	Squelette étiré et fragmenté	0.4	-
Extrudé à 400 °C	Faible	≈ 8 µm	Fragments + particules	0.6	2400
ECAE	Faible	≈ 2 µm	Particules [100–600 nm]	0.1	11500

Le comportement à la corrosion peut être impacté par différents paramètres microstructuraux listés dans le Tableau 2 : la taille de grain, la morphologie de la seconde phase et la texture. Cependant, les traitements thermomécaniques modifient plusieurs de ces paramètres en même temps. Il est alors difficile de les isoler afin de quantifier leurs répercussions. Néanmoins, dans le cas présent, il est possible de noter qu'un accroissement de la déformation équivalente du laminage à l'ECAE est associé à une diminution du taux de perte de masse.

Concernant l'évolution de la texture, seul le laminage produit une forte texture. Cependant, la taille de grain décroit pour les échantillons (sauf dans le cas de l'extrusion à 200 °C) et le squelette de seconde phase est quant à lui progressivement raffiné. En effet, l'échantillon brut de coulée montre un squelette de seconde phase connecté et une très faible résistance à la corrosion alors que, pour les échantillons après traitements thermomécaniques, le squelette est fragmenté et même dispersé en de fines particules.

Pour les alliages de magnésium-calcium, Harandi et al. [30] ont rapporté que, jusqu'à une certaine limite, l'ajout de calcium provoque une augmentation de la résistance à la corrosion du magnésium pur. Par contre, au-dessus de 1wt.% Harandi et al. [30] ont rapporté une augmentation du taux de dégradation dans un liquide physiologique. Cependant, Seong et al. [31] ont rapporté la possibilité de réduire le taux de corrosion de deux alliages de Mg-Ca (Mg-2wt.%Ca et Mg-3wt.%Ca) en réalisant du laminage à haut ratio de vitesses circonférentielles différentes. Ils expliquent cette amélioration de la tenue en corrosion au significatif raffinement de la seconde phase Mg_2Ca [31]. Comme rapporté par Kim et al. [32], la seconde phase, Mg_2Ca, est plus anodique que le magnésium et un effet micro-galvanique peut alors apparaître. Jeong et al. [33] ont proposé l'illustration suivante de cet effet micro-galvanique pour montrer l'impact d'une distribution continue ou discontinue de Mg_2Ca dans la matrice de magnésium, Figure 2. Il est suggéré que le même type d'impact s'applique à l'alliage présent.

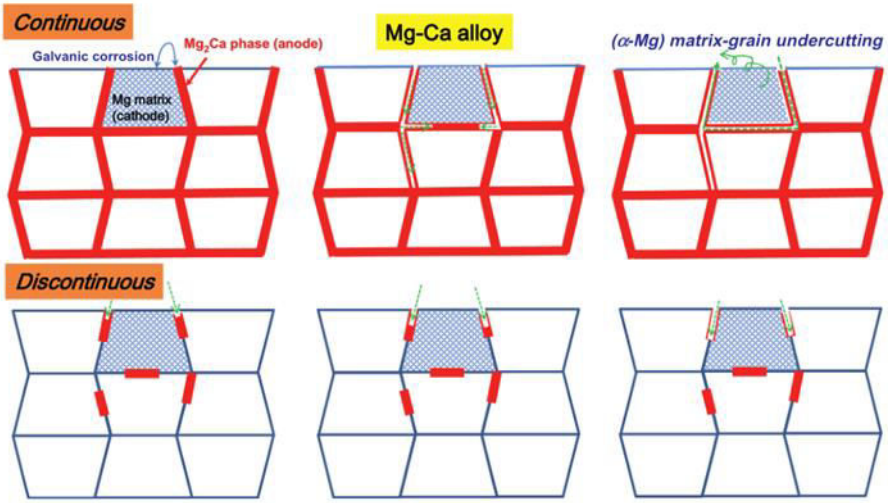

Figure 2 : Illustration de l'impact de la morphologie des phases Mg_2Ca dans les alliages de Mg-Ca [33].

Dans le cas présent, afin d'étudier plus en détail l'impact de la continuité/discontinuité du squelette de seconde phase, deux états différents (brut de coulée et extrudé à 400 °C) ont été caractérisé après immersion dans de la solution de Hanks. La Figure 3 montre des observations optiques de deux échantillons après 7 jours d'immersion (pour réaliser ces observations, les produits de corrosion ont été enlevés).

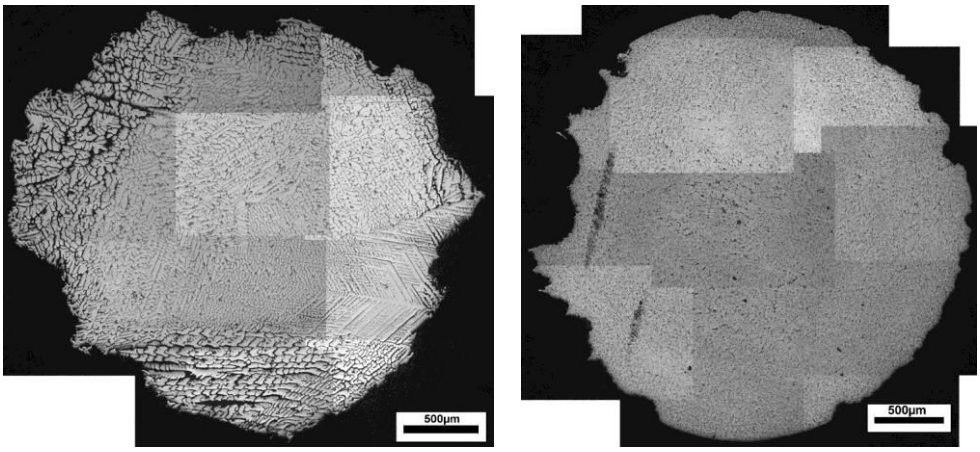

(a) (b)

Figure 3 : Observations microscopique d'une coupe transverse d'échantillons corrodés après immersion durant 7 jours dans de la solution de Hanks : (a) échantillon brut de coulée et (b) échantillon extrudé à 400 °C. Note : les zones inter-dendritiques apparaissant en noir sont vides.

La Figure 3 (a) montre qu'après corrosion, pour l'échantillon brut de coulée, le squelette de seconde phase est partiellement dégradé à cause de la corrosion. Au contraire, cela n'est pas observé pour l'échantillon extrudé à 400 °C (Figure 3 (b)).

L'échantillon brut de coulée (Figure 3 (a)) présente une corrosion massive commençant à la surface et se propageant le long des zones inter-dendritiques. Cela a pour conséquence une pénétration en profondeur de la corrosion dans l'échantillon. L'échantillon extrudé à 400 °C (Figure 3 (b)) quant à lui présente une plus faible corrosion et limitée à la surface du matériau. La Figure 4 montre une zone interne d'un échantillon brut de coulé corrodé à un plus fort grossissement.

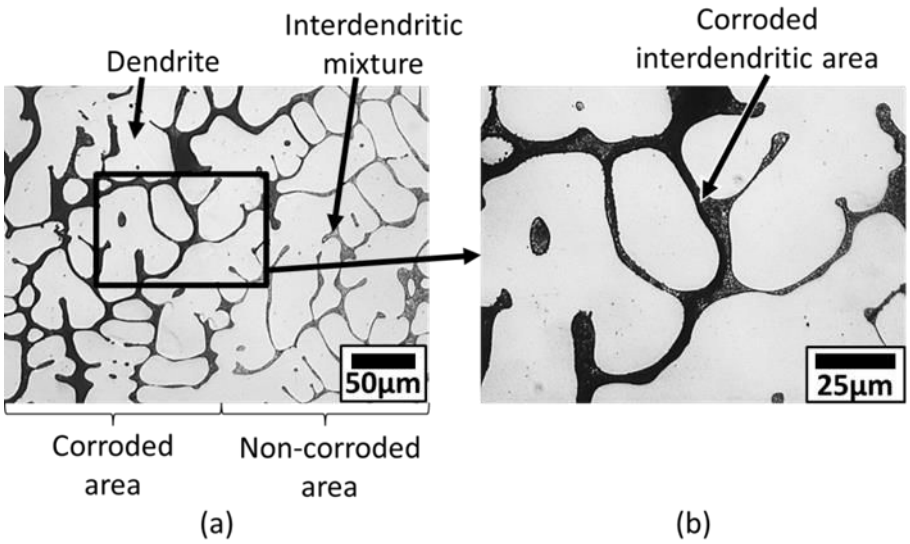

Figure 4 : Observations microscopiques : zone interne d'un échantillon brut de coulée après immersion durant 7 jours dans de la solution de Hanks et (b) un zoom sur une zone corrodée.

La Figure 4 (a) montre une zone corrodée avec des espaces inter-dendritiques vides (zones en noir) et une zone non corrodée où les espaces inter-dendritiques sont toujours remplis de la mixture eutectique. Comme on peut le voir sur le grossissement sur la Figure 4 (b), le phénomène de corrosion apparaît en premier lieu sur la mixture eutectique. La mixture eutectique est alors corrodée en premier la place de la matrice de magnésium et se désagrège. Lorsqu'un tel effet micro-galvanique prend place sur la mixture eutectique contenu dans les espaces inter-dendritiques, alors la corrosion peut pénétrer en profondeur du matériau. En raffinant ce squelette riche en seconde phase, il est alors possible de réduire la corrosion micro-galvanique.

Ce type de mécanisme est corroboré par l'évolution de la résistance des différents échantillons en fonction du temps d'immersion. La réduction de la résistance dans les premières heures d'immersion des échantillons bruts de coulée et laminé peut être due

à la dégradation continue de la mixture eutectique. Cet effet galvanique permet alors à la corrosion de progresser à l'intérieur du matériau. Dans le cas de l'échantillon laminé la résistance à la corrosion diminue fortement dès le début contrairement à l'échantillon extrudé à 400 °C qui a sa résistance à la corrosion qui décroit plus lentement. Cela peut alors être dû à la différence de morphologie de la seconde phase dans ces deux échantillons : dans l'échantillon extrudé à 400 °C, le squelette de seconde phase est beaucoup plus fragmenté que dans le cas de l'échantillon laminé.

L'échantillon ayant subi l'ECAE présente la plus grande résistance à la corrosion. De plus, cette forte résistance à la corrosion semble plutôt stable au cours du temps d'immersion. Ainsi, en plus d'une réduction drastique de l'effet galvanique dû au raffinement de la seconde phase, la grande résistance de la microstructure obtenue par ECAE suggère qu'un ou des autres paramètres peuvent améliorer la tenue à la corrosion.

Un autre paramètre microstructural important qui a été modifié durant l'ECAE est la taille de grain. Différentes études sur différents alliages de magnésium ont rapporté que la résistance à la corrosion augmentait avec la réduction de la taille de grain [16] [34] [35] [36]. Selon Kainer et al. [37], les contraintes de compression élevées entre le réseau cristallin du magnésium et la couche d'oxydes peuvent mener à des craquelures dans la couche d'oxydes. Birbilis et al. [34] ont rapporté qu'une plus forte densité de joints de grains en association avec une forte désorientation angulaire peut aider à la stabilité de la couche d'oxydes. Ce phénomène pourrait prendre part à l'amélioration de la tenue à la corrosion de l'échantillon ayant subi l'ECAE.

Jusqu'alors, l'interprétation a été focalisée sur les caractéristiques microstructurales majeures, soit la taille de grains et la morphologie de la seconde phase. Cependant, la texture est aussi connue pour modifier la résistance à la corrosion des alliages de magnésium. Par exemple, il est suggéré qu'une orientation basale des grains procure une plus grande résistance à la corrosion [38] [39]. Dans le cas présent, la forte texture basale de l'échantillon laminé peut jouer un rôle dans la forte augmentation de la résistance à la corrosion malgré une faible dispersion de la seconde phase dans le matériau. Cependant, pour les autres échantillons, il n'a pas été mesuré de texture

préférentielle et il n'est donc pas possible de conclure sur ce possible effet de la texture pour le cas présent.

La présence de dislocations et de macles dans la microstructure peut aussi modifier la tenue à la corrosion [36] [40]. Les traitements thermomécaniques employés dans la présente étude ont probablement modifié la densité de dislocations en plus des autres paramètres microstructuraux. Cependant, il n'a pas été décelé d'un évident impact de la densité de dislocations sur la tenue à la corrosion. L'investigation menée dans la présente étude montre que l'évolution de la taille de grain et la morphologie de la seconde phase possède une bonne corrélation avec l'évolution de la tenue à la corrosion.

1.3 Traitement de la surface par micro-déposition

1.3.1 Réalisation des dépôts

Tout d'abord, une étape d'optimisation des paramètres de déposition a été réalisée. Le fichier de travail qui a été utilisé pour contrôler la géométrie de la déposition dérivait un pattern de lignes croises (Figure 5).

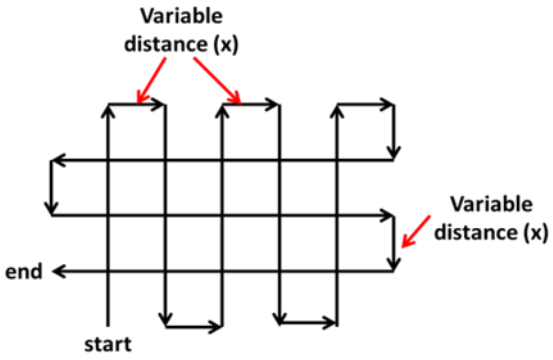

Figure 5 : Fichier de travail utilisé pour contrôler la géométrie du pattern lors de la déposition.

Après une série d'essais, des paramètres optimaux pour la déposition ont été déterminés. Ces paramètres ont permis d'obtenir des patterns reproductibles formés d'une ligne continue en une seule déposition comparé aux 10 à 20 couches nécessaires dans de précédentes études [41]. La Figure 6 montre une image MEB d'une déposition obtenue à l'aide de ces paramètres optimisés ainsi qu'un fort grossissement

sur une des lignes avant traitement thermique. On peut observer les nanoparticules d'argent sur cette image, Figure 6 (b).

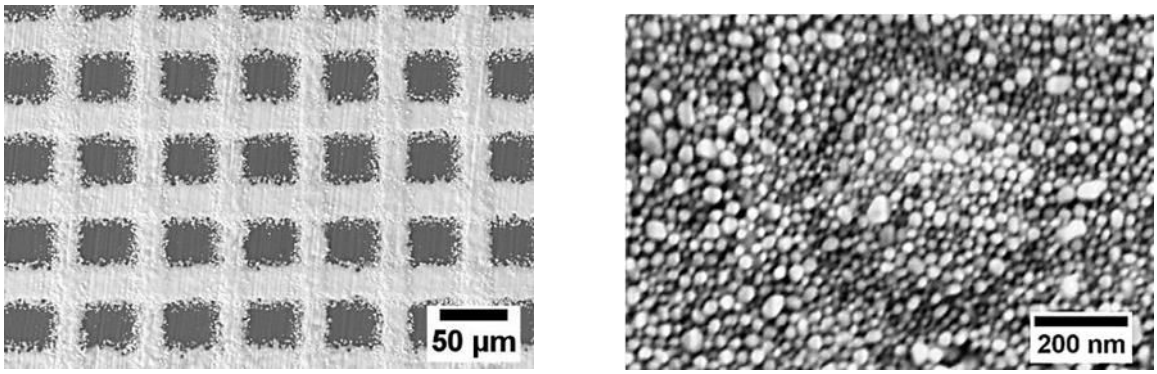

(a) (b)

Figure 6 : Images MEB de : (a) une déposition avec les paramètres optimisés et (b) un fort grossissement sur une des lignes déposées (composé de nanoparticules d'argent) avant traitement thermique.

En second lieu, ce sont les paramètres du traitement thermique qui ont été optimisé. Le traitement thermique était effectué à l'aide d'un laser continu à fibre dopé à l'erbium. Il a été déterminé qu'une puissance 8 W avec une vitesse d'environ 0.3 $mm.s^{-1}$ était nécessaire pour observer une agglomération des nanoparticules en surface du dépôt par MEB, Figure 7.

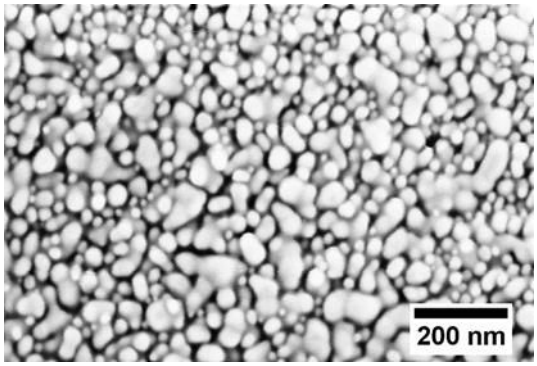

Figure 7 : Image MEB d'une déposition de nano-particules après traitement laser avec une puissance de 8 W, une vitesse de 0.3 $m.s^{-1}$ et une taille du spot du laser de 85 µm.

A la suite de l'optimisation des paramètres de déposition, une caractérisation du dépôt a été réalisée. Tout d'abord, la régularité de la déposition sur une grande échelle (plusieurs mm) a été contrôlée par profilométrie. Le résultat de la mesure de profilométrie réalisé sur un pattern de lignes croisées peut être observé en Figure 8. D'après l'échelle de couleur utilisée en z, l'épaisseur de la déposition est d'environ

1 µm pour une ligne simple et d'environ 2 µm aux croisements. La largeur d'une ligne est d'environ 20 µm.

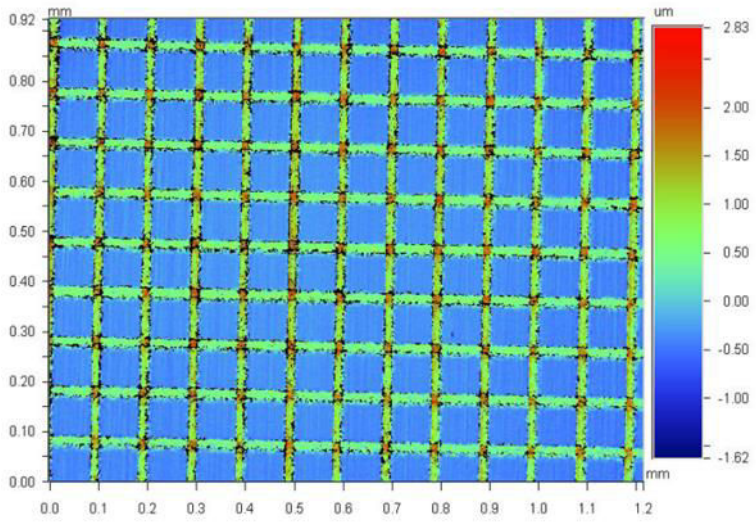

Figure 8 : Observation profilométrique d'un échantillon après déposition d'un pattern de nanoparticules d'argent.

Afin de compléter la caractérisation de la déposition, une section transverse, effectuée par coupe FIB, a été réalisée sur un échantillon après déposition et examinée par MEB. La Figure 9 (a) montre la localisation de la coupe FIB et la Figure 9 (b) montre une image MEB au fort grossissement de la coupe FIB en vue transverse. Il est possible de remarquer des défauts à l'interface avec une déposition qui n'est pas en cohésion avec le substrat.

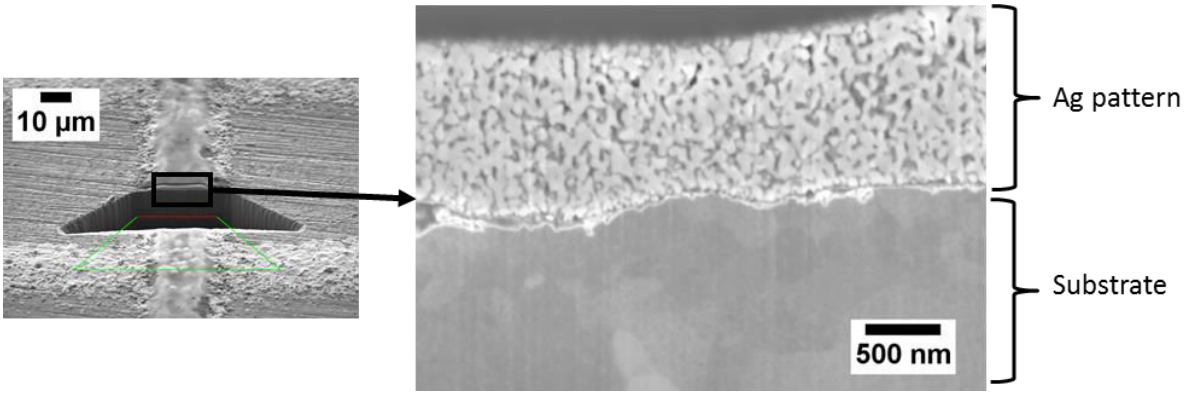

(a) (b)

Figure 9 : (a) Zone de la coupe FIB et (b) une image MEB de la section transverse d'une déposition de nano-particules d'argent après traitement thermique par laser (puissance = 8 W, vitesse = 0.1 $m.s^{-1}$, taille du spot = 85 µm).

Il a été réalisé une comparaison de la qualité du dépôt par observation de sections transverses après des traitements laser à différentes vitesses (0.1 $mm.s^{-1}$ et 0.7 $mm.s^{-1}$), Figure 10. Dans les deux conditions, la couche déposée présente une évolution homogène de sa morphologie sur toute son épaisseur. Les nano-particules d'argent ont formé une structure poreuse interconnectée après le traitement thermique par laser.

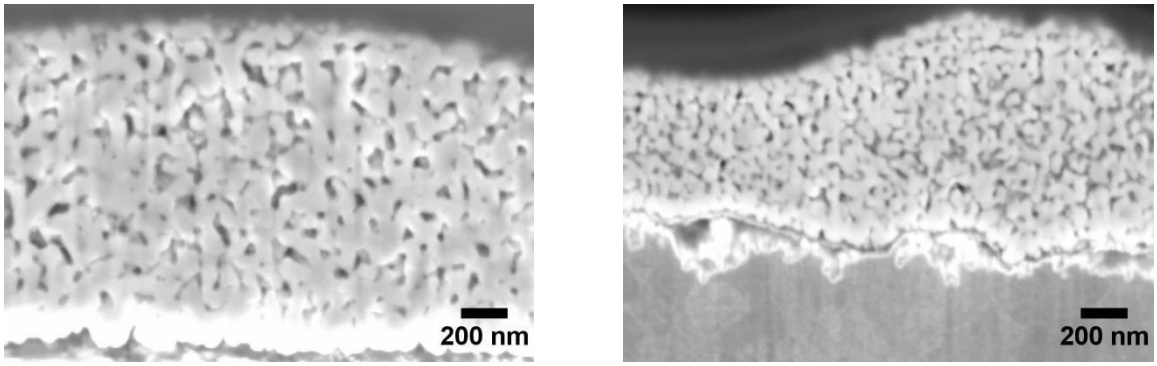

(a) (b)

Figure 10 : Images MEB d'une section transverse d'une déposition de nano-particules d'argent après traitement thermique au laser avec une puissance de 8 W, une taille du spot de 85 µm et une vitesse de (a) 0.1 $mm.s^{-1}$ et (b) 0.7 $mm.s^{-1}$.

Différentes mesures ont été réalisées sur les images MEB à l'aide du logiciel ImageJ, Table 3. Le taux moyen de porosités dans une déposition après traitement thermique est d'environ 31 % et 34 % pour une déposition avec une vitesse du laser de 0.1 $mm.s^{-1}$ et 0.7 $mm.^{-1}$ respectivement. Pour un entassement aléatoire de sphères, la porosité théorique est d'environ 38 % [42], ainsi, la densification obtenu durant le traitement thermique est très faible. Une telle structure micro-poreuse, après frittage de nano-particules d'argent, a déjà été rapportée dans la littérature [43] [44]. Il a aussi été rapporté la possibilité de décroître le taux de porosité d'une déposition de nano-particules d'argent par un traitement thermique en augmentant la durée de ce traitement thermique [45].

La taille moyenne des porosités a été déterminée par analyse image en utilisant ImageJ pour les deux conditions de traitement laser (différentes vitesses), Table 3. Le processus de densification se produisant durant le traitement thermique peut être

impacté par différents paramètres. La taille des particules et leur morphologie ainsi que le taux de porosité initial font partis de ces paramètres [46]. Durant les premières étapes de coalescence des particules, les particules les plus grosses vont grossir au dépend des plus petites particules à leur contact, [46]. Ces agglomérations de nano-particules participent à la formation de larges porosités. Il a été rapporté qu'une telle agglomération peut sévèrement ralentir le processus de densification [46].

Préalablement au traitement thermique, la déposition est composée de particules ayant une taille comprise entre 30 nm et 60 nm. Par analyse d'image, il a été déterminé que la taille moyenne des bras d'argent après traitement thermique est d'environ 81 nm et 48 nm pour un traitement laser à une vitesse de 0.1 $mm.s^{-1}$ et 0.7 $mm.^{-1}$ respectivement. Des agglomérations de particules ont ainsi pu être crée. Avec un temps d'interaction plus long, i.e. une vitesse plus lente, l'agglomération des particules est plus avancé et il en résulte une taille moyenne des bras d'argent plus grande. Cela est corroboré par la taille moyenne des porosités mesurée. L'agglomération des particules provoque un accroissement de la distance entre les bras d'argent, ce qui implique un accroissement de la taille des porosités. Ainsi, seul un début de frittage a pu être réalisé en utilisant les vitesses de laser de la présente étude, une complète densification de la déposition nécessitant une vitesse encore pls lente.

Table 3: Résultats des analyses d'images sur les images MEB des dépositions après traitement laser.

Analyse d'image	Vitesse du laser 0.1 $mm.s^{-1}$	Vitesse du laser 0.7 $mm.s^{-1}$
Porosité moyenne	31 %	34 %
Taille moyenne des porosités	46 nm	28 nm
Taille moyenne des bras d'argent	81 nm	48 nm

Sur l'image MEB de la section transverse, Figure 11, trois différentes zones peuvent être distinguées. Tout au-dessus, il y a la déposition poreuse d'argent qui a été précédemment décrite et qui ne présente pas de cohésion avec le substrat. Sous la déposition, juste sous la surface, il y a une fine couche dans le substrat ayant une

taille de grain très fine. Cette sous-couche est aussi présente à la surface de l'échantillon dans des zones sans déposition, Figure 12. Cette sous-couche possède une épaisseur d'environ 1 µm et est formée de grains de magnésium d'une taille allant de 100 nm à 1 µm. En-dessous de cette sous-couche on peut voir le substrat, un échantillon extrudé à 400 °C, qui possède de larges grains et des fragments de second phase.

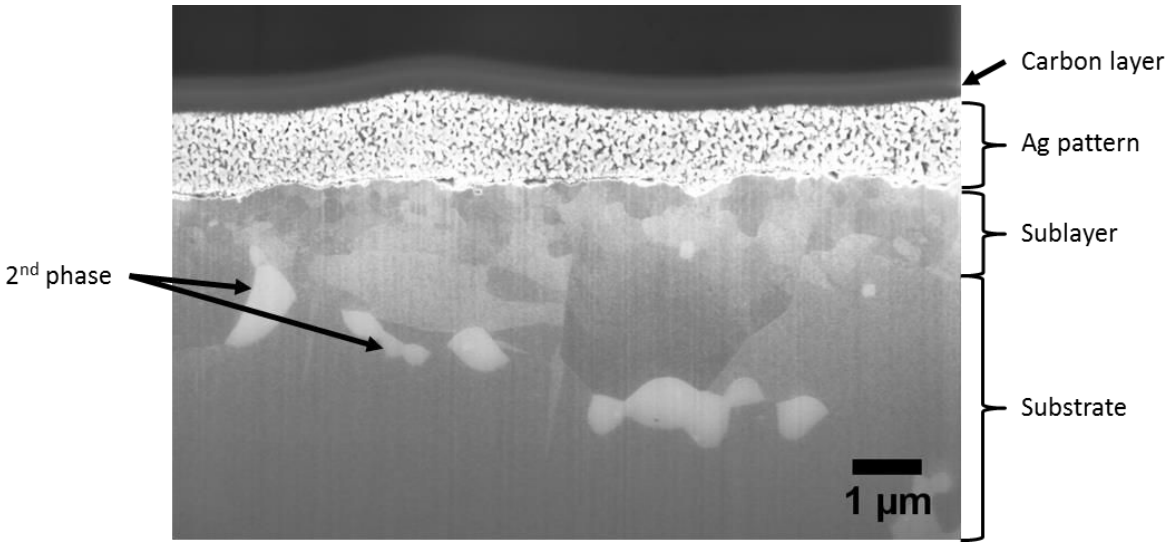

Figure 11 : Image MEB d'un section transverse d'un échantillon avec déposition après traitement laser.

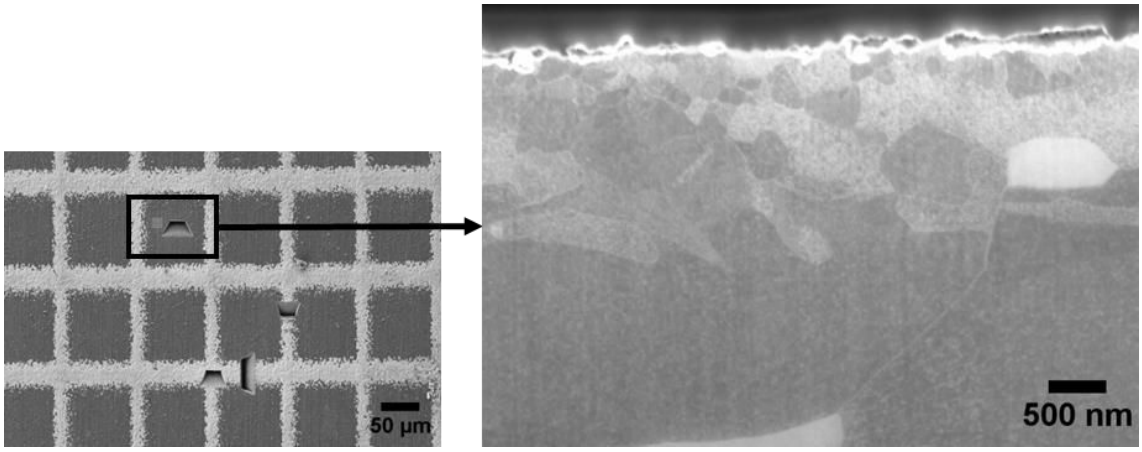

(a) (b)

Figure 12 : (a) Localisation de la découpe FIB et (b) image MEB d'une section transverse de la surface d'un échantillon après traitement laser.

Cette sous-couche révèle l'existence d'une zone thermiquement affectée par le traitement laser. La préparation des échantillons en vue de la déposition nécessite une étape de polissage mécanique sur un papier 4000 grit. La taille équivalente des grains

de ce papier est d'environ 4 µm. Une rugosité d'environ 2 µm peut alors être attendu en surface du matériau. Mais, les précédentes observations réalisé par profilométrie ou par MEB ont montré que la rugosité de surface du substrat était très faible : environ 0.2 µm. Ainsi, durant le polissage, de la déformation plastique a pu se produire à la surface du matériau. De plus, au cours des caractérisations par MET, il a été noté une importante densité de dislocations dû aux étapes préalable de polissage. En effet, le matériau étudié est très mou car le calcium ne possède qu'une très faible solubilité dans le magnésium, la matrice n'étant donc formé principalement que de magnésium pur. Cet écrouissage de surface lors des étapes de préparation a donc pu créer cette sous-couche par recristallisation lors du traitement thermique.

1.3.2 Simulation numérique de l'impact thermique du traitement laser

Dans la partie précédente, il a été décrit le procédé de fonctionnalisation de surface : il y a tout d'abord la déposition d'une couche de nano-particules d'argent à la surface de l'échantillon puis un traitement laser est utilisé pour fritter cette déposition. Les observations en coupe transverse ont permis de mettre en évidence la qualité du frittage. La déposition présente une microstructure poreuse et n'est pas cohésive avec le substrat. Ces observations ont été réalisé pour deux conditions de traitement laser avec pour seul changement la vitesse du laser : 0.1 $mm.s^{-1}$ et 0.7 $mm.s^{-1}$. D'autres paramètres du traitement laser pourraient aider à améliorer le frittage de la déposition : la puissance du laser et la taille du spot.

Un autre point à prendre en compte est la spécificité du procédé de fonctionnalisation dans le cas présent : substrat défini et déposition contrôlée (topographie et géométrie). Cependant, selon les exigences de l'application finale, ces paramètres peuvent être amenés à être modifié. En utilisant un modèle par éléments finis, il peut être possible de simuler l'évolution thermique dans le substrat et dans la déposition au cours du traitement laser. Un tel modèle pourrait servir de base pour étudier l'impact de la modification des paramètres du laser. Cela pourrait alors être utilisé afin d'amélioré le procédé de fonctionnalisation de surface.

À l'aide du module « transfert thermique en milieu solide » du logiciel COMSOL Multiphysics, il est possible de simuler les effets thermiques pour le système « porte

échantillon / échantillon / déposition d'Ag ». Les propriétés thermo-physiques des différents matériaux mis en jeu doivent tenir compte de la composition de l'alliage et de la microstructure poreuse de la déposition. La littérature existante sur le sujet des interactions avec un faisceau laser, [47], et aussi plus spécifiquement sur le frittage de nano-particules d'argent, [48] [49], procure les bases pour modéliser les différentes interactions thermique.

La Figure 13 montre le système modélisé avec le trajet du laser lors de la simulation : une ligne droite entre les points « a » et « c ». Entre les points « a » et « b » le laser sera sur une zone de substrat sans déposition. Ce domaine permet d'arriver d'atteindre un état de stabilité thermique. Entre les points « a » et « c », le début du parcours est une zone sans déposition et sur la fin du parcours le laser passe sur une déposition d'argent modélisée. Ce domaine permet d'obtenir des informations sur l'évolution thermique du substrat et de la déposition lors du passage du laser. La déposition est modélisée par un domaine de 200 µm de long et 20 µm de large. La longueur de ce domaine a volontairement été réduite au maximum afin de diminuer le nombre d'éléments de maillage et par conséquent le temps de calcul.

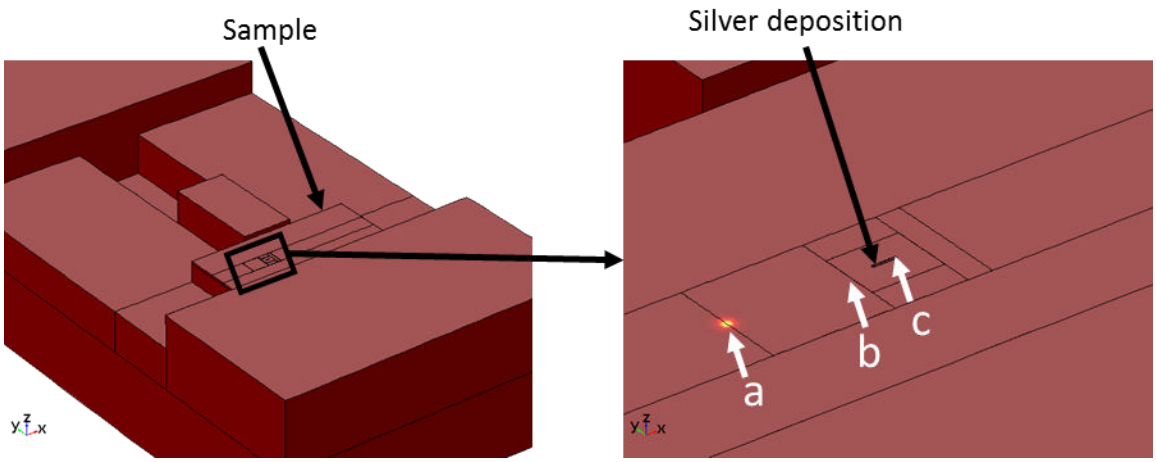

Figure 13 : (a) Représentation 3-D du système « porte échantillon / échantillon / déposition d'Ag » et (b) un grossissement sur le trajet du laser : une ligne droite entre les points « a » et « c ».

Il est important de bien définir le maillage de ces différents domaines afin de modéliser correctement la distribution d'énergie. En effet, une fluctuation de l'impact thermique peut survenir dans le cas d'un maillage trop gros. Le maillage doit donc être suffisamment fin pour permettre une simulation correcte du flux thermique selon la précision de l'étude Concernant la déposition, la taille maximum d'un élément du

maillage est limitée par l'épaisseur de la déposition : 1 µm. Il s'est avéré après essai, que cette taille permettait de visualiser correctement les échanges thermiques dans le cas présent.

Concernant la surface de l'échantillon, il a été choisi d'emboîter des domaines avec un maillage de plus en plus petit vers la déposition. Cela afin de diminuer le nombre total d'éléments et d'assurer une bonne continuité des domaines en terme de taille des maillages. Le modèle a ainsi été utilisé pour prédire les évolutions thermiques du système avec différentes associations de maillage pour ce domaine. En diminuant la taille du maillage il y a une augmentation de la température maximale prédite dans le substrat du par le raffinement de l'apport local d'énergie par le laser, i.e. le spot du laser était en contact avec une surface de maillage plus faible. Cette augmentation arrivant à son maximum lorsque l'effet du maillage devient négligeable.

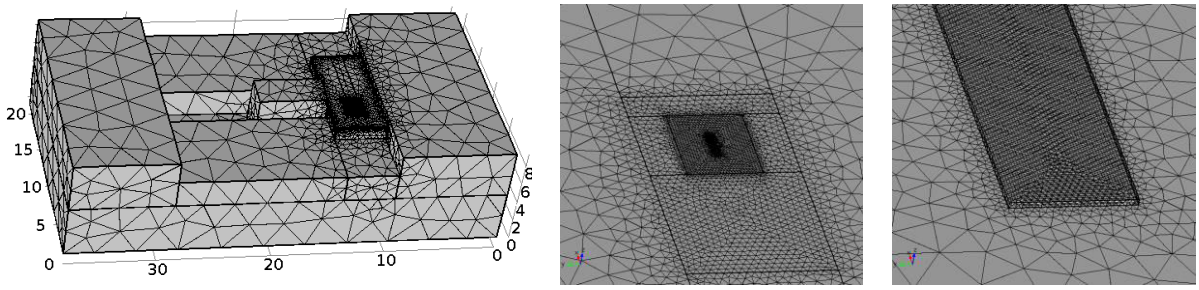

(a) (b) (c)

Figure 14 : Visualisation du maillage du modèle : (a) vue globale, (b) un zoom autour de la zone de stabilité thermique et (c) un zoom sur la déposition.

Le modèle a ainsi été utilisé pour prédire l'évolution thermique du système lors du traitement laser. Les paramètres d'entrée ont été modulés selon la littérature existante et plus particulièrement l'absorbance du matériau. De ces modélisations il a été extrait l'évolution thermique au sein du matériau et de la déposition. En utilisant les précédentes caractérisations microstructurales des échantillons il a été possible de borner les paramètres d'entrée des matériaux.

En utilisant ce modèle il est donc maintenant possible de prédire les évolutions thermiques au sein du matériau et de la déposition pour différentes valeurs de traitement laser (vitesse, puissance, taille du spot). Ce modèle peut alors être utilisé afin d'améliorer la qualité de la déposition et plus spécifiquement l'interaction entre la déposition et le substrat.

Sur l'intervalle étudié, le modèle a montré que la vitesse du laser affecté grandement le profil de température durant le traitement laser. Modifier la vitesse du laser pourrait ainsi permettre d'obtenir différent taux de porosité à l'intérieur de la déposition. Le modèle a aussi permis de montrer que le substrat est sujet à un fort effet thermique. La fine sous-couche de petits grains à la surface du substrat ne donnant qu'une limite basse de cet effet thermique. Il est ainsi important de pouvoir prédire l'impact thermique sur le substrat afin d'éviter une modification importante de sa microstructure. Cette microstructure ayant été préalablement architecturée grâce à un procédé thermomécanique.

1.4 Conclusion

La présente étude a été réalisée pour démontrer la capacité des traitements thermomécaniques combinés à un traitement de la surface à s'adapter à une application médicale d'implants dégradables. Cette application finale implique différents axes d'étude : les propriétés mécaniques, le comportement à la corrosion, la fonctionnalisation de surface et l'interaction *in vivo*. Ainsi, selon le point de vue, il est possible de suivre différentes routes pour modifier les propriétés d'un matériau. Dans la présente étude, il a été choisi de travailler d'un point de vue métallurgiste. La composition de l'alliage a été sélectionnée afin de répondre aux exigences *in vivo*. Puis, l'amélioration du matériau a été réalisée en suivant une stratégie en deux étapes : d'abord agir sur la microstructure du matériau pour changer ses propriétés mécanique et de corrosion, puis agir sur la surface pour la fonctionnaliser.

La première étape de ce travail était donc de modifier la microstructure interne du matériau sélectionné. Afin de réussir cet objectif, différents traitement thermomécaniques ont été mis en œuvre. La microstructure des échantillons ayant subis ces traitement thermomécaniques a aussi été caractérisée : taille de grains, morphologie de l'intermétallique et mesures de texture. Sur la base de la littérature existante, les principaux mécanismes responsables de l'amélioration des propriétés mécaniques et du comportement à la corrosion ont été identifiés. Concernant les propriétés mécaniques, différentes caractéristiques microstructurales peuvent être à l'origine de l'augmentation de la résistance du matériau : densité de dislocations,

macles, taille de grains et morphologie de l'intermétallique. Concernant le comportement en corrosion, la dispersion et la taille de l'intermétallique (Mg_2Ca) est apparu comme un paramètre clef pour réduire le taux de corrosion. La dispersion de l'intermétallique en de fines particules permet de réduire considérablement le processus de corrosion galvanique entre la matrice de magnésium et ces particules. En plus de cela, la réduction de la taille de grains peut aider à augmenter la résistance à la corrosion. Cela peut s'expliquer par l'accroissement de la densité des joints de grains qui permet de décroître les contraintes de compression qui existe entre la matrice de magnésium et la couche d'oxydes. À la suite de cette première étude, l'ECAE est apparu comme le procédé thermomécanique le plus efficace pour améliorer les propriétés mécaniques et le comportement à la corrosion de l'alliage Mg-2wt.%Ca.

La seconde partie de ce travail était centré sur la fonctionnalisation de surface. En utilisant une technique de fabrication additive il a été possible de déposer à la surface du matériau des couches de nano-particules avec différentes géométries. L'argent a été ici choisi pour ses propriétés antibactériennes. Après une première phase d'optimisation des paramètres de micro-déposition, il a été possible de réaliser un réseau de lignes continues de nano-particules d'argent selon une géométrie contrôlée. Un traitement laser a été réalisé à la suite de la déposition afin de rendre cette couche d'argent cohésive du substrat. Des observations en section transverse ont permis de caractériser la qualité de l'interface et de la déposition. La couche déposée présente une microstructure poreuse qui est caractéristique d'un frittage partiel des nano-particules d'argent. De plus, il a été noté que cette couche n'était pas entièrement cohésive avec le substrat. Une sous-couche de petits grains (moins de 1 µm) a été observée à la surface des échantillons. Ainsi, la caractérisation en section transverse a mis en évidence l'impact thermique du traitement laser sur le substrat. Afin d'améliorer la qualité du traitement thermique de la déposition, un modèle thermique a été réalisé en utilisant le logiciel COMSOL Multiphysics. En utilisant ce modèle il est ainsi possible de prédire les évolutions thermiques du substrat et de la déposition au cours du traitement laser. Ce modèle peut ainsi être utilisé pour améliorer la qualité de la déposition et de son interface avec le substrat en modifiant

les paramètres de frittage tels que la vitesse du laser, sa puissance ou encore la taille du spot.

2. Introduction

Each year, millions of people suffer from bone fracture. This number is expected to increase due to the longevity increase and popularity of extreme sports. Many bone injuries can be treated using implants. However, based on the location of the trauma, patients may need different types of implants. The implants can be categorized into different groups of applications: joint replacements (hip, knee, and shoulder), bone fixation plates and screws, spine disks, bone defect repair and dental implant-tooth fixation [1]. In these categories, it is possible to distinguish two main themes: implants that have to stay in the body to ensure the correct functionality of the treated bone (artificial replacement parts) and implants for bone fixation that will provide a temporary mechanical support for the treated bone.

Nowadays implants for bone fixation are usually made of stainless steels, cobalt-based alloys and titanium alloys [2]. These materials have been optimized for this application and can provide the mechanical support under loading during the whole healing time. However, they can lead to several complications like metal allergy, stress-shielding, infection or necrosis of soft-tissue around the implant [3]. In addition, after bone has healed, these implants often have to be removed especially for paediatric patients [4]. This operation involves more morbidity due to the surgery and leads to an extensive cost of medical care [5]. The use of biodegradable materials may then be an attractive solution for the development of new implants that would eliminate the need for removal surgery. Our interest will focus on these kinds of implants.

Various biodegradable materials have already been identified for such implant applications. These materials include polymers like polyglycolide, polylactide and polydioxanone [6]. However, usually, polymers have low mechanical properties which make them unsuitable for load bearing applications. For instance, their bulk moduli,

important for stiffness, are about ten times smaller than those of the bone structures [7]. From this point of view, due to their better mechanical properties, metallic systems are highly attractive. However degradable implant applications require metallic materials to be degradable and biocompatible. In addition, the degradation products have to be well tolerated by the body. Very few metallic systems fulfil these requirements. Indeed, magnesium due to its good tolerance by the body (a 400 mg daily intake is even recommended [8]) and its natural tendency for degradation (i.e. low corrosion resistance), stands as the most promising candidate. According to earlier reports, Edward C. Huse had used magnesium as degradable ligature wires on a patient in 1878 [9]. Since then, although the research progress in biodegradable Mg alloys was slow for many years; the last decade has seen major progress in this area.

In addition to good tolerance and natural degradation, magnesium alloys have an elastic modulus level (40 GPa) relatively close to those of the bone structures: about 20 GPa for cancellous bones [10]. Therefore, due to this similarity in elastic modulus to bones, a magnesium implant allows a better stress repartition during healing. As a consequence, the stress-shielding effect [11] that is a major problem for bone healing is reduced. No other metallic system has such advantage, since all other load bearing metals have higher elastic moduli. However, the yield stress of pure magnesium is low (20 MPa for pure magnesium [12]) compared to bones (120 MPa [13]). Therefore it may be preferable to use magnesium alloys which can provide higher yield strength values [14].

Mechanical properties of magnesium devices are usually improved by using magnesium alloys instead of pure magnesium. The addition of alloying elements to magnesium for implant applications has two drawbacks: first these elements can be toxic for the body, second the corrosion rate is generally higher than that for pure magnesium. The appropriate corrosion rate for a magnesium-based implant is dependent on the application itself: basically the degradation time of the implant has to be compatible with the healing process. Figure 15 illustrates the ideal condition for bone healing being concurrent with gradual implant degradation. The desired degradation time of the implant depends on many parameters (implant size, location and material characteristics) and is then very variable. Beside the needs for a good matching with the healing time, the corrosion process also has to avoid the formation

of too large bubbles due to the fast release of the hydrogen gas produced by the corrosion of magnesium. The control of corrosion rate is thus a major issue for a magnesium-based implant.

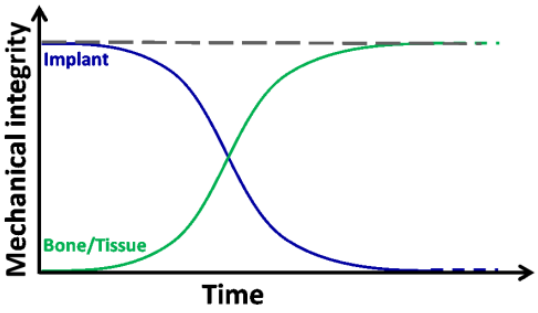

Figure 15: Desirable mechanical integrity of a degradable implant during healing process, adapted from [15].

Mechanical properties of magnesium alloys can also be improved by thermomechanical processing. For example, this may be achieved by hot rolling or extrusion processes that modify the microstructure (grain size, texture, second phase distribution). The impact of thermomechanical processes on corrosion properties has been considered in several studies [16] [17] [18] [19] [20]. Apparently, the presence of a second phase, grain size and texture influence the corrosion rate [16] [20]. But the possibility of controlling the corrosion rate by thermomechanical process is still open to extensive research. Although, magnesium appears as the most suitable metal for biodegradable bone implant applications, it still needs significant optimization of its mechanical properties and corrosion behavior before being approved and used.

This thesis focuses on studying the effect of thermomechanical processing and surface treatment on the degradation of an alloy of magnesium with calcium (i.e. Mg-2wt.%Ca). It is worth noting that surface treatment is of interest due to the fact that the implant surface is the first part to be in contact with the body environment and therefore is of importance for implant optimization. In addition, special surface treatments may provide additional benefits in biological reactions.

The general goal of the project is the development of bulk and surface processing approaches for developing optimized magnesium alloys for biomedical applications as degradable implants. In this context, a focus on the optimization of a Mg-Ca alloy

through thermomechanical treatments and a surface patterning technique by additive manufacturing will be done.

Selection of the Mg-Ca system is based on the biocompatibility and additional processing benefits of calcium [22] [23].

The objectives of the project are as follows:

- Optimization of the mechanical properties and corrosion behavior of the alloy by three different thermomechanical processing methods.
- Surface functionalization by silver deposition using a specific additive manufacturing technique. Silver is noted to provide the implant with an antibacterial effect [21]. Moreover, patterning of silver may allow better cell adhesion.

To achieve the first objective, conventional hot rolling and extrusion, as well as a non-conventional processing method, i.e. equal channel angular pressing (ECAP), have been chosen. The mechanical and corrosion behavior are evaluated by classical methods: micro-hardness tests, compression tests, immersion tests, electrochemical impedance spectroscopy (EIS). Multiscale characterization of the microstructure is carried out by optical microscopy, scanning electron microscopy (SEM) and transmission electron microscopy (TEM). These investigations aim at making the link between the microstructure tailoring produced by the various thermomechanical processing and the optimization of mechanical properties and corrosion behavior.

To achieve the second objective, an additive manufacturing method using a microdeposition machine (LAMM) [24] is adopted to deposit silver nanoparticles on the alloy surfaces. The deposition is followed by a laser sintering process. A series of deposition processes is performed in order to optimize the deposition conditions for silver nanoparticles and to obtain controlled patterning of the surface. The optimum conditions of patterning are identified using SEM and profilometry imaging. The microstructure of patterned samples and the quality of Ag deposit-substrate interface are evaluated by SEM and TEM characterizations of cross sections through the deposition and the substrate. The impact of laser treatment on the substrate will be modelled by a finite element simulation technique using COMSOL software. The aim

of this simulation is to model the thermal impact of the different conditions (laser power, laser speed) so that appropriate conditions to obtain different states of sintering of the silver nanoparticles within the deposition can be determined.

3. Background knowledge

As described in the introduction, the present work is focused on a particular biomedical application of magnesium, i.e., a degradable implants, which requires specific properties. However, magnesium and magnesium alloys are well known regarding other applications. In this chapter global considerations on magnesium will be given. The general applications of magnesium and magnesium alloys will be briefly described; then mechanical properties as well as the corrosion aspects will be reviewed. Also, an introduction to bone structure and implant will remind basic notions on the scope of the application. At the beginning of Chapters 3 and 4, the literature dedicated to the specific scope of the respective chapter will be more specifically reviewed.

3.1 Introduction to Mg and Mg alloys

3.1.1 Applications of Magnesium

Magnesium is one of the most abundant elements: the eighth in Earth's crust, the fifth in seawater. Magnesium can be found in different ores like dolomite, magnesite, brucite, olivine and also in water as an ion. Two main routes of production have been followed: the electrolytic process and the thermal process. Nowadays, the production of magnesium is estimated to 800 000 tons per year [50].

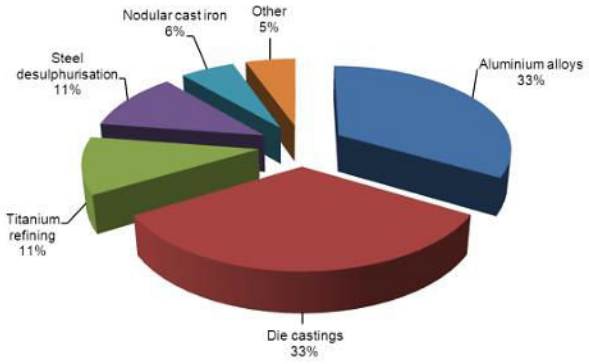

Figure 16: World consumption of magnesium by end-use, 2012 [51].

As illustrated in Figure 16, half of the magnesium production is used in alloying of other metals (aluminium, titanium, steels). The second important use of magnesium is for cast products. About 90 % of the magnesium alloys for structural applications are produced by casting [52]. A fast process is the high pressure die casting. However, the resulting products may contain porosity and are difficult to cast intricate shapes. To obtain complex shape with low porosity, low pressure mold castings or sand castings could be used.

Besides casting, thermomechanical processes can be employed to obtain magnesium products with desired shapes. The most common thermomechanical processing techniques that can be used for Mg fabrication are extrusion, rolling and press forging. Since at low temperature, magnesium shows low formability, these thermomechanical processing are usually carried out at high temperature (300 °C to 500 °C) [53].

Magnesium was employed for aircrafts during the 2nd World War and also later on vehicles for wheels, engine components, brackets and panels [53]. Using magnesium in vehicles decreases the weight, and consequently reduces gas consumption. However a major drawback of magnesium for structural applications (automotive, aeronautics) is its low corrosion resistance, and thus the requirements for surface protection. Recently, research on magnesium for structure lightweighting progressed significantly. Magnesium is also of importance for portable electronic devices such as laptops and cell phones.

Magnesium based alloys have been developed for applications as structural materials and therefore most of the works and knowledge are centered on this application. For

instance, alloying, mechanical properties, thermomechanical processes are well documented. Other properties like corrosion are currently studied but usually in particular media in connection with specific applications. Specifications for such industrial applications are not the same as for biomedical applications especially for a material to be degraded in the body. To use of magnesium alloys for biomedical applications, high purity materials are expected to be employed with possible additions of solute elements selected for their body tolerance along with other processing and property benefits. This should result in grades quite different from the ones employed for other applications. Therefore, Mg-based systems selected for biomedical applications need analyses dedicated to their characteristics and expected service.

3.1.2 Main characteristics and properties of Mg and Mg alloys

This section will be limited to the presentation of the main characteristics and properties relevant for the current subject. Therefore, only mechanical and corrosion properties of magnesium and its alloys will be introduced.

3.1.2.1 Mechanical behavior

Magnesium has a remarkably low density: only 1.74 g·cm^{-3}. Magnesium is the lightest engineering metal; by comparison, the density of iron and aluminium are respectively 7.87 g·cm^{-3} and 2.70 g·cm^{-3}. On the other hand, pure magnesium has low mechanical properties [12] [53]. However due to its low density, the specific strength (strength/density ratio) of magnesium is particularly high, which makes magnesium a highly attractive material for structural applications.

Contrary to the mostly used metals like iron and aluminium which have cubic crystallographic structures, magnesium has a hexagonal closed-packed structure (h.c.p.). This crystallographic feature has an impact on the formability or ductility of magnesium. Low ductility of magnesium at room temperature results from the low number of active slip systems of the hexagonal cell. Plastic deformation by slip mechanisms occurs primarily along the most dense direction and planes. In a h.c.p. structure, there is only one dense plane: the basal plane, (0001). Secondary slip can take place on the prismatic $\{10\bar{1}0\}$ planes along the $\langle 11\bar{2}0\rangle$ direction and activation of other glide mechanisms in pure magnesium is also possible at higher temperature.

For instance, above 250 °C glide on the $\{10\bar{1}1\}$ pyramidal plane in the $\langle 11\bar{2}0\rangle$ direction is activated [12]. Another important deformation mechanism in magnesium is twinning. At room temperature, twinning occurs primary across the $\{10\bar{1}2\}$ planes [12]. To improve ductility and other mechanical properties of magnesium, it is essential to modify the microstructure using thermomechanical processing and/or by alloying.

Thermomechanical processing

Thermomechanical processing methods basically consist of applying plastic deformation at low or high temperature. They can be classified based on the temperature of the operation. Typically hot working is done at temperature above 0.5 Tm where Tm is the melting temperature of the material, while cold working is done near room temperature (RT). "Warm working" is a term used for thermomechanical processing at temperatures between RT and 0.5 Tm. The most common thermomechanical processing methods are rolling and extrusion which are used at the industrial scale. At the laboratory scale, non-conventional processes are being developed allowing for extreme conditions of deformation. The following three processing are examples of such methods: equal channel angular extrusion, high pressure torsion and accumulative roll-bonding [54].

The change in mechanical properties after thermomechanical processing is related to a strong modification of the coarse cast microstructure of the starting material. Indeed, the main effects of thermomechanical processing may include the modification of the grain size, the dispersion of the phases present in the material, the dissolution of certain phases and the formation of new phases. Generally speaking, deformations are associated with the production of lattice defects in the microstructure. In general, the higher is the density of defects, the higher is the internal energy of the material. The deformed system then has a natural tendency to decrease this excess energy by microstructural evolution. Reorganization of these defects usually occurs during or after a thermomechanical treatment. Depending on the temperature and the total internal stress, this reorganization can lead to local or more global microstructural changes.

For instance, entangled dislocations may annihilate or form a substructure, named low-energy dislocation structure. This substructure is formed within the existing grains and has low angle boundaries [55]. This stage corresponding to the decrease of the dislocation density without grain size change is called recovery; it is usually the first step to occur in the microstructural evolution after deformation. When temperature is high enough and with sufficient driving force due to the deformation, recrystallization of the material can occur. The misorientation between the cells of the substructure may increase creating new grains [55]. Nucleation and then growth of new grains free of dislocations can also occur at high dislocations density zones or in the vicinity of second phase particles [56]. This process is named static or dynamic recrystallization, depending on whether it occurs during deformation or during a heat treatment after the deformation. In magnesium alloys, the typical size range obtained by static recrystallization is 8 µm to 25 µm [57]. Dynamic recrystallization usually attains better grain refinement. For instance, using severe plastic deformation techniques, ultrafine grain size around 1 µm can be achieved [58].

The grain size has an impact on the strength of the material. When a finer grain size is obtained the material has usually a higher strength. This behavior known as the Hall-Petch effect is described by an empirical law which link the average diameter of grain, d, to the yield strength of the material, σ_y [59]:

$$\sigma_y = \sigma_0 + k_y \times d^{-1/2} \qquad (1)$$

where σ_0 is a material constant and k_y a strengthening coefficient specific for each material. This increase of the strength can be accounted to the difference of dislocation mobility between the interior of a grain and across grain boundaries. Due to the crystallographic disorientation between two grains, a higher energy level is required for a dislocation to cross a grain boundary than to propagate inside a grain. As a consequence at a grain boundary, dislocation propagation is slow and they tend to pile-up. This pile-up of dislocations creates a stress concentration. Under deformation, it can reach a critical stress value matching the one required to propagate through grain boundaries. When this critical stress is reached, further deformation can occur. Since with smaller grains more dislocations will pile-up due to

the increase of grain boundaries area, and thus the applied force required for plastic deformation has to be higher.

In the case of an alloy, the presence of particles may impact the microstructure evolution (recovery, recrystallization and grain growth). Indeed, the motion of grain boundaries can be impacted by pinning force coming from these particles [60]. This effect, also called Zener pinning, depend on the particle volume fraction and size [61]. The Zener force writes as follow:

$$F_z = \frac{3}{2} \times \frac{f_v \times \gamma_s}{r} \qquad (2)$$

where f_v is the volume fraction, r the size and γ_s the interfacial energy of the particles. Thus the finer and the denser is the dispersion of particles, the higher is its impact on the microstructure evolution and mechanical properties.

For instance, an increase of the density of the particles associated with a refinement of the average size of these particles may happen [62]. On a Mg−6Zn−0.5Zr(wt.%) alloy, a specific ECAP process involving an equivalent strain of 5.4 have been reported to break and redistribute the Mg-Zn and Zn-Zr inter-metallic phases, along with a refinement of the grain size. This process has reported to increase the ultimate tensile strength from 264 MPa to 351 MPa [63].

Alloying

Alloying is another possibility to improve mechanical behavior of magnesium. This hardening comes from the modification of dislocation motion due to matrix deformation, solute drag or formation of solute clusters. It is also important to note that the morphology of the precipitate play an important role on the interaction with dislocations. Indeed, it will be easier to bypass a precipitate which is oriented parallel to the slip plane. In magnesium, the most active slip system is in the basal plane. Thus it has been suggested that precipitates elongated along the c-axis direction will have a higher hardening effect [64].

Alloying consists of forming a supersaturated solid solution by high temperature treatment. At lower temperatures, if the element solubility in magnesium is high, the alloying element will remain as dispersed solutes which can be responsible for the so

called solution hardening. If the solubility is low, the metastable supersaturated solution decomposes by natural or artificial aging, forming a fine scale precipitation within the magnesium grains. This precipitation may have a hardening effect due to the pinning of dislocations during deformation on the precipitates.

Magnesium structure could accept a large number of alloying elements [65]. Aluminium is the most frequent alloying element because it improves several magnesium alloys properties. Addition of aluminium up to 5 wt.% makes the grain size of cast alloys to drop significantly. The so called AZ alloys contain aluminium and zinc and are widely used for light structural components in several commercial applications.

3.1.2.2 Corrosion behavior

Magnesium is usually considered to have a poor corrosion behavior. This behavior is one of the reasons that make magnesium a good candidate for biodegradable implant applications. As corrosion mechanisms depend greatly on the environment, then for biomedical applications, corrosion behavior has to be investigated in a body fluid. In addition, specific mechanisms involving bacteria or living cells are also expected. These aspects of *in vivo* corrosion must certainly be considered but are presently out of the scope of the study. The present work will be limited to studying the corrosion resistance in a simulated body fluid[1]. However, in this fluid, the general types of corrosion mechanisms expected to occur are similar to the ones encountered in aqueous solutions as it will be described in the following section.

Electrochemical aspects

The corrosion of a metal is due to an exchange of electron between the material and an external chemical compound (for review on metal and alloy corrosion see [66] [67], more specifically on magnesium alloy corrosion see [68] [69]). After establishment of a dynamic equilibrium of the corrosion reaction, a double-layer capacitor can appear. It is formed by two charged layers, one in the material due to the dissolution of the metal and the other at the surface in the solution by attraction of ions to the surface. Then, potential difference exists between these two layers. The potential difference

[1] A simulated body fluid usually contains the following ions: sodium, potassium, calcium, magnesium and chloride. Their concentrations are close to the one in human blood plasma.

measured between pure metal sample in standard conditions[2] and a stable reference electrode is called standard electrode potential. It represents the tendency of a metal to be oxidized: for low value of this potential, the equilibrium is displaced on the side of oxide production. The standard potential (versus hydrogen) for magnesium (−2.37 V) is low compared to other metals like silver (0.8 V), aluminium (−1.7 V) or iron (0.56 V). This means that magnesium is highly reactive and has a high tendency for oxidation. Due to this high reactivity, when magnesium is in contact with an aqueous solution the following reactions occur:

$$Mg_{(s)} \rightarrow Mg^{2+}_{(aq)} + 2e^{-} \qquad \text{(anodic reaction)} \qquad (3)$$

$$2H_2O_{(l)} + 2e^{-} \rightarrow 2OH^{-}_{(aq)} + H_{2\,(g)} \qquad \text{(cathodic reaction)} \qquad (4)$$

$$Mg^{2+} + 2OH^{-} \rightarrow Mg(OH)_{2\,(s)} \qquad \text{(product formation)} \qquad (5)$$

All these equation can be combined under the following overall reaction:

$$Mg_{(s)} + 2H_2O_{(l)} \rightarrow Mg(OH)_{2\,(s)} + H_{2\,(g)} \qquad \text{(general reaction)} \qquad (6)$$

Depending on environmental parameters such as temperature, pH, activity of the species in solution or ion adsorption on the surface; the kinetics of these reactions can be significantly modified [70].

To summarize, magnesium corrosion is accompanied by hydrogen gas release and the formation of hydroxide compounds may produce a film on the surface, (Equation (6)). When this film is formed under atmospheric conditions; the surface of a magnesium sample turns to grey. Under standard atmosphere and in a high alkaline solution (pH $>$ 10.5) this film is stable [71] [72]. Under other conditions this film is usually unstable due to various phenomena. First, the misfit between the magnesium crystal structure and its hydroxide induce stresses in the film layer which can lead to cracks in the film [73]. Also, the production of hydrogen can lead to decohesion of portions of the film for the immersed samples [73]. Lastly, in aqueous solutions containing chloride, the film is dissolved letting the surface free for corrosion [73]. Nevertheless, due to the high attractivity of magnesium as a

[2] Standard conditions correspond to pure element sample in molar solution of the metal ions under 1 bar pressure.

structural metal, many efforts are done to improve its corrosion behavior which is frequently achieved by surface treatments. The degradation mechanisms of magnesium and magnesium alloys will be described hereafter.

Degradation mechanisms

Corrosion mechanisms can be divided into two categories: general corrosion (also called uniform corrosion) and localized corrosion. Both categories have been reported for magnesium alloys. Figure 17 shows a schematic representation for several possible corrosion mechanisms in magnesium alloys.

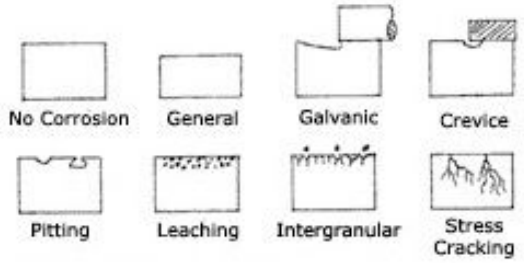

Figure 17: Schematic representation of different types of corrosion in magnesium and magnesium alloys [74].

A general corrosion is, as indicated by its name, a corrosion occurring homogeneously on the entire surface of the sample. This kind of corrosion is governed by the kinetics of the corrosion reactions and/or by the diffusion process [66]. For a naked metal, without any corrosion product, if the adsorption of reactive elements on the surface is fast, the corrosion rate is determined by the slowest chemical reaction. But if the corrosion products are not dissolved and begin to form clusters and finally a film, the adsorption of ions to the surface will be more difficult, then the corrosion rate can slow down. The film on the surface can be protective with efficiency depending on film resistance and porosity. For example, the good corrosion resistance under air atmosphere of Mg-Al alloys can be attributed to the formation of an effective protective film [68].

Localized corrosion usually occurs due to heterogeneities in the material. In magnesium alloys, the most common phenomenon with a high detrimental impact on corrosion resistance is the micro-galvanic effect due to the alloying elements. Pure magnesium is usually alloyed to improve its mechanical properties by solid-solution, precipitation or particle strengthening. However, from a chemical point of view, the

microstructural heterogeneities resulting from the added elements (clusters, precipitates, second phase particles) are usually more cathodic than magnesium. Therefore, a micro-galvanic cell can be formed between the magnesium matrix and the precipitates [75]. The particles play the role of cathodic areas with magnesium dissolution occurring at the interface. This kind of corrosion can finally cause the fall out of the particles [68]. Due to this micro-galvanic effect, second phases present in the magnesium matrix could lead to a rapid degradation [75].

A particular localized corrosion mechanism occurring in magnesium is pitting. As previously mentioned, the corrosion product film may not be stable. When at some point, the film breaks, the naked material is in direct contact with the solution, allowing for ion exchange [76]. This naked area becomes anodic and the dissolution of the metal occurs; the large area covered with the film behaves as cathodic area [76]. Pitting may also occur from the preferential corrosion of the second phase areas. In Mg-Al industrial alloys, where second phases like AlMn, AlMnFe, $Mg_{17}Al_{12}$ or Mg_2Cu act as cathode, pitting corrosion may also be observed [75]. When micro-galvanic corrosion occurs for precipitates or element segregation at grain boundaries, it is called intergranular corrosion. Microstructural characterization of the sample surface may allow identifying a pitting mechanism or an intergranular corrosion.

Protective coatings

In spite of the possible adjustment of alloy composition to improve corrosion resistance, magnesium alloys may remain very reactive in various environments. Then the formation of a barrier on the surface is a way to protect the material from the environment.

For an industrial application, two main techniques of coating preparation are used [77]: chemical or electrochemical treatments (this process is called passivation) or deposition of chemical compounds (usually organic ones). One can note that a chemical conversion of the surface is usually done as a pre-treatment for an organic coating in order to improve its adhesion to the surface [78]. Chromic based solutions have been extensively used to provide a high adhesion to the surface for organic coatings [68]. A full range of polymer paints (epoxy, phenolic, vinyl, polyester, etc.)

have been developed for corrosion protection and also protection against scratches [79].

The coatings presented above have been designed for industrial applications and cannot be directly applied for biomedical uses. In most cases, these coatings contain compounds that are not safe for biomedical applications. Coatings for biomedical applications require very specific developments depending on the aim and the problem that is addressed. There is abundant information in the literature on magnesium alloys coatings for biodegradable applications [80]. The major part focuses on inorganic coating obtained by chemical or electro-chemical conversion of the surface of the alloys. For instance, fluoride-containing coatings have shown their ability to reduce the degradation rate of Mg-based alloys [81] [82]. Other coating methods have also been investigated like chemical vapour deposition, plasma spraying, ion implantation (for metallic coatings or spin coating), dipping, self-assembled monolayers for organic coatings [80]. Wong et al. have reported a reduction of the degradation rate using a polymer-based membrane with various pore size, deposited layer-by-layer using a spraying device [83].

Thus, there are many different kinds of coatings and many possibilities to form a coating. Coatings can be used to control the degradation rate, enhance cell adhesion or cell activity; few studies have also shown the possibility for organic coating to be used as drug delivery systems [80]. As a matter of fact, in the present work, the goal of the surface modification is more to enhance the surface properties for the implant integration rather than to control the corrosion rate.

3.2 Bone structure and bone healing

3.2.1 Bone composition

Bones display a unique architecture made of an organic matrix, a mineral substance and cavities. These three constituents, in combination, respond to the mechanical stresses from the environment. The mass-to-strength ratio of bones is optimized by natural processes of modeling and remodeling. Depending on their location, bones have various structures. As an example, the inside structure of a bone is very

heterogeneous. In addition, the microstructure evolves with sex, age, activities, etc... [84] However, one can consider that, on average, bones are composed for 35 % of organic matrix (mostly collagen fibrils (90 %)) and 65 % of mineral substances. Collagen fibrils are organized as concentric lamellae, forming a cylinder called osteon (Figure 18). This complex microstructure of collagen fibrils contributes to the tensile strength and flexibility of bones. The mineral substance of a bone essentially consists of a calcium phosphate: $Ca_{10}(PO_4)6(OH)_2$ called hydroxyapatite (HAP). The HAP crystals which are aligned along the axis of the collagen fibrils contribute to the bone strength [85].

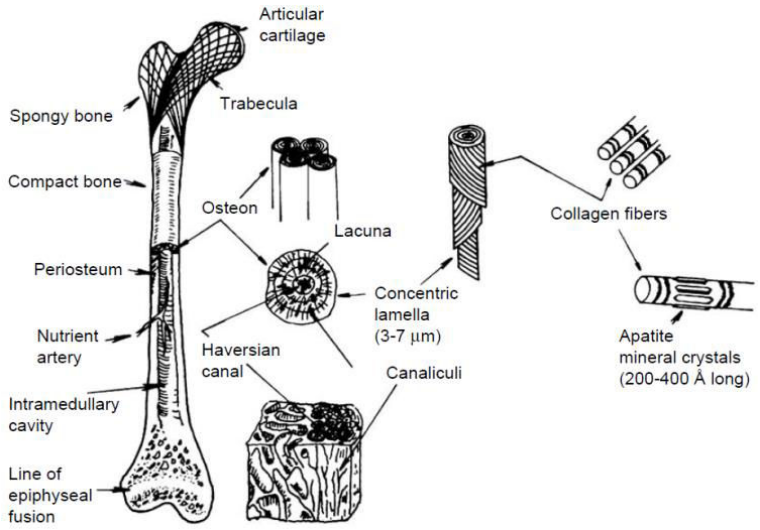

Figure 18 : Structural organization in a human long bone [86].

3.2.2 Bone healing process

When a bone breaks, a complex restoration process takes place at the fracture location. A brief description of the main steps of this process will be given in the following part. Figure 8 describes the healing process of a broken bone. During healing, four different steps can be distinguished: 1- hematoma formation, 2- fibrocartilaginous callus formation, 3- bony callus formation and 4- bone remodeling [10].

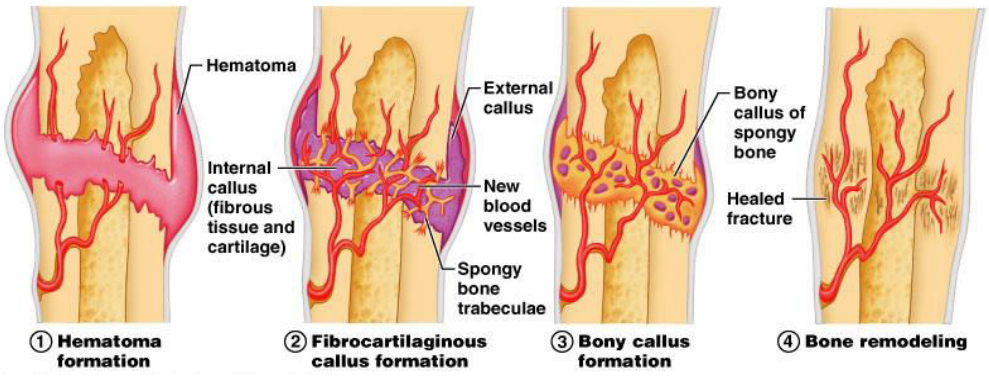

Figure 19: Bone healing process [87].

The first step, (1), occurs shortly after the fracture. It corresponds to an inflammatory response identical to the response happening for any injury in the body. There is an increase of blood flow that allows for the migration of various cells at the periphery of the bone. It is worth noting that during this step an infection has the highest probability to occur, especially in case of an open fracture. To prevent such scenario, antibiotics are frequently used. The standard medical treatment is drugs (antibiotic) but antibacterial coatings are innovative ideas presently under consideration. For instance, silver coatings are developed to be used as bactericidal on medical implants. Silver coatings have been shown to prevent bacterial adhesion or colonization [88]. The inflammatory activity has a peak within 24 H and is complete after 7 days [89]. During the second step, (2), there is cell proliferation and differentiation followed by the production of new fibrous connective tissue matrix (in particular collagen fiber). This new tissue is called soft callus. This tissue cannot support load application during the first 4 to 6 weeks of the healing process. During the third step, (3), the soft callus becomes stiffer and is transformed into the hard callus. The stiffness of the healing part results from the calcification of the soft callus, which is due to the deposition of HAP crystals on the collagen part. Consequently, bone slowly replaces the soft callus. This stage of repairs lasts several weeks. At this point, the architecture of the bone is not perfect but the main mechanical properties are restored. The last step, (4), could last several years during which the bone is slowly remodeled upon experiencing mechanical stresses to improve the mass-to-strength ratio.

Based on the severity of the injury, bones may need to be re-aligned and restrained in mobility. The mechanical stability is obtained using devices (plates, rods, screws

and pins). The devices are placed in order to obtain immobilization of the bone fragments with the smallest gap between the injured sections. Because of the close contact of bone fragments, the first steps, (1), (2) and (3), of the healing process is reduced. The amount of soft callus (and thus hard callus) to be formed is minimal and may even not occur during this healing process. Thus the bone may heal directly following the natural process of remodeling. As a result, the process to renew the bone architecture is faster than without bone fixation. As displayed in Figure 20, depending on location the consolidation process last from 30 days to 120 days.

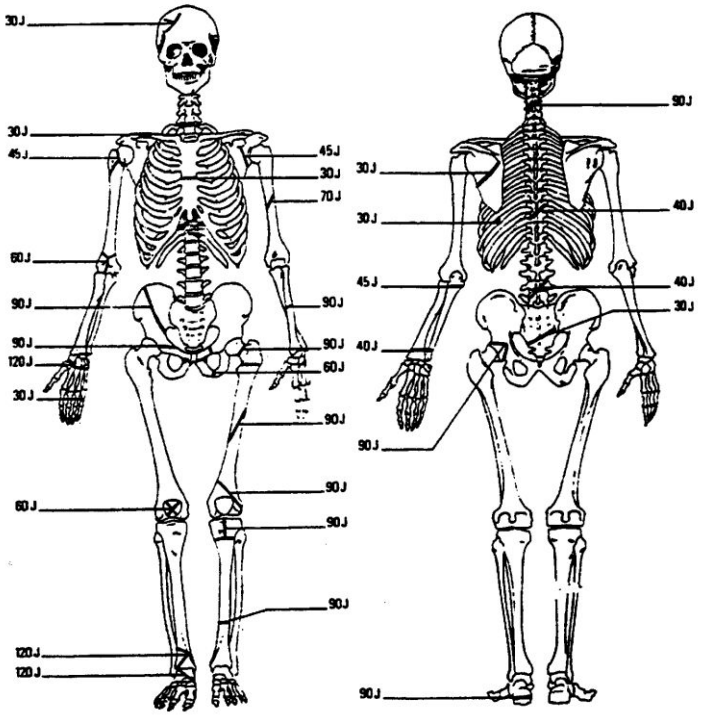

Figure 20: Average healing time for bones depending on their location, J=jours=days [90].

3.2.3 Stress shielding effect

Using a fixation system for bone healing may lead to a complication called stress shielding. Stress shielding is a medical name for the reduction of bone density that results of the screening of the stresses during healing due to the presence of the implant. This can be described for an orthopedic fixation as illustrated in Figure 10: the implant, stiffer compared to the bone, will support the majority of load.

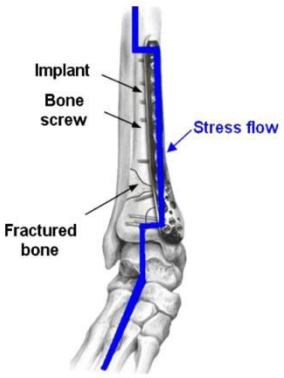

Figure 21: Schematic presentation of stress shielding effect due to an orthopaedic implant [91].

Practically, it means that the stress distribution applied to a bone is modified in presence of an implant. The higher is the Young's modulus of the implant compare to the one of the bone, the lower is the stress supported by the bone. The stress repartition has a direct consequence on the bone reconstruction process. Bone is naturally remodeled in response to stresses applied to it. So if the stress applied to the bone is mainly supported by a device, the bone does not have enough stress stimuli. Bone is then remodeled as if no stress applied which results in a reduction of bone density. The Young's modulus for stainless steel is usually around 200 GPa, common titanium alloys are about 115 GPa which is much higher than the 20 GPa for the cortical modulus bone [92], [93]. Thus using these materials may reduce the density of bone close to the implant. Among all the metals, magnesium is the one with the lowest Young's modulus: 40 GPa. Thus, among the metal based system, magnesium alloys are promising candidate to reduce the stress-shielding effect. In addition, as presented below, magnesium has other interesting properties for degradable implant application.

3.3 Magnesium for degradable implant applications

3.3.1 Magnesium: a promising candidate

Biocompatibility of magnesium

Magnesium is well tolerated by the body: according to current medical recommendations, the recommended dietary allowance of magnesium is about 400 mg

per day [94] and in case of excess, it would be well excreted by the urine. Magnesium has been earlier experimented as orthopaedic implants [9] and as stent products [95].

Degradability of magnesium

Degradability is the core property for a degradable implant. Magnesium is well known for its corrosion activity in an aqueous media. Thus, magnesium can be easily degraded *in vivo* but the degradation must not be too fast. With its degradation, the implant has to ensure the complementary mechanical support for the injured area until the recovery of the bone occurs. In that regard, the degradation rate of an implant should match with the consolidation process time (variable over a period from 1 to 12 months [15] [96] [97]).

Suitable mechanical properties

With magnesium Young's modulus being comparable to that of the human bone, the stress shielding may be reduced [98]. Magnesium is then more appropriate than other metallic materials for orthopaedic implant. Still bulk modulus represents only a part of mechanical properties, strength is also an important issue for load bearing applications. Therefore, a magnesium implant should have strength in a similar range compared to bones. Indeed though magnesium appears as a promising material for degradable implant applications, improvement of mechanical behavior is still required.

The first part of the project is focused on the improvement of mechanical and corrosion behavior that will be carried out by modifying the microstructure of the bulk material by thermomechanical processing. The second part of the project is focused on the functionalization by surface treatment in order to improve the interaction with the body and enhance the healing process.

3.3.2 Alloy selection: Mg-Ca

A major consideration for degradable implants is to have a harmless interaction with the body of the patient. In order to choose the best candidate alloy, a selection strategy based on the toxicity of the element has to be done. Table 4 displays the toxicity limit of the typical solute element for magnesium alloys.

Table 4 : Toxicity limits for typical alloying elements usually used with Mg [93].

Element	**Daily allowable dosage** (mg)
Al	14
Be	0.01
Ca	1400
Cu	6
Fe	40
Ni	0.6
RE	4.2*
Sn	3.5
Sr	5
Ti	0.8
Y	0.016*
Zn	15

*Denotes that the total amount of the rare earth elements: Ce, La, Nd, Pr and Y should not exceed 4.2 $mg.d^{-1}$.

According to Table 4, the daily body tolerance limit is very variable from one element to another. High toxicity elements like beryllium, nickel, titanium and yttrium have to be avoided or kept under a very low level. In addition, some solute elements have to be discarded for other reasons: for instance iron and copper are known to be detrimental for the corrosion resistance of magnesium alloys [65]. In commercial alloys, these elements are kept below very low critical level to avoid severe corrosion: 20 - 50 ppm for iron and 100 – 300 ppm for copper [22].

After the above selection, only four elements remain: calcium, tin, strontium and zinc. Strontium has been shown to reduce the grain size of a Mg-Sr alloy (with Sr content up to 1.5wt.%) but the effect on the mechanical properties is not sufficient for load bearing applications [99]. Tin addition improves the mechanical behavior but has a toxic effect on osteosarcoma cells [100]. Concerning the last two elements: Zn and Ca, calcium has a higher tolerance limit in the body than zinc: about one hundred times higher (Table 4). Calcium is well known as a major element of bones: an adult bone is composed of 30 to 40 wt.% of calcium[3] [101]. In addition to the body tolerance issue, calcium has multiple positive effects on magnesium:

- calcium may also promote the healing process with the formation of hydroxyapatite crystals [102]

[3] Composition from analysis of bone ash.

- calcium may increase the strength by solution strengthening and/or precipitation hardening [22]
- calcium improves the fabrication of magnesium by reducing the oxidation and facilitating the metallurgical process [103]

Thus, calcium is a highly promising alloying element for magnesium for degradable implant applications. In the present work, it has been chosen to investigate the Mg-Ca binary system with the lowest amount of impurities. The material studied in this project has been prepared by CanmetMATERIALS (Canada). The alloy was cast as cylinder ingot of 1.5 inch diameter. The composition of the cast alloy is reported in Table 5.

Table 5: Composition of the Mg-2wt.%Ca alloy of the cast ingot.

	Mg	Ca	Zn	La	Ce	Al	Si	Cu	Fe	Mn
wt.%	(balance)	2.5	0.026	<0.05	0.015	<0.01	0.006	<0.005	<0.005	<0.005
at.%	(balance)	1.53	0.02	<0.005	0.003	<0.01	0.005	<0.002	<0.002	<0.002

The magnesium-calcium binary phase diagram displayed below shows that only one Mg-Ca intermetallic is expected, namely the Mg_2Ca C14 Laves phase, Table 6.

Table 6 : (a) The Mg-Ca phase diagram [104] and (b) structural properties of the phases of a Mg-Ca system.

Mg-Ca system

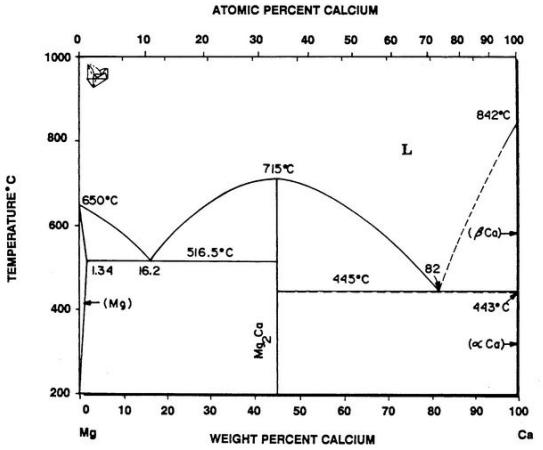

(a)

	Phase	
	Mg	Mg_2Ca
Structure	hP2	hP12
a (Å)	0.320*	0.626*
c (Å)	0.520*	1.015*

(b)

*Values from Pearson's Crystal Data [105]

The cast material shows a typical casting microstructure with large dendrites separated by the Mg-Mg_2Ca eutectic mixture in the interdendritic areas, Figure 22 (a). The eutectic structure is made of alternated Mg and Mg_2Ca phase lamellae, Figure 22 (b). The dendrites and eutectic mixture are separated by a halo of Mg_2Ca phase with an approximate thickness of 0.5 µm. The thickness of the Mg and Mg_2Ca lamellae in the eutectic structure is also about 0.5 µm. The eutectic phase represents a volume fraction of 0.08 according to image analysis consistent with the 2wt.% of calcium.

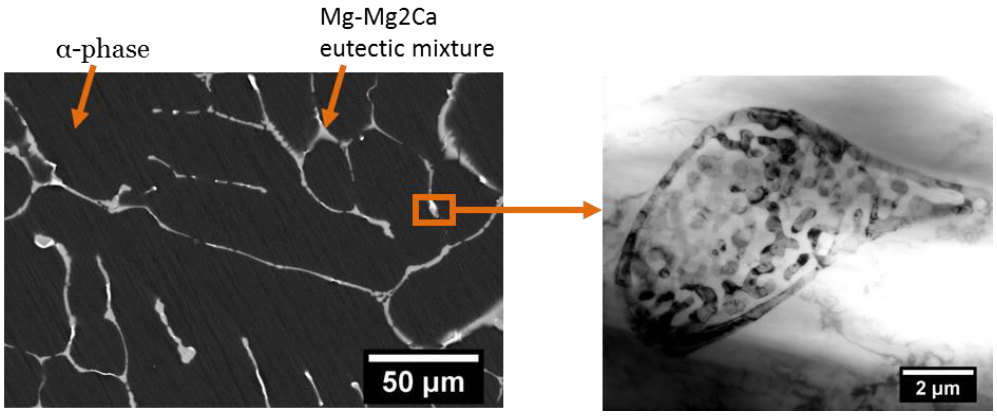

(a) (b)

Figure 22: (a) SEM image of cast material formed with backscattered electron detector, bright area correspond to the eutectic mixture. (b) TEM image, bright field image of a eutectic mixture in an interdendritic space, Mg_2Ca phase appears in dark contrast.

***

In the general introduction, it has been described that magnesium and magnesium alloys are mainly used in structural applications. For these applications, mechanical properties and corrosion behavior of magnesium and magnesium alloys have been investigated. A novel field of application would take advantage of magnesium properties: degradable implants. However, a sufficient reduction of the degradation rate of magnesium and magnesium alloys still need to be achieved. In addition, the *in vivo* framework needs to be taken into account. In this context the general goal of the present project is the development of an Mg-Ca alloy for this application. A two steps strategy has been set-up: bulk optimization and surface functionalization.

To achieve the first objective, different thermomechanical processing will be used. The impact on mechanical properties and corrosion behavior will be evaluated by classical methods. Microstructural characterization will also be carried out to make the link between the microstructure tailoring produced by the various thermomechanical processing and the optimization of mechanical properties and corrosion behavior.

The second objective is the functionalization of the surface of the previously optimized material to provide the implant with an antibacterial effect. An additive manufacturing technique will be used to deposit silver nanoparticles on the alloy surfaces. Then, a laser treatment will sinter the deposition to ensure a better

adhesion of the deposition. Microstructural characterizations of the deposited layer will be carried out to control the pattern quality. Finally, a finite element modelling will be developed to help further optimization of deposition and sintering parameters.

These two steps could be seen as two different parts of the present project: the first objective targeting a bulk optimization and the second objective targeting a surface functionalization. Then, the literatures as well as the methodology used for each part are independent. In order to make the reading easier, it has been chosen to separate the present manuscript in two parts: each part focusing on one objective of the present work. Thus, at the beginning of Chapter 3 and 4, the specific literature on the associated part will be reviewed.

4. Property optimization by thermomechanical processing

The first part of the present work has been focused on the thermomechanical processing methods and their impacts on the mechanical and corrosion properties. Microstructural characterizations have also been performed in order to get some understanding of the properties evolution. The aim of this part was to identify solutions to optimize both mechanical and corrosion behavior of Mg-2wt.%Ca alloy for degradable implant applications. In this chapter, first the literature on the optimization of these properties for Mg-Ca alloys will be reviewed. Then, the results concerning the impact on these properties by the selected thermomechanical processing will be presented.

4.1 Focused literature review

4.1.1 Mechanical behavior of Mg-Ca alloys

As described in Section 2.1.2, alloying and utilization of thermomechanical processing are the main methods used to modify the mechanical properties of magnesium and magnesium alloys. In the present work, it has been chosen to use a magnesium-calcium alloy. Thus, in the present section, the literature focused on the modification of mechanical properties of magnesium-calcium alloys will be reviewed.

Concerning the Mg-Ca alloy of interest here, the calcium solubility decreases in magnesium with a decrease of temperature, Table 6. Thus, the precipitation effect as presented in Section 2.1.2 may occur. Indeed, a moderate precipitation hardening has been reported in Mg-Ca alloys [23] [106]. Increasing the calcium content above 0.7 wt.% encourages the formation of an eutectic structure in the alloy [30].

During solidification, there is an enrichment of calcium at the solidification front which leads to the formation of the eutectic phase Mg+Mg_2Ca. Thus the formation of this eutectic structure refines the microstructure of the cast alloy. Higher percentage of calcium will allow the formation of a finer microstructure [30] [107]. However, it has been reported that for calcium content above 5 wt.%, the resulting alloy is very brittle at room temperature [102].

For Mg-Ca alloys with 0.5, 1.0, 1.5 and 2.0 wt.%Ca, extruded at 623 K with a ratio of 20, Murakoshi et al. [108] have observed a beneficial impact of calcium content on the mechanical properties. As summarized in Table 7, by increasing the calcium content Murakoshi et al. have measured an increase of the ultimate tensile strength and the proof stress. They have also measured higher ductility of these extruded Mg-Ca alloys by increasing the calcium content from 0.5 to 1 wt.%; however, for calcium content above 1 wt.% a slight decrease can be noted. Concerning the microstructure, a finer grain size with higher calcium content for the extruded material has been observed. However, Murakoshi et al. did not investigate the possible relation between the microstructure and the mechanical properties.

Table 7: Mechanical property of extruded magnesium-calcium alloys with different calcium content at room temperature [108]

Ca content /wt%	UTS /MPa	Proof stress /MPa	Strain ε
0.5	260	30	0.07
1.0	310	32	0.13
1.5	316	45	0.11
2.0	316	50	0.11

In agreement with the above results, Harandi et al. [30] has reported a hardness increase in Mg-Ca alloys with increasing Ca content: 27 Hv for pure magnesium to 47 Hv for Mg-4wt.%Ca. They have attributed this increase to a solid solution effect associated with grain size refinement and also to the distribution of Mg_2Ca intermetallic phase.

For a series of Mg alloys with different calcium content and extruded using the same conditions (350 °C, ratio 7.5), Drynda et al. [107] have observed the impact of Ca content on the mechanical properties of Mg-Ca alloys. It is important to note that Drynda et al. have observed similar grain sizes after extrusion for different alloys,

namely grain size ranging from 5 to 30 µm. The grain refinement effect of calcium has been observed only in cast materials. As illustrated in Figure 23 (a), in the range of calcium content studied by Drynda et al., increasing the calcium content increases the tensile strength from 200 MPa (pure Mg) to 240 MPa (Mg-4wt.%Ca) and the 0.2 % proof stress also steadily increase from approximatively 100 MPa (pure Mg) to 200 MPa (Mg-4wt.%Ca). However, it is shown (Figure 23 (b)) that the ductility increases for Ca content up to 1wt.%. At higher content, the ductility decreases down to lower values than pure magnesium.

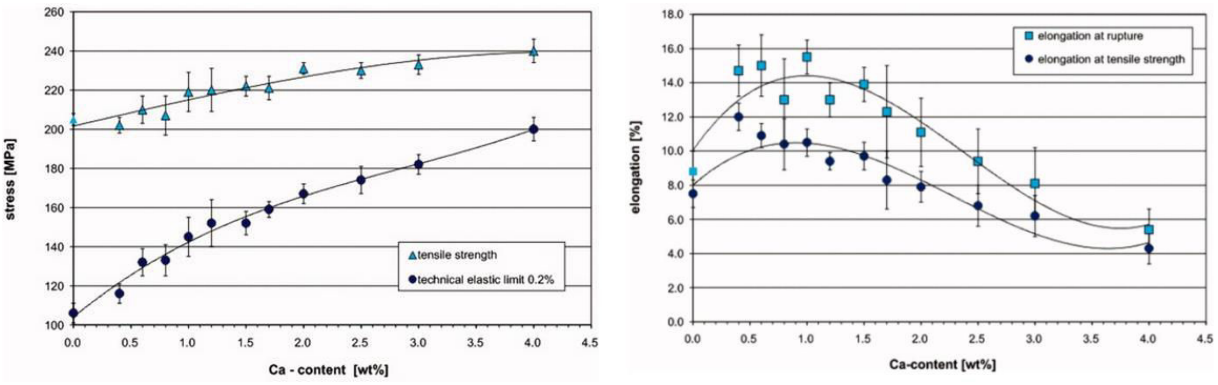

(a) (b)

Figure 23: Evolution of the mechanical properties of the Mg-Ca alloy with the Ca content [107].

Both Murakoshi et al. and Drynda et al. have investigated the mechanical properties after extrusion of magnesium-calcium alloys. They have shown that up to a certain limit (around 1 wt.%), calcium allows to increase the mechanical properties of the alloy.

Li et al. [102] have studied the effect of thermomechanical treatment on the mechanical and corrosion properties of a Mg-1wt.%Ca alloy. Either by hot rolling (60 % reduction at 400 °C) and hot extrusion (210 °C, ratio 17), the mechanical strength is improved (Figure 24). Such higher strength can be related to the refinement of grain size resulting from thermomechanical processing. For Mg-2wt.%Ca and Mg-3wt.%Ca, Li et al. [102] have observed the formation of Mg_2Ca phase. However, contrary to the previous studies, this increase of calcium content did not improve the mechanical strength (Figure 24).

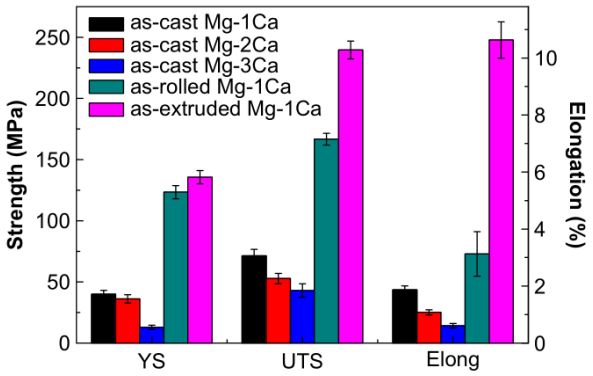

Figure 24 : Tensile properties of as-cast Mg-xCa alloy for x = 1, 2, 3wt.% and as-rolled Mg-1wt.%Ca alloy and as-extruded Mg-1wt.%Ca alloy [102]

Han et al. [109] have used extrusion to improve the mechanical behaviour of a Mg-5wt.%Ca alloy. After hot extrusion (350 °C, ratio 25), compressive tests have shown a large increase of both the yield strength and ultimate compressive strength (150 MPa and 202 MPa to 180 MPa and 393 MPa, respectively). Han et al. have associated this evolution to the grain refinement and the fragmentation of network of brittle eutectic mixture.

Equal channel angular pressing

One of the thermomechanical processes used in the present study is equal channel angular pressing (ECAP). This non-conventional processing will be described first and then the general considerations of ECAP on magnesium and its alloys will be reported. To the knowledge of the author, the ECAP process on magnesium-calcium alloy has not been reported in the literature.

ECAP is a severe plastic deformation processing. This technique is highly attractive for its high level of deformation possible by shearing due to the angle of the inner die. A schematic representation of an ECAP system is shown in Figure 25.

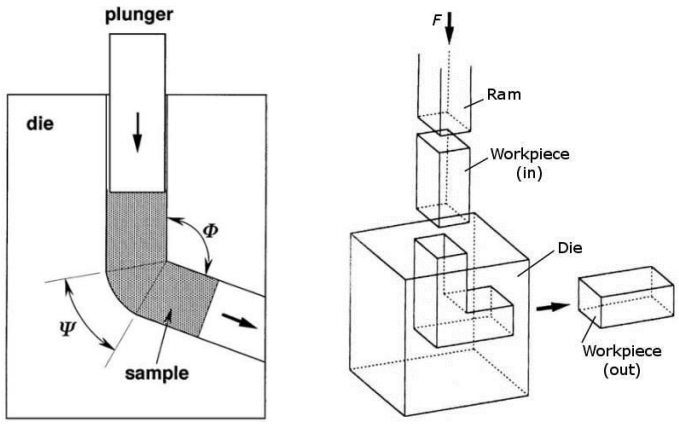

(a) (b)

Figure 25: (a) A section through an ECAP die showing the two internal angles φ and Ψ [110] and (b) a schematic representation of an ECAP system with φ = 90° and Ψ = 0° [Adapted from [110]].

As described in Figure 25 (a), the inner die shape is defined by two angles: φ and Ψ. The equivalent strain, as a function of the total number of passes N and the angles φ and Ψ, has been established by Goforth R. E., [111], see Equation (7):

$$\varepsilon_N = \frac{N}{\sqrt{3}}\left[2\cot\left(\frac{\varphi+\Psi}{2}\right)+\Psi\right] \qquad (7)$$

ECAP maintains the sectional area of the sample during the processing allowing repeating the processing several times. Between each pass, the rotation applied to the sample defines the process route: route A no rotation, route B_A the sample is alternatively rotated by + 90° and - 90°, route B_C the sample is rotated by 90° and route C the sample is rotated by 180°, Figure 26 [110]. The combination of these rotations described the route of the process [112]. Using different routes may result in a different evolution during the processing [110].

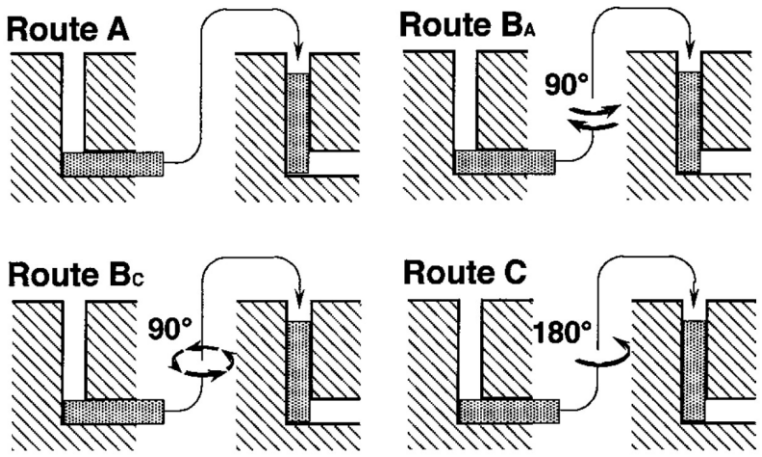

Figure 26: The four different processing routes which may be used for repetitive pressings [110]

ECAP processing is usually done at a high temperature (250 °C) due to low deformability of magnesium at room temperature [113]. Since high temperature promotes grain growth, submicron grain sizes are difficult to obtain especially for low grade alloys [113] [114]. To allow lower processing temperature, other processing procedures have been investigated. For instance, applying a back-pressure to process by ECAP has been investigated by Lapovok et al. [115]. By applying 44 MPa back-pressure, Lapovok et al. have been able to process by ECAP an AZ31 cast alloy at 200 °C. After 6 passes, Lapovok et al. obtained an equiaxed microstructure of fine grain size ranging 1 to 3 µm. Sequential temperature reduction has been investigated by Mussi et al. [116]. Decreasing gradually the temperature from 265 °C to 150 °C for each pass in a total of eight, Mussi et al. have reported a 0.5 µm grain size for an AZ91 alloy. Thus, even with low temperature, submicronic grain sizes are difficult to obtain.

Different explanations have been given for the microstructure refinement process [117] [118] [119]. However, experimentally all the routes allow to refine the grain size, but the route B_C was proven to be more efficient for dies with $\varphi = 90°$ [120]. Nevertheless, the route used in the process will also have an impact on the second phase if a second phase is present in the material. The different routes activate different shear planes based on the number of passes with routes A and C having redundant strain [120], Figure 27. Furukawa et al. [117] have investigated the impact of the different routes on a cubic element and have concluded that routes A

and B_A involve a higher deformation than routes B_C and C. Thus, these routes may have a high impact on the second phase morphology and distribution.

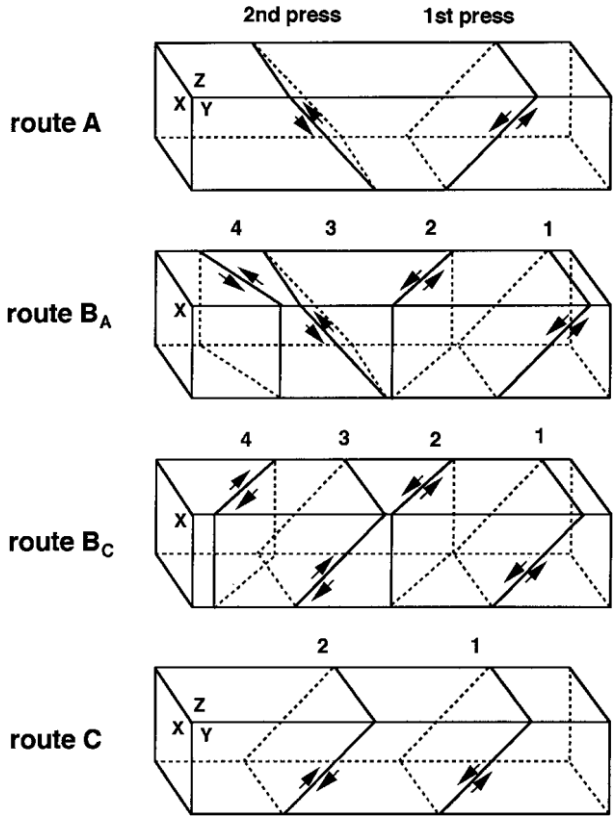

Figure 27: Shear strain planes for each ECAP route for a die with φ = 90° [110].

Nevertheless, besides route and temperature, the number of passes is also important for the microstructure evolution during ECAP processing. For magnesium alloys, it has been suggested the existence of an initial critical grain size, above which, a partial recrystallization would occur [119]. Under this size, a homogeneous distribution of fine grain could be obtained [119]. Increasing the number of passes may then first partially recrystallize the coarse cast microstructure which could then be as the passes continue [119]. For instance, for an AZ31 alloy, 6 passes were necessary to reduce the grain size from 10 µm to 1.5 µm; when only one pass was sufficient to reduce the extruded microstructure of a ZK60 alloy from 3 µm to 1 µm [119]. In other terms, beginning with a finer microstructure would reduce the number of passes required to obtain a homogeneous fine grain microstructure by ECAP processing. Other studies in the literature report the utilization of conventional extrusion to refine the microstructure prior to ECAP [114] [121] [122].

In addition to grain size effect, ECAP may also impact the texture of the material. However, the relationship between the ECAP process conditions and the texture evolution is not completely clarified. Beausir et al. [123] have reported the possibility to obtain similar texture with the routes A, B_C and C with the c axis perpendicular to the extrusion direction. Another study reports a preferred orientation with a 45 ° inclination of the basal plane to the extrusion direction for magnesium alloy AZ31B processed by ECAP with route B_C [28]. Kim et al. [124] suggest that increasing the number of passes from 2 - 4 to 8 may increase the preferable orientation of the basal plane (45 ° to the extrusion direction). Yoshida et al. [125] have reported different texture on an AZ31 alloy after 4 passes of ECAP processing at different temperatures: a 45 ° inclination of the basal plane to the extrusion direction at 250 °C and the basal plane parallel to the extrusion direction at 300 °C.

4.1.2 Corrosion behavior of Mg-Ca alloys

As previously described, the solubility of calcium in magnesium is low. Thus, the Mg_2Ca intermetallic compound is formed in magnesium-calcium alloys with low Ca content. In the general literature review, Section 2.1.2, it has been mentioned the microgalvanic effect between the matrix and the second phases could occur in magnesium alloys. Usually, the second phases formed in magnesium alloys are more cathodic than the matrix of magnesium. In magnesium-calcium alloys, the intermetallic, Mg_2Ca, is more anodic than Mg which differentiates magnesium-calcium from the other magnesium alloys [32] [126]. However, even if the intermetallic compound is more anodic than the matrix, the presence of this second phase has an impact on the corrosion resistance.

At room temperature, for calcium contents under the solubility limit, an increase of the corrosion resistance of magnesium has been reported [127]. However, above the solubility limit, magnesium-calcium alloys have shown high corrosion rate [30] [107]. This is clearly shown by the plot in Figure 28.

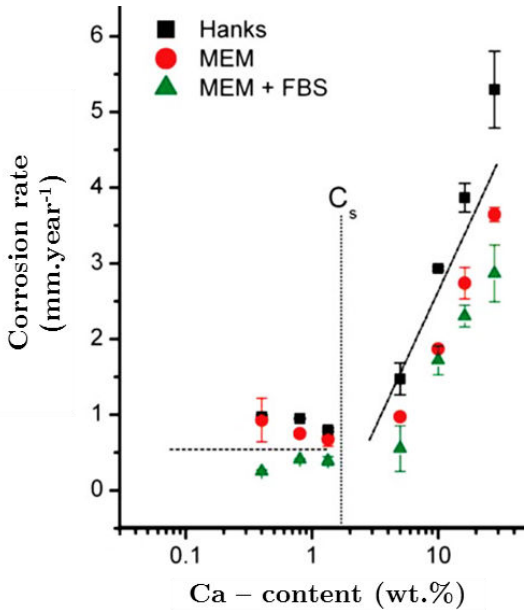

Figure 28: Evolution of the corrosion of magnesium-calcium alloys as a function of the calcium content and in different corrosion media[4]. Adapted from [128].

Kirkland et al. [129] have measured the corrosion rate by mass loss test for a series of alloys with various Ca contents (Mg-0.4wt.%Ca to Mg-16.2wt.%Ca) and concluded a two regimes behaviour. Above a critical Ca content, being in the 1 to 5 wt.% range, the corrosion rate rapidly increases. Kirkland et al. mentioned a possible effect of local galvanic corrosion due to intermetallic phases that form when the Ca content is above the solubility limit. However, it is interesting to note that a similar corrosion rate has been obtained for highly different calcium contents: 5 wt.% and 16.2 wt.%. Bakhsheshi Rad et al. [130] have reported the same tendency by potentiodynamic and immersion tests in a simulated body fluid with an increase of the corrosion rate by increasing the Ca content from 0.5 wt.% to 10 wt.%. However, in addition to the Mg_2Ca formation, Bakhsheshi Rad et al. have noted that the Ca addition also leads to a grain size and dendrite cell refinement.

In addition to the composition heterogeneities, microstructural features may also play a role in the corrosion behavior of an alloy. For mechanical behavior, it is well known that properties are affected by microstructural features like grain size, crystallographic texture, dislocations density, twin density, etc. For corrosion behavior, though second phase particles can be expected to have an effect through

[4] Corrosion media: Hanks is the Hanks Balanced Salt Solution, MEM is a Minimum Essential Medium and MEM+FBS is a Minimum Essential Medium containing foetal bovine serum.

micro-galvanic corrosion, the impact of other micro-structural features is not so clear. For instance, the effect of grain size is rather well documented for magnesium and magnesium alloys but does not lead to general conclusion. Birbilis et al. [34] have reported an increase of the corrosion resistance of pure magnesium by reduction of grain size using ECAP processing. Birbilis et al. suggest that the combination of both high misorientation angle and high density of grain boundaries due to the small grain size (2 µm to 6 µm) has improved the stability of the oxide layer. Alvarez-Lopez et al. [35] have suggested the same interpretation for the higher corrosion resistance of an AZ31 alloy with a small grain size (5 µm) compared to a larger one (26 µm).

On the other hand, increase of the corrosion rate has been observed when decreasing the grain size. For instance, an ultra-fine grain WE43 alloy ($<$ 1µm) obtained by ECAP processing has shown a higher degradation rate in a simulated body fluid than without ECAP and with a larger grain size (7 µm to 15 µm) [131]. The authors suggested that the higher density of grain and interphase boundaries may be responsible of this increment. Idris et al. [132] have reported that forging a Mg-1Ca alloy reduced the grain size of the alloy but increased the corrosion rate in a simulated body fluid. However, Idris et al. have also reported an increase of the twinning planes by forging. In another publication, Aung et al. [36] have reported that the existence of twins may accelerate the corrosion of an AZ31B alloy.

Wang et al. [16] have used hot rolling on an AZ31 alloy to reduce the dendritic structure (average grain size equal to 450 µm) into a uniform microstructure with an average grain size of 20 µm. Wang et al. have investigated the degradation behavior of the alloys by an immersion test in a simulated body fluid and shown that the rolled alloy has a lower degradation rate. However, they have shown that further microstructure refinement (average grain size equal to 2.5 µm) by ECAP of the rolled alloy did not permit to further decrease the degradation rate of the alloy, Figure 29. Nevertheless, it is important to note that Wang et al. did not report texture evolution associated with the thermomechanical treatments.

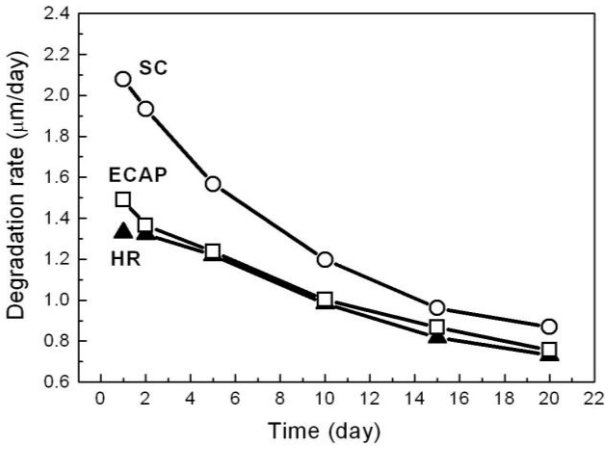

Figure 29: Degradation rate of SC (squeeze cast), HR and ECAP sample in Hanks solution under static conditions [16].

There is little literature concerning the effect on corrosion of other microstructural parameters like texture and dislocation density in Mg alloys. However, basal planes have been reported to have a lower surface energy than the other planes and thus to be electrochemically more stable [38] [39]. Rolling and direct extrusion usually produce materials with a basal texture. Thus, the surfaces with basal texture obtained by these processes should have a beneficial impact on the corrosion resistance. Dislocations are crystallographic defects. Thus, a higher dislocation density locally decreases the electrochemical stability (formation of an anodic area) [40]. Then, this area would encourage galvanic corrosion with the cathodic matrix.

***

Changing the microstructure using thermomechanical processing should be an effective way to affect the corrosion behavior. However, thermomechanical processes impact several parameters at the same time. Therefore, the effect on corrosion of the complete microstructure evolution is difficult to anticipate. Specific investigation on the selected Mg-2wt.%Ca system is then required.

4.2 Characterization methods

4.2.1 Mechanical characterization

The mechanical properties of the thermomechanically processed samples were evaluated using micro-hardness and compression tests. These experiments aimed to compare the different states (not at an in-depth mechanical properties study that would have required more elaborate experiments).

4.2.1.1 Micro-hardness

Vickers hardness measurements were performed using a load of 25 g for a duration of 15 s. Indentations on the rolled samples were made on a surface parallel to the rolling plane and, for extruded samples, in both directions: perpendicular and parallel to the extrusion direction. Indentations were made inside dendrites or in the largest matrix areas, i.e. aiming to avoid the second phase areas. 10 measurements for each tested surface were done, the dispersion (minimum and maximum measured values) were shown by the error bars. For the rolled samples, due to the limited thickness, the micro-hardness measurements were made only on a surface parallel to the rolling plane. Concerning the extruded sample, the micro-hardness measurements were made in both directions: in the extrusion direction (ED) and normal to ED and at more than 1 mm from the specimen periphery. Only the average value is reported in the present work as no significant difference was found between these two directions. Before hardness tests, the samples were polished with an abrasive paper (4000 grit).

4.2.1.2 Compression tests

Compression tests were performed up to fracture at room temperature using an MTS 4M machine equipped with a 20 kN cell load and a strain rate of 2.5×10^{-4} s^{-1}. Cylindrical samples with the dimension of 3 mm in diameter and 5 mm in length were used for these tests. Compression direction was parallel to the ingot axis for the as-cast sample and parallel to the extrusion direction for the extruded and ECAP samples. Electro-erosion was used to prepare the samples when needed (as-cast and ECAP materials). No compression tests could be done on the rolled material due to its small thickness which did not allow making appropriate samples.

4.2.2 Corrosion characterization

Because of the biomedical context, corrosion has been studied in a simulated body fluid. Hanks solution, which is the most common fluid used in corrosion studies of magnesium alloys for degradable implant applications [133], have been chosen for the present work. The composition used in this work is given in Table 8.

Table 8: Composition of the Hanks solution simulated body fluid.

Component	Concentration ($g.L^{-1}$)
NaCl	8.0
KCl	0.4
$MgSO_4.7H_2O$	0.2
$CaCl_2.2H_2O$	0.19
$Na_2H_2PO_4.7H_2O$	0.08
KH_2PO_4	0.06
$NaHCO_3$	0.35
Glucose	1.0
Phenol red	0.02

4.2.2.1 Mass loss test

For the immersion test, samples were polished using the classical techniques, with last step done on a 4000 grit paper using ethanol. Samples were cleaned in an ultrasonic bath with ethanol, measured and weighted before immersion. The samples were immersed in a dedicated jar placed in a thermostatic bath, Figure 30. A ratio of 10 mL per 10 mm^2 sample surface of Hanks solution was used and renewed every 24 H. A thermostatic bath was used to keep immersion temperature at 37 ± 1 °C. After 7 days of immersion the samples were cleaned with distilled water and corrosion products carefully removed using a chromic acid solution [5]: CrO_3 at 100 $g.L^{-1}$. Then the samples were weighted again and the mass loss rate was estimated.

[5] Chromic acid has a negligible corrosion attack on magnesium alloys but removes the corrosion products [200].

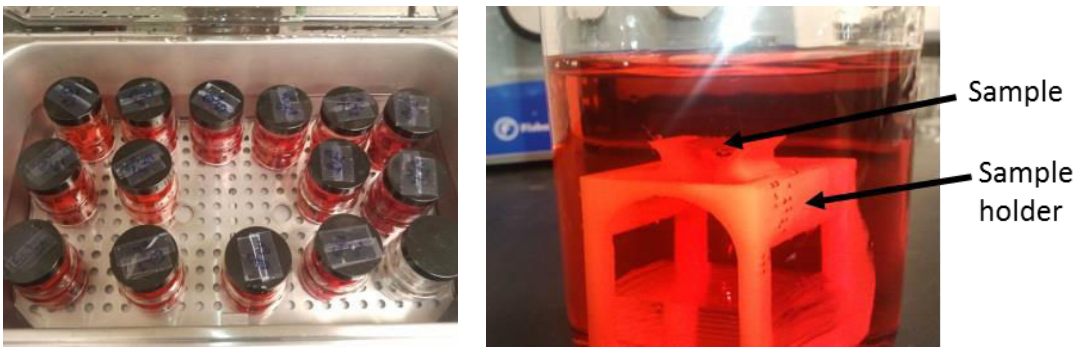

(a) (b)

Figure 30: Overview of the experimental set-up of (a) the thermostatic bath with several jars, (b) a sample on its sample holder in Hanks solution, the red colour indicated a pH=7.4.

4.2.2.2 Electrochemical impedance spectroscopy

Electrochemical impedance spectroscopy (EIS) was done in collaboration with the "Departamento de Engenharia Quimica e Biologica" of the "Instituto Superior Tecnico" in the "Universidade Tecnica de Lisboa" (Portugal). The system used in the present project is shown in Figure 31.

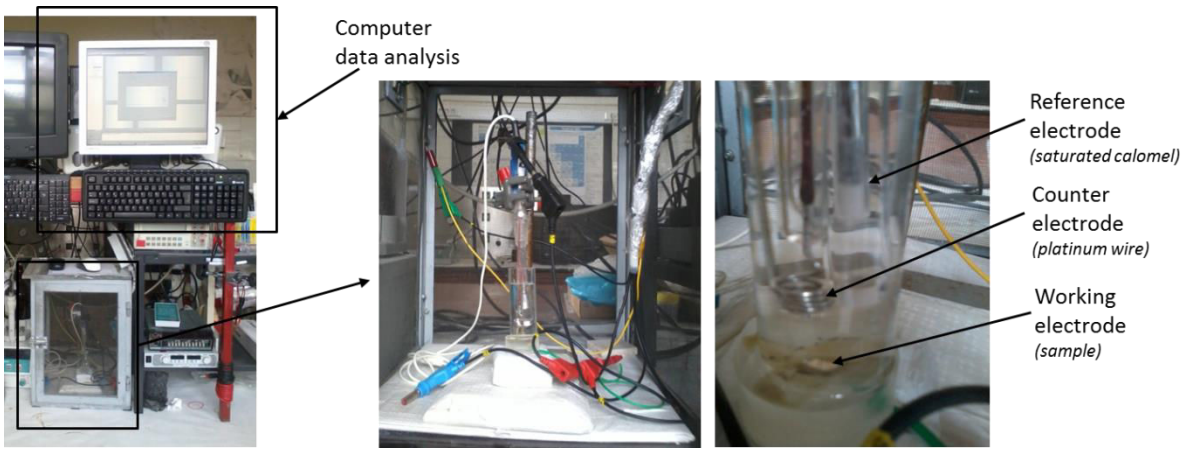

Figure 31: On the left, the electrochemical impedance spectroscopy system; on the right, a zoom on the electrolytic cell formed by a tube on a mounted sample.

Samples were connected to a wire using silver lacquer and cold mounted in an epoxy resin prior to measurements to ensure a good electrical contact. The samples were polished using abrasive papers to 4000 grit (with ethanol) at the last step. A tube was then added on the mounted sample to form the electrolytic cell shown in Figure 31 (right). This cell was filled with 15 mL of a Hanks solution at t = 0 H. A saturated calomel electrode was used as the reference electrode and a platinum wire acted as the counter electrode. Finally, EIS measurements were made after different

periods of immersion: 0 H, 1 H, 3 H, 6 H, 9 H, 24 H, 33 H and 48 H and under room conditions. For each condition, the impedance, Z, and the phase shift, θ, were measured under the open circuit condition with a 10 mV peak to peak signal amplitude at a frequency range from 10 mHz to 100 kHz (which are conditions used in the literature [134]). The impedance can be defined as the following complex quantity:

$$Z = |Z|e^{i\theta} \quad (8)$$

From these spectra, Nyquist plots and Bode plots were derived in order to carry out quantitative analysis. Nyquist plots allow a direct comparison of the corrosion resistance of the materials for the different immersion times. Bode plots represent the phase angle, θ, and the magnitude of the impedance, $|Z|$, as a function of the frequency. The phase shift being sensitive to additional time constant in the electrochemical behavior of the material, Bode plots are convenient to reveal the characteristic time constants [135].

It is also possible to model the electrical behavior of the electrochemical cell by an electrical circuit of passive electrical components. Then, the quantitative analyses using equivalent circuit descriptions were carried out using the EIS Spectrum Analyzer software [136].

4.2.3 Structural characterization

In order to evaluate the impact of the thermomechanical processes on the microstructure, a multiscale characterization study was carried out.

4.2.3.1 Microstructural observations

Optical microscopy

The evolution of the microstructure and more specifically grain size evolution was investigated by metallography using an optical microscope. The samples were etched prior to observations with the following solution: 1 mL HNO_3, 24 mL distilled water and 75 mL ethylene glycol. From the microscopy images, using the software ImageJ [137], the average grain size was determined following the lineal intercept procedure [138]. For the rolled sample, the rolling surface was investigated and for the extruded samples both directions: ED and normal to ED were investigated.

The investigation of corroded sample was also done using an optical microscope. For these observations, after removal of corroded products with a chromic solution, samples were mounted in epoxy resin. Polishing with abrasive papers and ethanol up to 4000 grit were done on the top surface to allow for observation of the corrosion on the side of the cylindrical samples.

Scanning electron microscopy

The second phase morphology was studied by scanning electron microscopy (SEM) using a LEO S440 and a ZEISS Ultra 55, both handled by the Consortium des Moyens Technologiques Communs (CMTC) from Grenoble Institute of Technology. The ZEISS Ultra 55, which is equipped with a field emission gun and an in lens detector, allowed high resolution images when the scale of the second phase microstructure was too fine for the LEO S440. Samples were prepared by polishing using abrasive papers for the first steps and diamond paste up to $^1/_4$ µm for the last steps. Ethanol was used as a solution for the diamond paste polishing steps.

Transmission electron microscopy

High magnification observations of the microstructure were done using transmission electron microscope (TEM) on a JEOL 3010 operating at 300 kV (SIMaP laboratory). This microscope was principally used for detailed investigations of the eutectic/second phase morphology after thermomechanical processing. Conventional TEM was carried out using the bright field and dark field modes that are appropriate for imaging grains, microstructural defects and second phases.

The samples for TEM were prepared by mechanical polishing using a 4000 grit paper down to a thickness between 50 µm to 70 µm. Thinning down by ion beam milling was carried out using a GATAN 691 precision ion polishing system (PIPS) with argon ions under a tension of 4 keV and incidence angle 10 °. When a hole appeared at the centre of the sample, a final thinning down was done at lower angle (6 °) and a lower voltage, i.e. 3 keV, for 1 H.

4.2.3.2 Texture analysis

Texture analysis was carried out by X-Ray diffraction. For the work reported in this thesis, a Siemens D5000 four circles X-ray diffractometer of CMTC (Grenoble INP) has been used. A cupper anode with a wavelength of 0.154nm for its Kα line has been

used as a source for the x-ray beam. Only the magnesium matrix has been investigated for texture analysis, the percentage of second phase was not high enough to produce a sufficient diffracted signal for analysis. The following planes have been investigated: (0001), $(10\bar{1}1)$ and $(11\bar{2}0)$; the 2Θ angles being respectively set to the following values: 34.399 °, 36.620 ° and 57.375 °. A variation of the angle ϕ from 0 to 355 ° with a step of 5 ° and a variation of the angle χ from 0 to 85 ° permit the exploration of the diffractions angles. The samples were polished before measurements with abrasive paper up to 4000 grit with the last step using ethanol.

4.3 Thermomechanical processing

The different thermomechanical processes considered in the present study are rolling, conventional extrusion and a non-conventional extrusion process called equal channel angular pressing (ECAP).

4.3.1 Rolling

The rolling machine used in this study was a conventional rolling device composed of two parallel cylinders which rotated at the same velocity. The thickness of the material was reduced in the normal direction (ND), which caused an increase in the length of the material in the rolling direction (RD). The increase of width in the transverse direction (TD) was considered as insignificant. In the present study, the rolls were at ambient temperature and had a velocity of 10 $m.min^{-1}$.

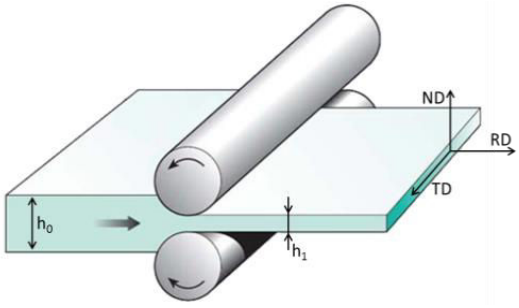

Figure 32: Schematic representation of a conventional rolling system with the associated directions (adapted from [139]).

Conventional rolling was carried out on an 8.4 mm thick plate. For the first trial, two passes at 40 % reduction with pre-heating at 300 °C was performed. However, at the

first pass, which consisted of a reduction from 8.4 mm to 5 mm, the material broke in several parts, making a second rolling impossible. Thus, fir the subsequent trial, a 2 min heat treatment at 400 °C and a lower percentage of reduction (equivalent to 0.5 mm of thickness reduction at each pass) were applied for each pass. Table 9 summarizes the experimental reduction data. The total equivalent strain, i.e. $\overline{\varepsilon_{roll}} = \ln\left(\frac{h_0}{h_1}\right)$, was equal to 1.39. The sample was air cooled after the final pass.

Table 9: Measured thickness evolution between each pass during rolling at 400 °C.

h_0 (mm)	8.4	8.0	7.5	7.0	6.7	6.3	5.6	5.1	4.5	4.1	3.6	3.0	2.5
h_1 (mm)	8.0	7.5	7.0	6.7	6.3	5.6	5.1	4.5	4.1	3.6	3.0	2.5	2.1
Reduction (%)	4.8	6.3	6.7	4.3	6.0	11.1	8.9	11.8	8.9	12.2	16.7	16.7	16.0

During rolling steps, the material showed some edge cracking and also few visible cracks in the inner part of the rolled sample. These cracks in the rolled material could result from the lack of ductility due to the strong basal texture obtained by rolling. Also the high density of twins, that is known to reduce the dislocation motion in the basal direction [25], could account for these cracks. The inner parts of the material which were not affected by cracks were kept for further microstructural, mechanical and corrosion investigations.

4.3.2 Direct extrusion

The conventional extrusion was conducted using a direct extrusion machine from SIMaP laboratory (Figure 33(a)). The set-up was based on a compression and traction test machine Adamel DY26 equipped with a load cell of 100 kN. A heating system adapted on the extrusion device allowed working at high temperatures (up to 425 °C). The maximum force delivered by the machine was 50 kN. The machine was equipped with different dies. To reduce the friction between the die and the material, a high temperature resistant lubricant was used. Also during extrusion, the set-up allowed for recording stress-strain curves that provided a full monitoring of the process.

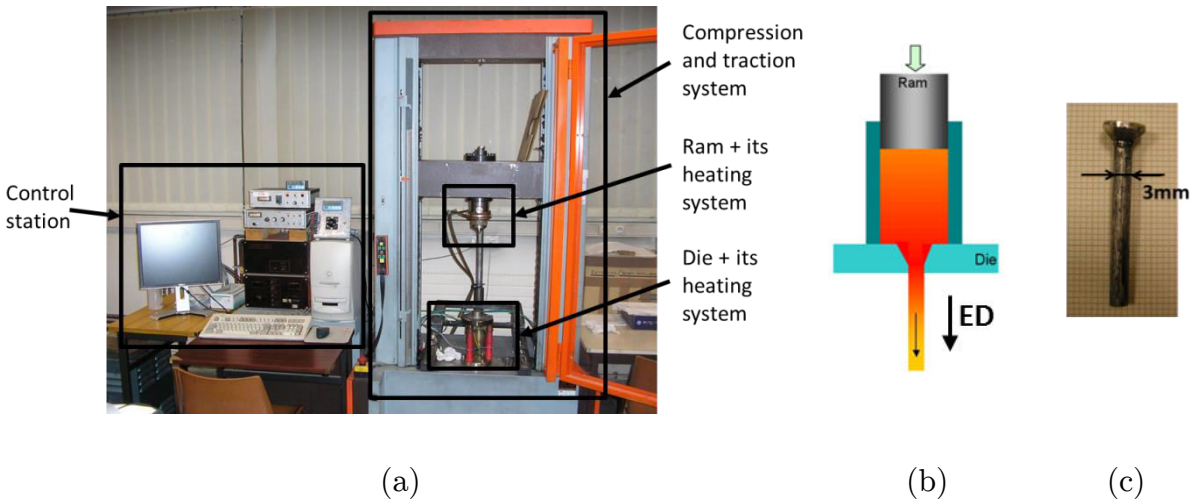

Figure 33: (a) Experimental set-up of the extrusion system, (b) a schematic representation of the process with the associated extrusion direction (ED) (Public domain) and (c) an extruded sample.

The die used for studying the mechanical and corrosion behavior in the present work had a cylindrical shape with an entrance diameter of 7 mm and an exit diameter of 3 mm. This system permitted an extrusion ratio R_e = 5.4, corresponding to the equivalent strain, i.e. $\overline{\varepsilon_{extru}} = \ln(R_e)$, of 1.7. The chosen extrusion parameters for the present work are displayed in Table 10. This range of temperature was selected to permit different microstructural evolutions. In these conditions, extrusions were correctly achieved; no crack was visible on the surface of the samples.

Table 10: Chosen parameters for extrusion of Mg-2wt.%Ca.

Parameter	Value
Temperature	200 °C, 250 °C, 300 °C, 350 °C and 400 °C
Ram speed	0.9 $mm.min^{-1}$

In order to carry out the surface functionalization study in the second part of the project, a different die was used that allows for rectangular extruded shape with the following dimensions: 5 mm thick and 1.5 mm width (extrusion ratio R_e = 5.1). The extruded plates were obtained in selected conditions from the previous panel of the extruded cylinders (temperature, ram speed) based on the obtained mechanical and corrosion properties. The plate shape was more convenient for the laser-assisted patterning while the cylindrical shape was more adapted for compression test samples.

4.3.3 Equal Channel Angular Pressing

Finally, a non-conventional thermomechanical treatment, the so called ECAP process, was used in this study. In our case, the system was designed by Dupuy L., [140], and set-up on the Adamel DY26 machine used for extrusion. The entrance dimensions of the die were 10 * 10 mm and the exit ones were slightly smaller: 9.9 * 9.9 mm. This smaller exit size was used to avoid any problem due to thermal dilatation that would prevent the billet to be directly inserted for another pass.

According to the conditions used in this project ($\varphi = 90°$ and $\Psi = 0°$), the equivalent strain applied to the material at each pass was equal to 1.15 (see Equation (7) Section 3.1.1). The cast alloy used in the present study had a large grain size, thus, to produce high microstructural modifications, a total number of 8 passes was performed (see literature review Section 3.1.1). Then the total applied equivalent strain was equal to 9.2.

As shown in Figure 34, this home-made ECAP system was fitted with a hydraulic jack at the front permitting to eject the billet and immediately water quench it before the subsequent pass. In the present case, the ram velocity was set to 5 $mm.min^{-1}$, which allowed completing a pass for a 50 mm billet in about 10 min. A heating system made of four heating resistors permitted to obtain a temperature from room temperature to 350 °C. The temperature was controlled near the inner die by two thermocouples and regulated by a PID controller. To limit the friction between the billet and the inner die, molybdenum disulfide was used as the lubricant for the inner die and for the surfaces of the billet between each pass.

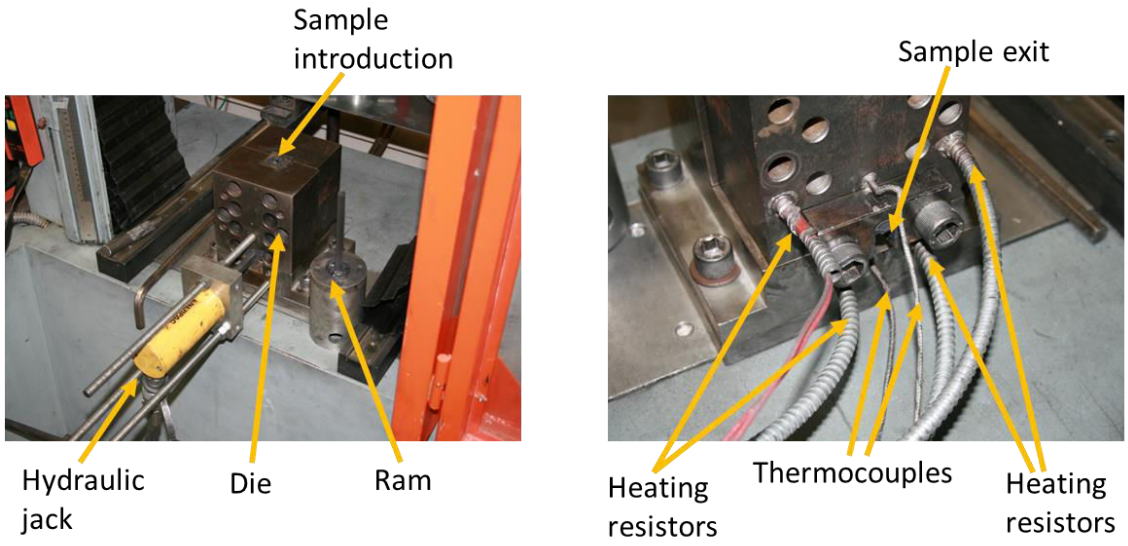

Figure 34: ECAP system: (a) front view, (b) rear view.

As the temperature plays an important role in grain growth, ideally to obtain a fine grain microstructure the lowest temperature should be used. The determination of the lowest possible temperature was done by trial and error on a low-grade Mg-2wt.%Ca alloy. After several attempts, the optimal temperature was 280 ± 5 °C. Under 280 °C, samples were broken in several pieces due to shearing, Figure 35.

Figure 35: Broken sample by ECAP at low temperature.

The following protocol was followed for ECAP processing. Billets were cut from the longitudinal orientation of the cast material. Their dimensions were adjusted by polishing using an abrasive paper (up to 4000 grit) to obtain a section between 9.90 * 9.90 mm^2 to 9.95 * 9.95 mm^2. The length of the billet was 45 ± 1 mm. The ECAP system was heated 1 H before the experiment to obtain a stable temperature inside the system (280 ± 5 °C). Then the ECAP procedure was started following an adapted route B_A, as specified in [140]. The billet was alternatively rotated by + 90° and – 90° but also turned top to bottom as shown in Figure 36. This specific introduction of the billet allowed avoiding the stretching of the sample occurring

after several passes. The ECAE3D software developed by Dupuy [140] was used to determine the working volume of the extruded sample, i.e. the part of the billet subject to the total deformation.

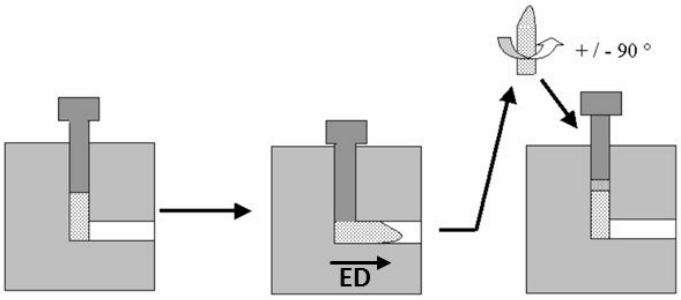

Figure 36: Specific introduction of the billet for each pass [141] and description of the extrusion direction (ED).

All the thermomechanical processes described above were used to tailor the bulk microstructure of the Mg-2wt.%Ca alloy in order to improve their mechanical and corrosion behavior.

4.4 Impact of thermomechanical processing on properties

4.4.1 Mechanical behavior

The results of Vickers hardness measurements of the as-cast and processed samples are presented in Figure 37.

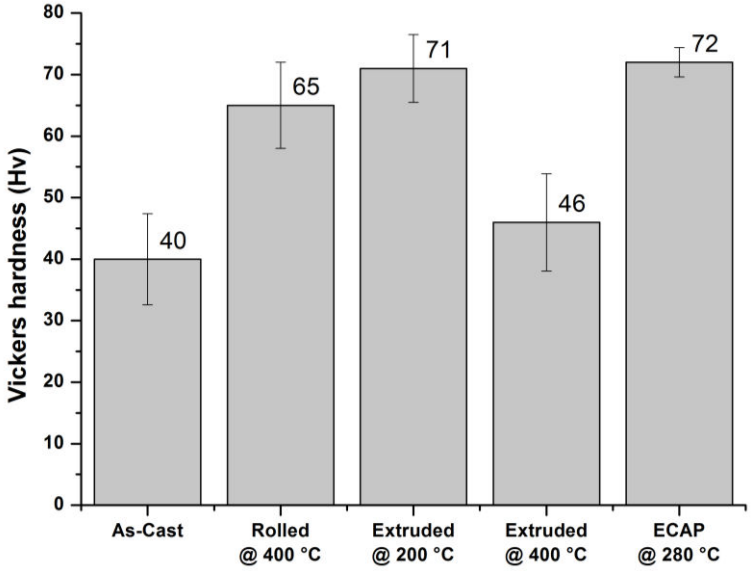

Figure 37: Evolution of the Vickers hardness by thermomechanical processing.

Depending on processing, the hardness values are ranging from 40 to 72 Hv. The low hardness of the as-cast material is in agreement with the value measured for a Mg-2wt.%Ca alloy by Harandi S. E. (42 Hv) [142]. The increase of the hardness after thermomechanical treatment clearly illustrates the possibility to strengthen the material by these processing. The sample extruded at 400 °C shows a limited increase of hardness. The highest hardness is obtained for extrusion performed at 200 °C and for the ECAP processes an increase by about 175 % of the initial hardness is obtained.

Regarding the hardness increase observed after thermomechanical processing, it is interesting to compare them to Mg-Ca alloys with different calcium contents. Bakhsheshi Rad et al. [130] have reported the evolution of hardness with calcium content in Mg-Ca alloys for the solute content up to 10 wt.% Ca. The highest hardness (78.8 Hv) is obtained for an as-cast Mg-10wt.%Ca alloy. In comparison with alloying effects, thermomechanical processes appear very efficient increasing the strength. This is particularly of noticeable advantage for low solute content in alloys, e.g. 2 wt.% Ca, which are of interest for a better corrosion behavior.

In addition to hardness tests, compression tests have been carried out to get complementary information. The stress-strain plots obtained from the compression tests are shown in Figure 38 (a).

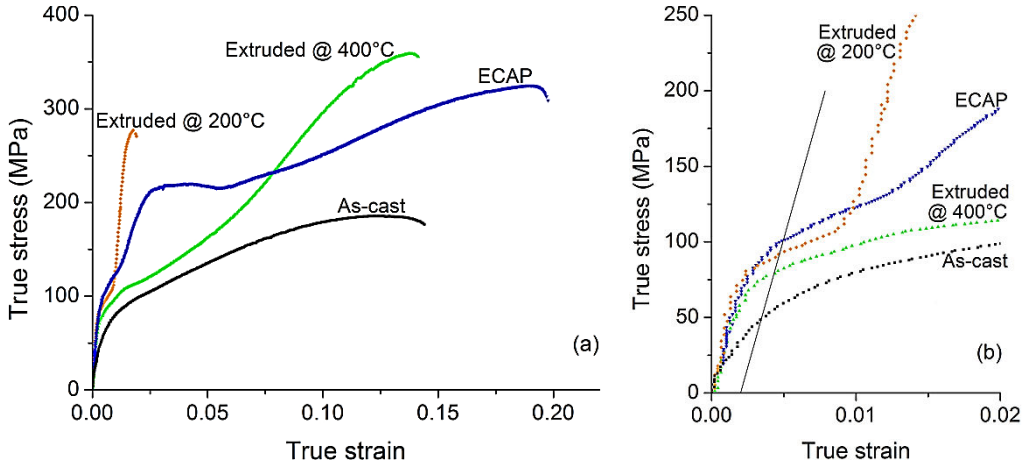

(a) (b)

Figure 38: (a) Strain-stress curves of as-cast and thermomechanically processed materials at ambient temperatures with a strain of 2.5 10-4 s^{-1} and (b) zoom on the elastic part and determination of the 0.2 % proof stress. (Note: no compression test has been done on the rolled material due to the small size of the samples available).

The stress-strain curves, shown in Figure 38, allow comparing the strength of the tested materials as well as their ductility in compression. Table 11 displays the characteristic values given by the compression tests: ultimate strength, maximum compression strain and 0.2 % proof stress.

Table 11: Evolution of the ultimate compressive strength and maximum compression strain as a function of the thermomechanical processing.

	Ultimate strength (MPa)	Maximum compression strain	0.2 % proof stress (MPa)
As-cast	186	0.14	49
Extruded at 200 °C	277	0.02	93
Extruded at 400 °C	359	0.14	80
ECAP at 280 °C	325	0.20	102

The cast material presents poor mechanical properties. One can also note that at low strains, the compression curves of the sample extruded at 200 °C and the sample processed by ECAP display an inflection around 100 MPa corresponding to the end of the elastic part. This inflection is a typical feature of the compressive stress-strain curves of magnesium alloys, and attributed to the activation of a compression twinning mechanism [143]. Concerning the specimen extruded at 400 °C, at low stress (75 MPa), the sample begins to deform plastically.

The plastic deformation curves of the different samples present different trends. Indeed, the sample extruded at 200 °C shows a typical behavior of a brittle material with a high increase of stress with low deformability. The cast sample presents a strain-hardening behavior before fracture. The sample extruded at 400 °C presents a S shape curve above 125 MPa formed by strain hardening before fracture. The sample processed by ECAP begins to show a high increase of stress with low deformation. When the sample reaches approximately 215 MPa there is a plateau at constant stress with deformation from 0.03 to 0.06. Finally, in the final deformation step, strain-hardening occurs before failure.

According to the ultimate compression strength, ECAP and 400 °C extruded materials stand as the most strengthened states. In addition, both materials have significant deformability. However, the 0.2 % proof stress of the ECAP material is actually higher than the one of the material extruded at 400 °C. It is worth noting that the sample extruded at 200 °C that shows a high hardness has a poor ductility with only 2 % strain before failure.

In spite of the low calcium content of the current alloy, the mechanical strength level obtained after thermomechanical processing are in the highest range of the materials considered for degradable application as reported in the review by Kirkland et al. [144]. For comparison, it is reported that cast Mg-Ca and Mg-Zn alloys, with a very high solute content (up to Mg-10wt.%Zn and Mg-16.2wt.%Ca), have an ultimate compressive strength varying from 150 MPa to 350 MPa [144]. From the comparative data discussed above, the ECAP treatment definitely appears as the most efficient to improve the mechanical behavior of the Mg-2wt.%Ca alloy.

4.4.2 Corrosion behavior

In order to compare the corrosion behavior of the thermomechanically processed samples with the as-cast material, immersion tests with mass loss measurements have been carried out. The mass loss rates measured after 7 days of immersion in Hanks solution at 37 °C are displayed in Figure 39. These degradation rates cover a large range: from 3.6 $mg.cm^{-2}.day^{-1}$ for the as-cast material to 0.1 $mg.cm^{-2}.day^{-1}$ for the sample processed by ECAP. This evolution of the mass loss rate provides the first evidence for the high impact of thermomechanical process on the corrosion behavior.

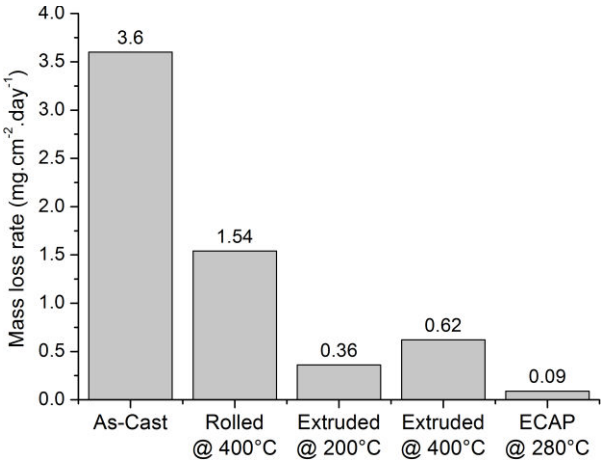

Figure 39: Evolution of the mass loss rate for different thermomechanical processing routes after 7 days of immersion in Hanks solution.

Compared to the as-cast sample, after rolling, mass loss rate is reduced by a factor 2. By extrusion at 200 °C, the mass loss rate is reduced by a factor of 9 of the initial value. The maximum reduction is obtained by the sample processed by ECAP, which is corresponding to a reduction by a factor 36. It is worth noting that extrusion at 400 °C is less efficient to reduce the mass loss rate than extrusion at 200 °C. This suggests that microstructural parameters impacted by the processing temperature have an impact on the corrosion behavior.

Mass loss tests give the average mass loss rates on a selected period of time but do not allow for a series of continued measurements as possible with the electrochemical impedance spectroscopy (EIS). In addition, analysing the Nyquist plots derived from EIS in terms of equivalent electrical circuits, it is possible to compare quantitatively the corrosion resistance of the various samples after different immersion times. Nyquist plots obtained from EIS tests are plotted in Figure 40. These plots show the evolution of the corrosion behavior for the investigated processing conditions (as-cast and thermomechanically processed) after different immersion times in Hanks solution (0 H, 1 H, 6 H and 9 H). Note that for EIS measurements, since a selection of the most relevant samples had to be made, the sample extruded at 200 °C has been discarded because of limited interest due to its too low deformability (Table 11).

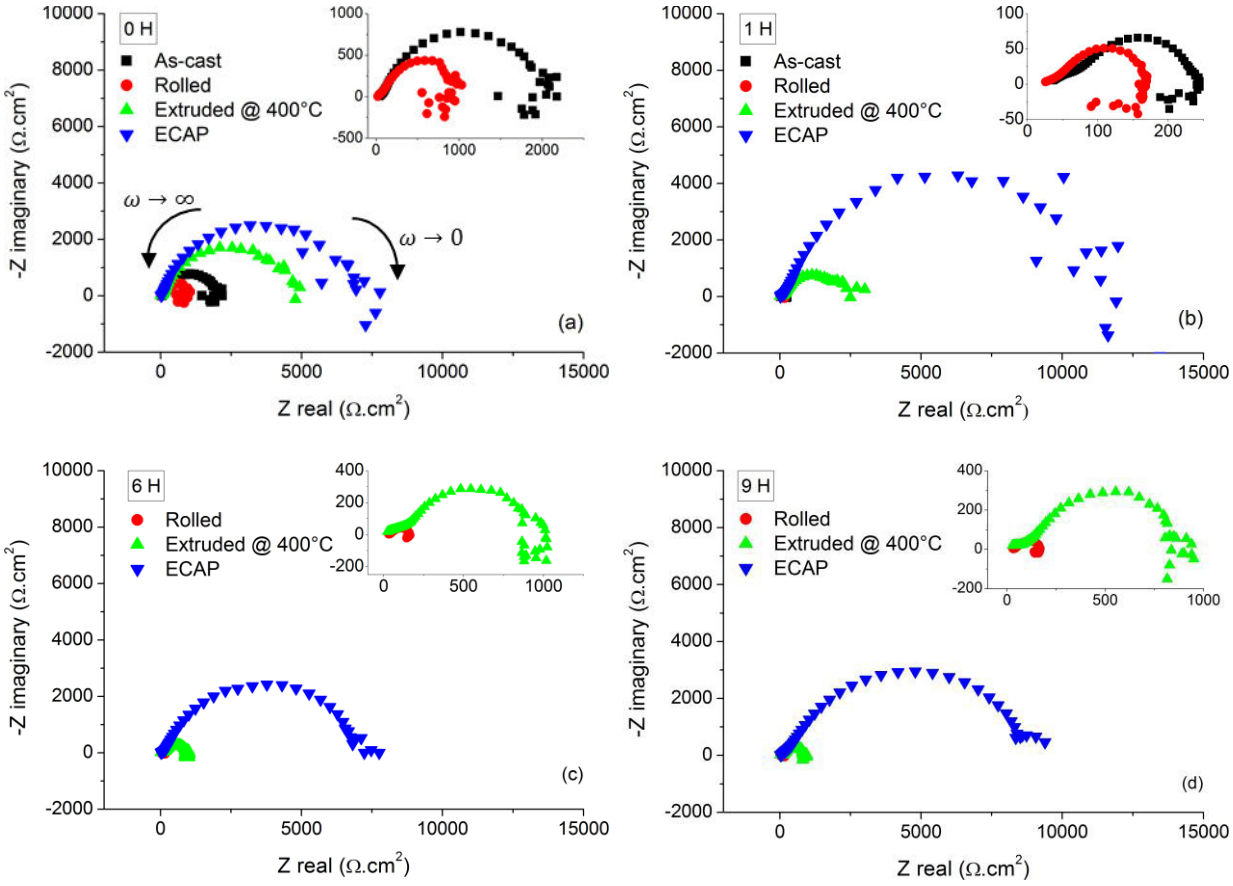

Figure 40: Nyquist plots of the as-cast and thermomechanically processed samples in Hanks solution at (a) initial immersion, (b) immersed for 1 H, (c) immersed for 6 H and (d) immersed for 9 H (Note: The as-cast sample does not appear in the 6 H and 9 H plots, due to its extensive corrosion.). For clarity, the low Z part of the Nyquist plots is shown in the inserts on the top right of each figure.

Before a quantitative analysis, some qualitative observations can be made from the Nyquist plots obtained at different immersion times. First, all the states are roughly characterized by an identical trend, but the impedance values are significantly affected by the thermomechanical processing. In particular, the sample processed by ECAP displays the semi-circle with the largest diameter compared to other states. This feature is more pronounced for longer immersion times. One can note the presence of an inductive loop at low frequencies on some Nyquist plots, which is an indicator of corrosion activity [145]. The low frequency dispersion can induce difficulty in the numerical simulation of the experimental measurements using equivalent circuits [133]. Thus, in this work a simplified approach that consisted of the simulation of the EIS data only at medium/high frequencies was adopted.

In a resistance-capacitor equivalent circuit description, the semi-circle diameter of a Nyquist plot corresponds to an electrical resistance assigned to a specific

phenomenon, such as the existence of a surface layer or to the charge transfer processes, which reflects the corrosion resistance. Therefore, qualitatively, the increasing diameter of Nyquist plots (Figure 40), points out the increase in corrosion resistance due to thermomechanical processing. The highest corrosion resistance results from the ECAP processing. The Bode plots (Figure 41) were used to identify the characteristic time constants and therefore the number of electrochemical phenomena that should be considered to model the Nyquist plots.

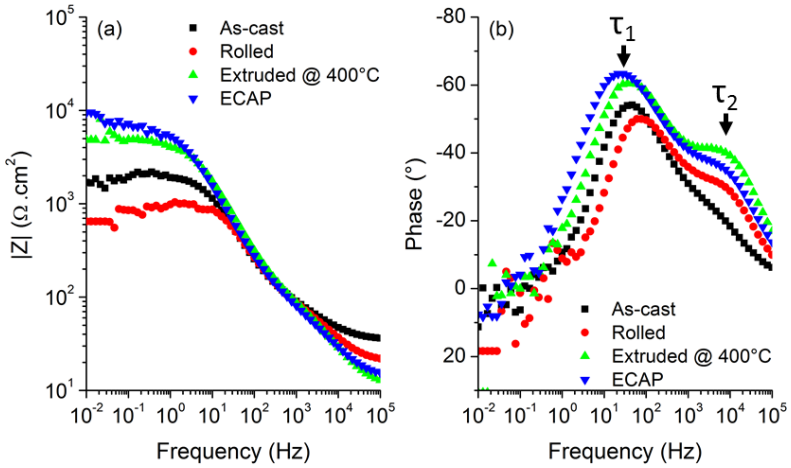

Figure 41: Bode plots of the as-cast and the thermomechanically processed samples at the initial state.

The Bode phase plots in Figure 41 can be described in three frequency domains. The medium and high frequency domains are characterized by the presence of two time constants: τ_1 and τ_2. The time frequency constant at low frequency reflects the active corrosion process and is usually explained as the result of surface relaxation processes of adsorbed species on the electrode surface, and in particular, adsorbed Mg^{+} reacting to Mg^{2+} or $MgOH^{+}$ [146], [147]. This process is associated with an inductive behavior of the system with a slight decrease of the impedance modulus and a positive phase shift. Such inductive behavior does not seem to occur in the sample processed by ECAP at the explored frequencies. For magnesium and magnesium alloys, Wen et al. [148] have reported that the mechanism involved at medium and high frequencies can be respectively related to the build-up of a surface layer due to the accumulation of protective corrosion products and to the charge transfer processes. The corrosion process involves strong alkalization of the interface and thus the growth of a stable and insoluble layer of corrosion products. In spite of its stability, the corrosion products layer is not completely protective and there are

defects, allowing electrolyte uptake and the charge transfer processes to occur. In this situation the impedance response is governed by two constant phase elements (CPE) in parallel: one accounting for the film resistance and capacitance and another one accounting for the charge transfer and double layer response [149]. Concerning the medium frequencies response, the maximum phase angles for the samples extruded at 400 °C and processed by ECAP are higher than the one of as-cast. The range of frequencies of this capacitive behavior is also wider toward lower values. This shows a more marked capacitive response of the samples which may be related to more stable and protective oxide layers.

Both time constants at medium and high frequencies are modelled by resistance-capacitor parallel circuit, in agreement with earlier works [18], [148], [150]. In these circuits, constant phase elements (CPE) are used to account for the imperfect capacitance of the phenomena. The equivalent circuit is displayed in Figure 42 with R_s corresponding to the resistance of the electrolytic solution and the two R-C circuits (a resistance with a CPE in parallel). The resistance R_1 refers to the oxide and charge transfer resistances of the sample while the CPE_1 is the constant phase element that describes the imperfect capacitor resulting from the interfacial phenomena at the metal electrolyte interface. The medium frequency resistance can be assigned to the resistance to mass transport through the film formed: R_2, and its CPE_2.

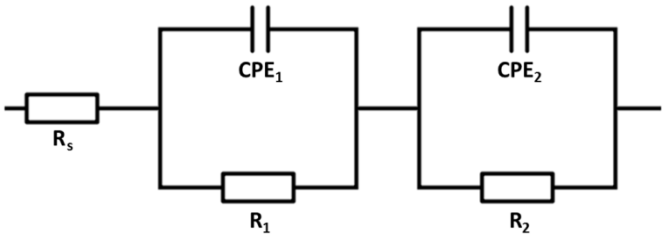

Figure 42: Equivalent circuit of the as-cast and thermomechanically processed samples immersed in Hanks solution where R stands for a resistance component and CPE stands for a constant phase element.

A quantitative analysis based on the equivalent circuits described above was carried out using the EIS Spectrum Analyzer software [136]. From this analysis a global resistance $R_{tot} = R_1 + R_2$ which describes the evolution of the global corrosion resistance of the samples can be derived. Thus, for the investigated samples, a global

resistance in function of the immersion time was obtained. These results are gathered in Figure 43 showing the evolution of the total resistance with immersion time for as-cast and thermomechanically processed samples.

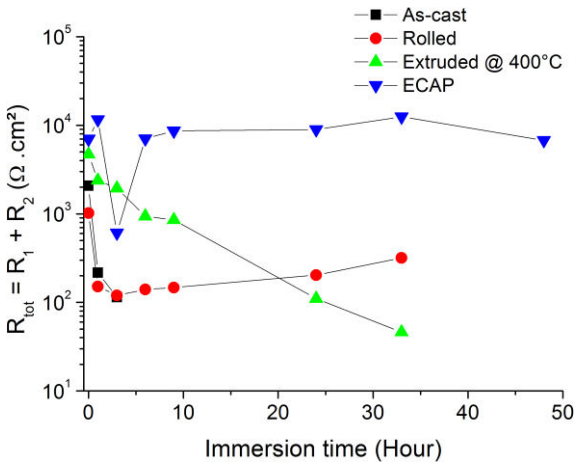

Figure 43: Evolution of the total resistance, Rtot, with immersion time in Hanks solution of the as-cast and thermomechanically processed materials.

According to Figure 43, except for the sample processed by ECAP, the resistance rapidly decreases with the immersion time, with a less pronounced impact for the sample extruded at 400 °C. After 3 H of immersion, as-cast sample revealed intense corrosion activity with visible release of gas bubbles and the EIS measurement was stopped. In parallel, the corrosion resistance of the rolled sample begins to slowly increase which might be due to the accumulation of the insoluble corrosion products like carbonates and phosphates. The two samples: extruded at 400 °C and processed by ECAP, exhibit higher initial corrosion resistance as evidenced in the Nyquist and Bode plots. The corrosion resistance of the sample extruded at 400 °C decreases with immersion time but less rapidly than that of the as-cast and rolled samples. After a 24 H of immersion, rolled and extruded samples display similar corrosion resistance.

Concerning the sample processed by ECAP, except for an anomalous point at 3 H, the corrosion resistance stays remarkably high and almost constant for immersion time up to 48 H. The low frequency resistance at 3 H immersion probably only results from a local breaking of the corrosion products layer due to its instability and/or to the manipulation during measurements. The quantitative analysis of the EIS plots strongly supports the increased corrosion resistance of the sample processed by ECAP for a long immersion time in Hanks solution, as confirmed by the

qualitative analysis. This is in agreement with the mass loss rate reported in Figure 39.

For further understanding of the evolution of both the mechanical properties and corrosion behavior after thermomechanical processing, observations of the microstructure evolution have been done. In the following part, these observations will be presented, and the relation between microstructures and properties will be also discussed.

4.5 Multiscale characterization of the microstructure

4.5.1 Grain microstructure evolution

A first series of observations has been made with classical metallography: light microscopy and etching to reveal the grain boundaries. Figure 44 displays the different micrographs obtained for the as-cast and thermomechanically processed samples.

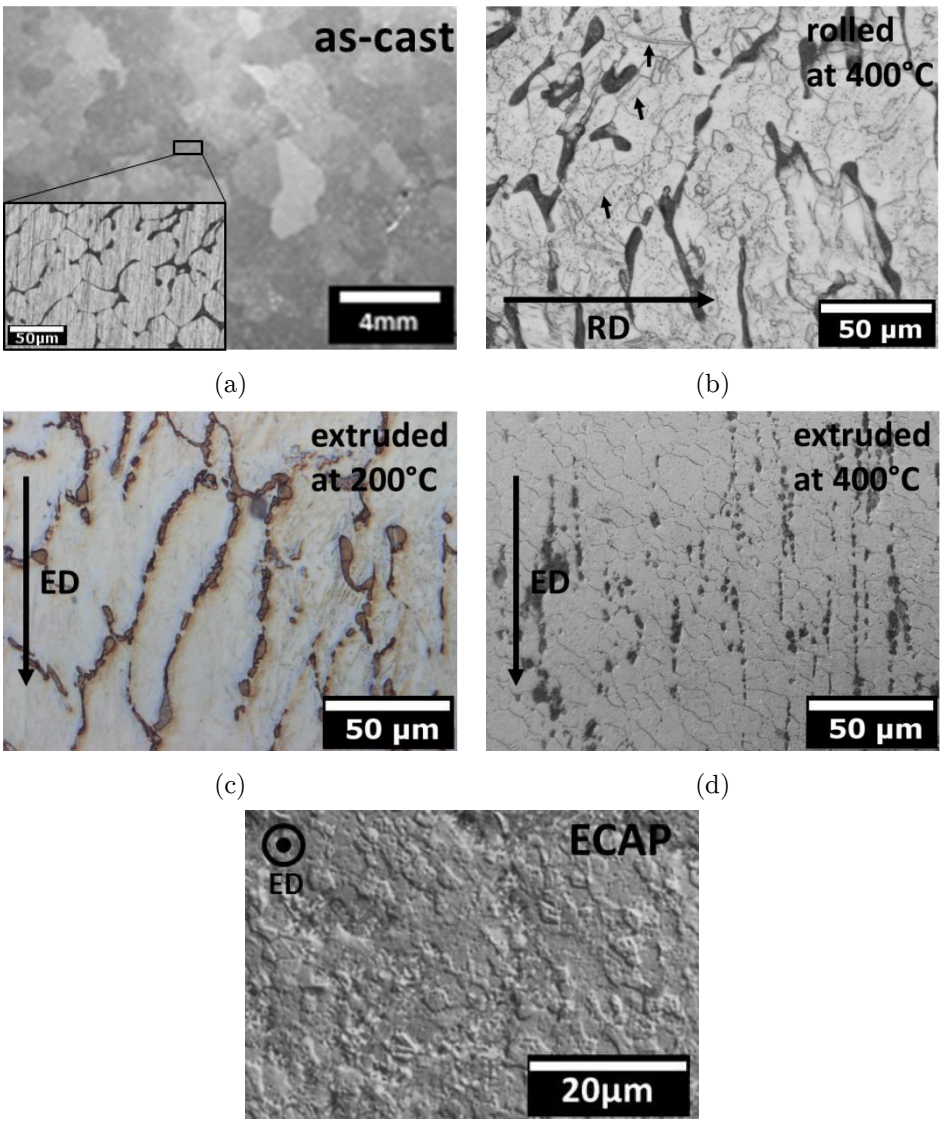

Figure 44: Optical micrographs of differently processed samples after etching: (a) as-cast, (b) rolled at 400 °C, (c) extruded at 200 °C, (d) extruded at 400 °C and (e) processed by ECAP. Note: For a better description of the as-cast sample, fig. (a), a SEM image is given in the insert.

The as-cast sample consists of large grains (Figure 44 (a)), containing magnesium dendrites separated by a thin eutectic mixture (SEM insert Figure 44 (a)). The sample rolled at 400 °C, Figure 44 (b) shows an inhomogeneous microstructure with an average grain size of 25 µm. The presence of twins can also be noticed (marked by arrows in Figure 44 (b)). During the process for rolling, the sample was hold at 400 °C between each pass. This short annealing may have been sufficient to allow dislocation motion and therefore the driving force for the recrystallization process.

After extrusion at 200 °C, Figure 44 (c), no small grains were observed probably because at such a low temperature recrystallization has not occurred. This is

corroborated by a complementary investigation of the extrusion processing which was done with increasing temperatures from 200 °C by 50 °C steps. As shown in Figure 45, at 300 °C, recrystallization preferentially located near the second phase particles was observed. For extrusions at temperatures below 300 °C (250 °C and 200 °C) no recrystallization was observed. Complete recrystallization has occurred in the entire sample for extrusion at 400 °C. The Mg-2wt.%Ca sample extruded at 400 °C has exhibited a homogeneous grain microstructure in both directions (perpendicular and parallel to ED) (≈ 8 µm), Figure 44 (d).

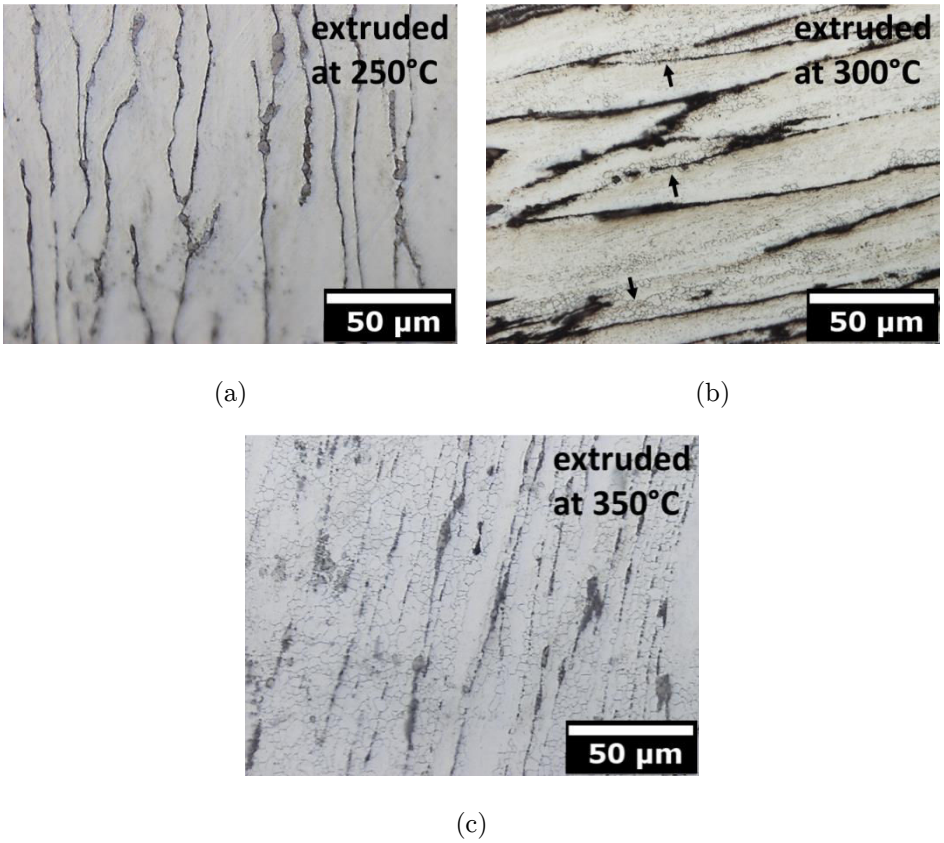

Figure 45: Evolution of the microstructure with the extrusion temperature: (a) 250 °C, (b) 300 °C and (c) 350 °C.

For the sample processed by ECAP (Figure 44 (e)), a fine microstructure was observed. No noticeable difference was observed between ED and perpendicularly to ED. The average measured grain size is 2 µm which represents a significant refinement in comparison with the other processed states.

4.5.2 Second phase evolution

To complete the grain microstructure evolution study, as the starting material is a two phases material, SEM observations has been performed to evaluate more specifically the evolution of the second phase areas by thermomechanical processing, Figure 46. It is worth mentioning that z-contrast SEM imaging does not differentiate between the Mg-Mg_2Ca eutectic mixture and Mg_2Ca particles. As the first step, SEM allows to localize the second phase rich areas, TEM observations will be necessary in the future for more detailed studies. In Figure 46 (a), a TEM image is given in the insert to show the detailed microstructure of the interdendritic area: alternate lamellae of Mg and Mg_2Ca Laves phase with a halo of Mg_2Ca Laves phase at the dendrite/eutectic mixture interface.

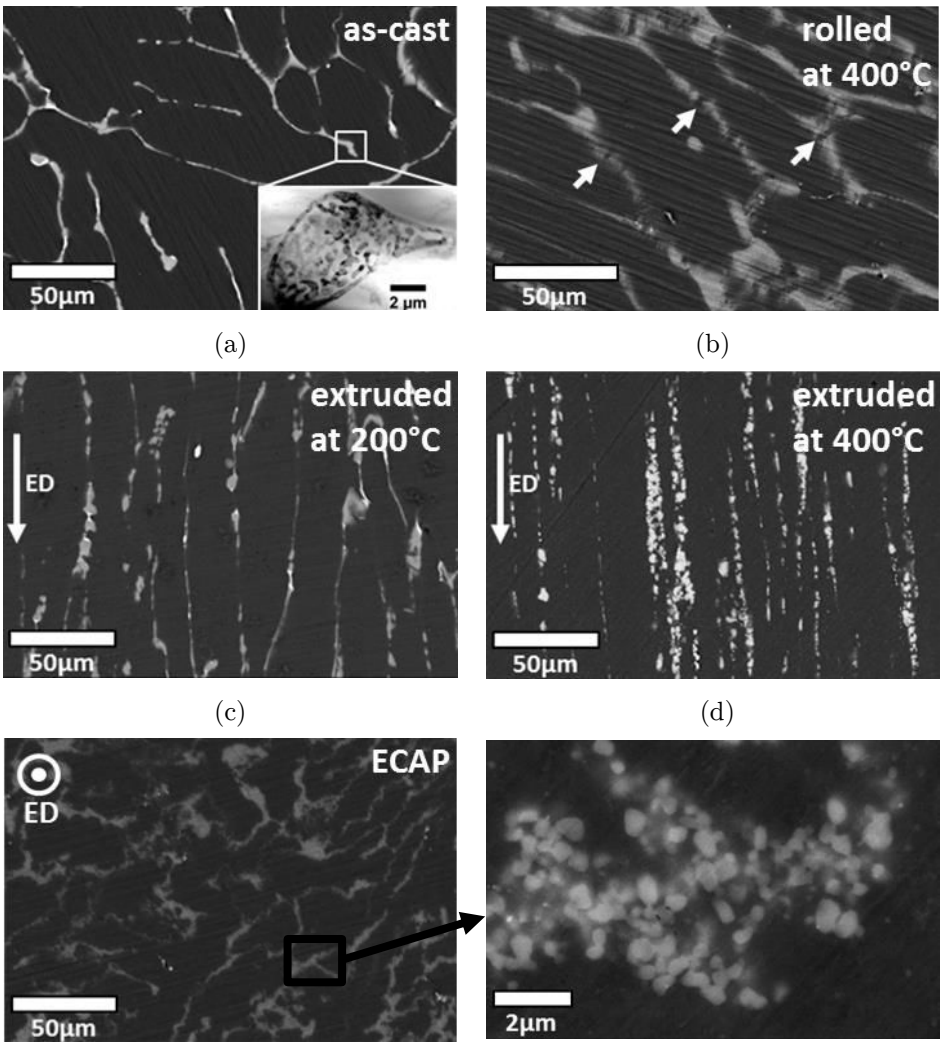

Figure 46: SEM observations of (a) as-cast sample and after different thermomechanical processing: (b) rolling at 400 °C, (c) extrusion at 200 °C, (d) extrusion at 400 °C and (e) processed by ECAP. Note: For a better description of the as-cast sample, fig. (a), a TEM image is given in the insert.

The cast alloy microstructure shows large dendrites separated by the Mg-Mg_2Ca eutectic mixture. The eutectic mixture forms a 3D skeleton. Since Mg_2Ca phase, as all Laves phases, is very brittle [151], a significant evolution of the second phase microstructure with thermomechanical processing can be expected.

After rolling, the eutectic mixture skeleton shows many disconnections as pointed by the arrows in Figure 46 (b). Also after extrusion at 200 °C, Figure 46 (c) indicates important changes in the eutectic mixture skeleton. Indeed, after the 200 °C extrusion the skeleton arms appear very elongated and disconnected in many points. As illustrated by Figure 46 (d), after extrusion at 400 °C, more pronounced changes

in the second phase microstructure have occurred. For additional information, Figure 47 is displayed to show different views of the sample at a higher magnification.

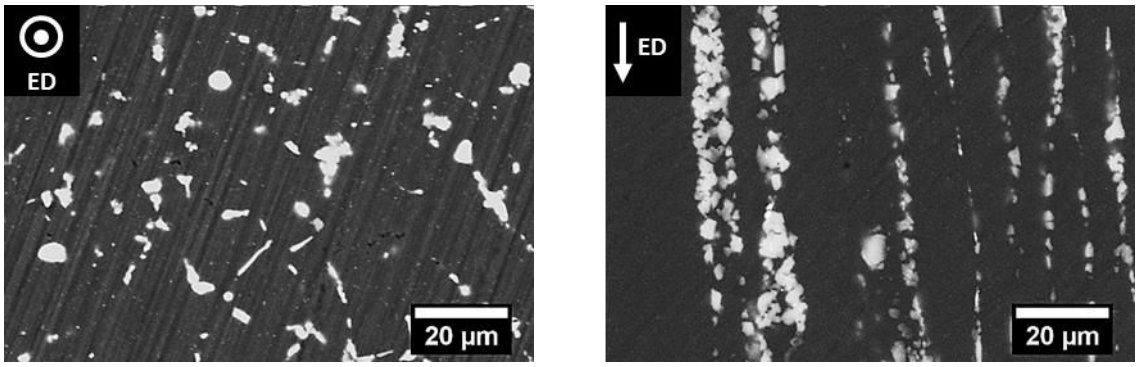

(a) (b)

Figure 47: SEM observations of a sample extruded at 400 °C: (a) perpendicularly to the extrusion direction and (b) parallel to the extrusion direction.

On the view perpendicular to the extrusion direction, the fragments of the eutectic mixture seem uniformly dispersed. On the view parallel to the extrusion direction, the skeleton of eutectic mixture has been fragmented in small pieces and dispersed following the extrusion direction. The size distribution of the fragments is rather heterogeneous. Indeed, if with a closer look at the microstructure using TEM, it is possible to note the presence of very fine particles of Mg_2Ca, Figure 48.

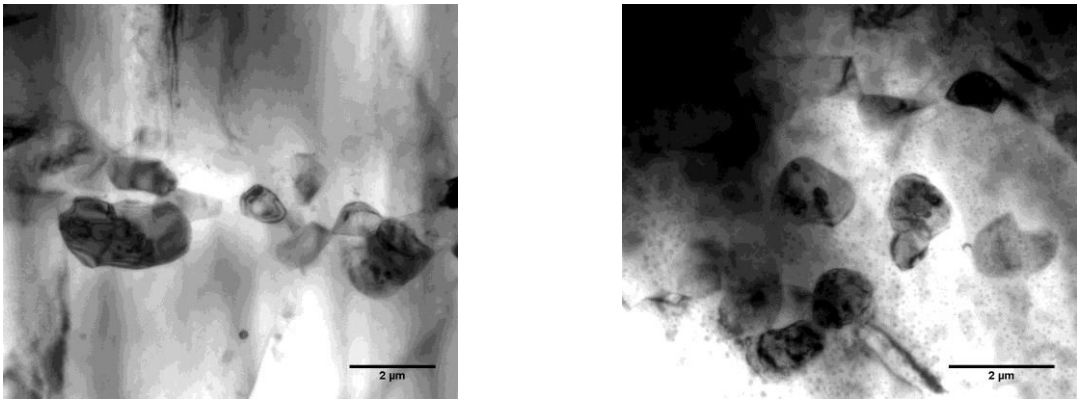

(a) (b)

Figure 48: TEM observations: bright field of areas of second phase particles after extrusion at 400 °C.

Detailed observations of the microstructures as displayed in Figure 46 (e) show that the eutectic mixture was strongly modified by the ECAP process: very small particles are observed (between 100 nm and 600 nm according to the image analysis). The size of these particles matches the ones of the Mg_2Ca lamellae in the cast eutectic mixture. Thus, this suggests that the formation of the fine particles result from the

fragmentation of the eutectic mixture. Such high refinement efficiency by ECAP processing has also been reported in the literature. For instance, in an AZ91 magnesium alloy, the second phase has been refined into particles sizing around 1 µm after 6 passes through route B_C of ECAP processing [152]. Also, in a Mg-Zn-Y, particles ranging between 0.5 µm to 1 µm have been obtained after 8 passes through route B_C by fragmenting the eutectic microstructure [153].

In addition to the strong modification of the eutectic areas into particles, the ECAP process modifies the overall second phase distribution of the initial structure. This is illustrated by Figure 49: image (a) gives an overview of the microstructure of the ECAP sample; the images (b) and (c), taken at a high magnification, show the local morphological characteristics of the eutectic skeleton. In both images, the eutectic skeleton has turned to very small particles [100 – 600 nm]. But on image (b), the particles are dispersed into the matrix, whereas on image (c) the former dendrites are well recognized. Thus ECAP processing seems to locally produce a finer dispersion of the particles.

There is little information in the literature on the impact of the ECAP route on the dispersion of the resulting particles in Mg alloys. For instance, route B_C has been used with more or less efficiency for particles dispersion in the matrix ([154], [155], [156]) and, 8 passes through route B_A has also shown its potential to disperse a second phase in the matrix [157]. The area highlight in Figure 49 (a) may be the result of a highly localized plastic deformation by shearing during the process. However, it is not a dominant feature of the microstructure. In the present study, the followed route does not result in a homogeneous dispersion of second phase particles. As mentioned in the literature, a prior dispersion of the second phase by conventional extrusion may give better results [114] [121] [122].

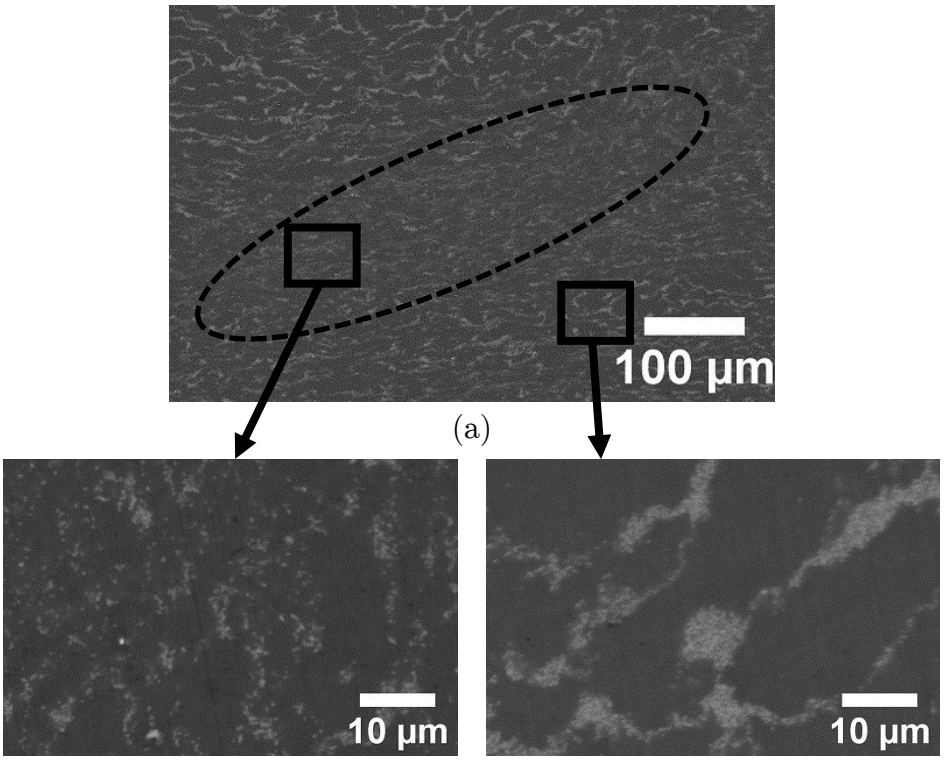

(a)

(b) (c)

Figure 49: SEM observations of an ECAP sample with a focus on two different second phase evolution area.

Further investigations on the second phase areas of the sample processed by ECAP have been conducted by TEM.

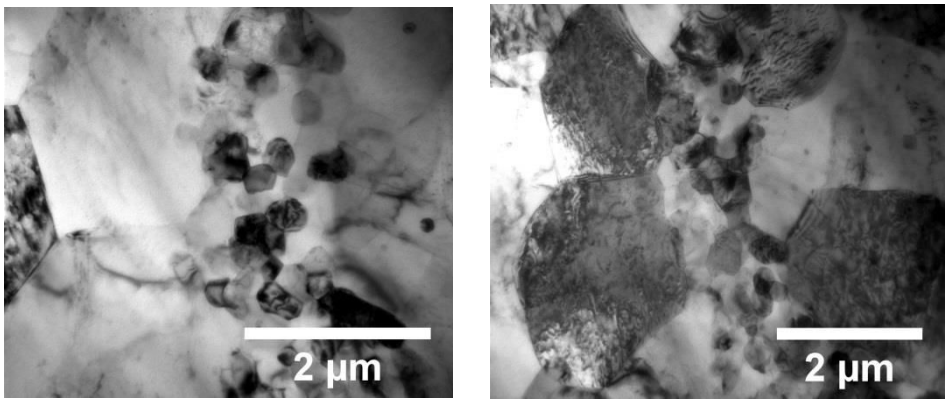

(a) (b)

Figure 50: TEM observations: bright field image of areas of second phase particles after processing by ECAP.

As illustrated in Figure 50, after ECAP processing there is a large colony of the second phase particles (dark contrast), with sizes ranging between 100 to 600 nm. These particles are gathering together with the recrystallized matrix around (average

size of 2 µm). Mixed with the Mg_2Ca particles, there are nanograins of Mg which are resulting from the fragmentation of the lamellae of Mg.

***

In conclusion, the microstructural investigations show that thermomechanical processing can strongly affect the as-cast microstructure. Except for extrusion at 200 °C, grain refinement is obtained. In addition, the thermomechanical processing has an impact on the second phase distribution in all cases. The initial structure is characterized by a Mg_2Ca second phase embedded in a eutectic mixture forming a connected skeleton within large grains. The utilization of different thermomechanical processing permits to obtain different microstructures.

By rolling, the skeleton of eutectic mixture is locally fragmented. This fragmentation is accompanied by recrystallization of the matrix (25 µm). By extrusion at 200 °C, in addition to local fragmentation, the skeleton of the eutectic mixture is also elongated in the extrusion direction. However, no recrystallization is observed in this case. Increasing the extrusion temperature up to 400 °C allows further modifications. The matrix of magnesium is recrystallized into grains with an average of 8 µm. The fragments of eutectic mixture are smaller than in the previous thermomechanical processing. Using TEM observations, particles of Mg_2Ca Laves phase are observed.

ECAP processing involves high shearing strain at each pass. This shearing severely deforms the eutectic mixture. By ECAP processing, the fragmentation of eutectic mixture led to into small particles of Mg_2Ca Laves phase and nanograins of Mg. In addition the matrix of magnesium turns into fine grains with an average grain size of 2 µm. Thus contrary to other thermomechanical processing involved in the present work, ECAP processing is able to completely redesign the microstructure of the sample at the finest scale.

4.5.3 Texture evolution

Thermomechanical processing is known for modifying the crystallographic texture. A pronounced texture may have some impact on the mechanical properties but also on the corrosion behavior. Thus, texture analysis of the processed samples has been carried out. Due to the large grain size of the as-cast and extruded at 200 °C samples,

a texture analysis of these states would not be meaningful. Thus, texture measurements were performed only on the following states: rolled, extruded at 400 °C and processed by ECAP. The sample being a two phase alloy, it could have been interesting to study both phases. However, the volume fraction of the eutectic mixture being very small (0.08), in the present experimental set-up, the intensity diffracted by Mg_2Ca could not be detected. Thus, only magnesium phase has been selected for the analysis. Based on the crystallographic structure of magnesium (h.c.p.), the following planes have been analysed: (0001), $(10\bar{1}1)$ and $(11\bar{2}0)$ (Figure 51).

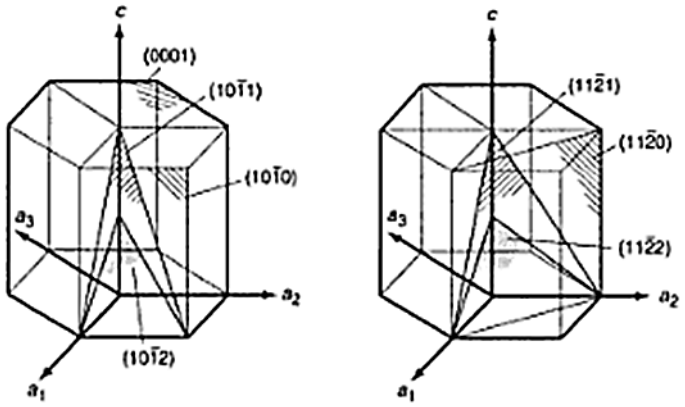

Figure 51: The magnesium unit cell crystal with principal planes [12].

For each condition, the 3D representations of pole figures, as well as 2D representations, are displayed. The colour scale is a relative scale based on the maximum of intensity that was measured for the whole batch of samples, Figure 52.

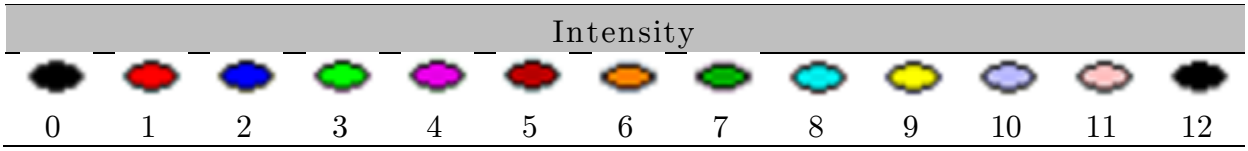

Figure 52: Intensity colour scale of pole figures.

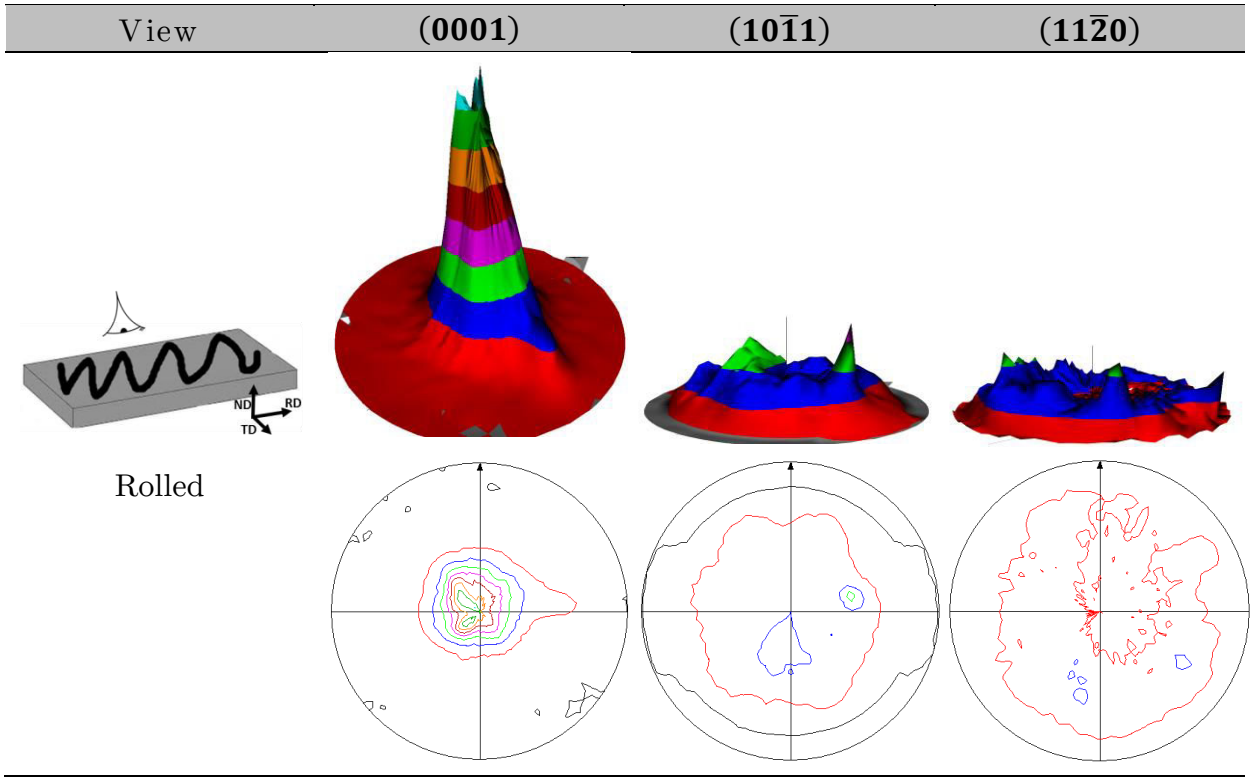

Figure 53: Pole figures of the rolled sample.

Figure 53 displays the pole figures obtained on the rolled sample. In the pole figures associated with the plane (0001), a strong and rather large peak is present at the centre of the pole figure. Such crystallographic orientation suggests a basal texture of the sample with the basal planes parallel to the rolling surface. On the pole figure associated with the plane $(11\bar{2}0)$, no visible peak is detected near the centre. However there is an almost complete ring of low signal intensity near the periphery of the pole figure. This is in agreement with the rather large peak observed for the plane (0001). This plane being perpendicular to the basal plane, the measured intensities of both planes are correlated. A central peak would have suggested the existence of peripheral pics on the pole figure of plane (0001). Indeed, there is a dark area at the periphery of each pole figure were the signal cannot be measured. Thus it is worth to complete an investigation with a complementary plane.

It is well known that h.c.p. material like magnesium exhibits a high tendency to deform by twinning [12]. When a crystal of magnesium has its c-axis perpendicular to the stress, slip on the pyramidal plane type II requires a higher stress than twinning $\{10\bar{1}2\}$, then a reorganization occurs by a rotation of 86.3 ° of the basal plan. Therefore, rolling is expected to produce many grains with the c-axis

perpendicular to the rolling direction [158]. The present texture is then a typical texture of hot rolling [159].

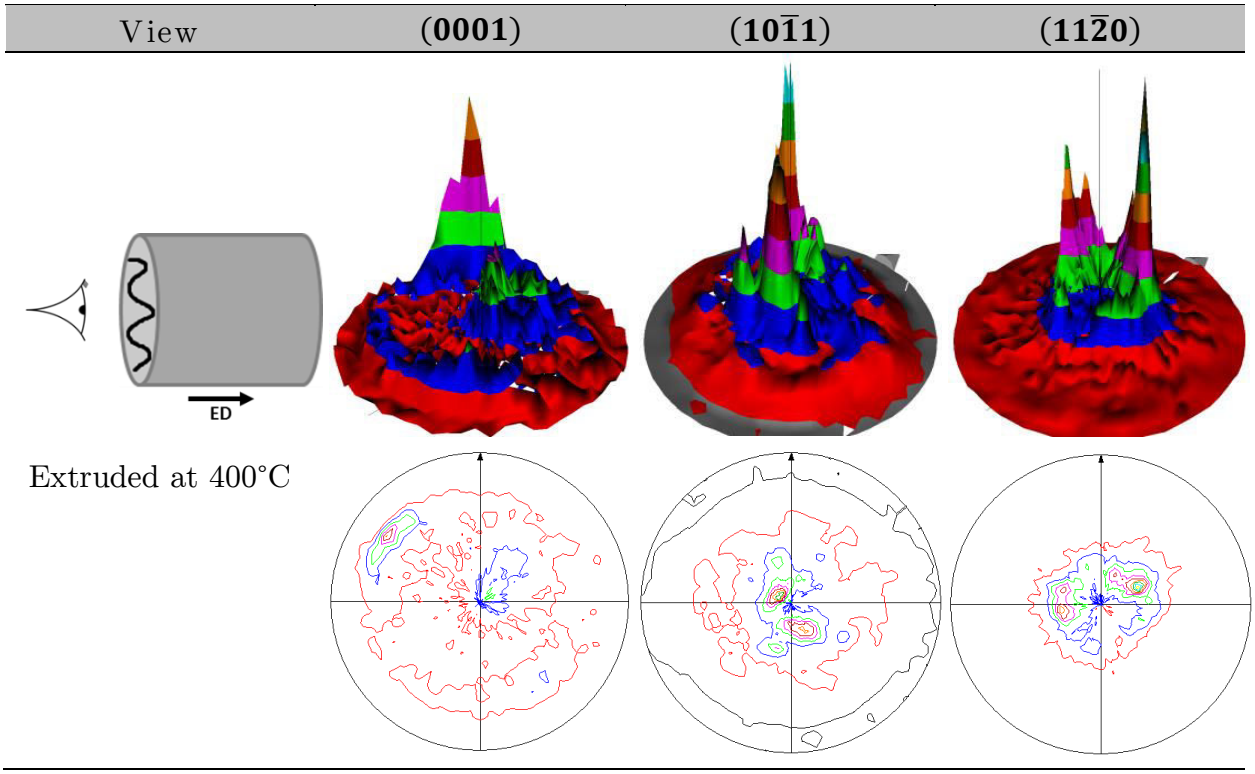

Figure 54: Pole figures of the extruded at 400 °C sample (cylindrical die).

Figure 54 displays the pole figures of the sample extruded at 400 °C. In these pole figures it is possible to note the presence of noise. On the pole figure of the plane $(11\bar{2}0)$ there is two peaks near the centre. These peaks are in agreement with the pole figure of the plane (0001): a partial ring of signal with an intense peak near the periphery. However, there is also a peak near the centre of the pole figure of the plane (0001). Finally, there are also few peaks near the centre of the pole figure for the plane $(10\bar{1}1)$.

In the literature, it is reported that direct extrusion generally produces a typical texture with the c-axis preferentially oriented perpendicularly to the extrusion direction [160]. In the present case, such texture should induce the formation of an intense peak near the centre for the plane $(11\bar{2}0)$. Based on the previous observations; some grains are orientated with their c-axis in accordance with this texture. However, there are also other peaks from the other planes. Thus, there is no strong fibre texture in the present sample.

In the literature, it is suggested that fibre texture is generally developed during extrusion process due to the limitation of slip systems [161] [162]. Thus, the weak texture of the present sample may be explained by the high temperature of the extrusion (400 °C): at this temperature, there is activation of different slip systems which may limit the impact on the texture. In addition, microstructural observations have shown that recrystallization has occurred during the extrusion at 400 °C. In the literature, it is reported that dynamic recrystallization during deformation at high temperature in magnesium may weaken the texture [163].

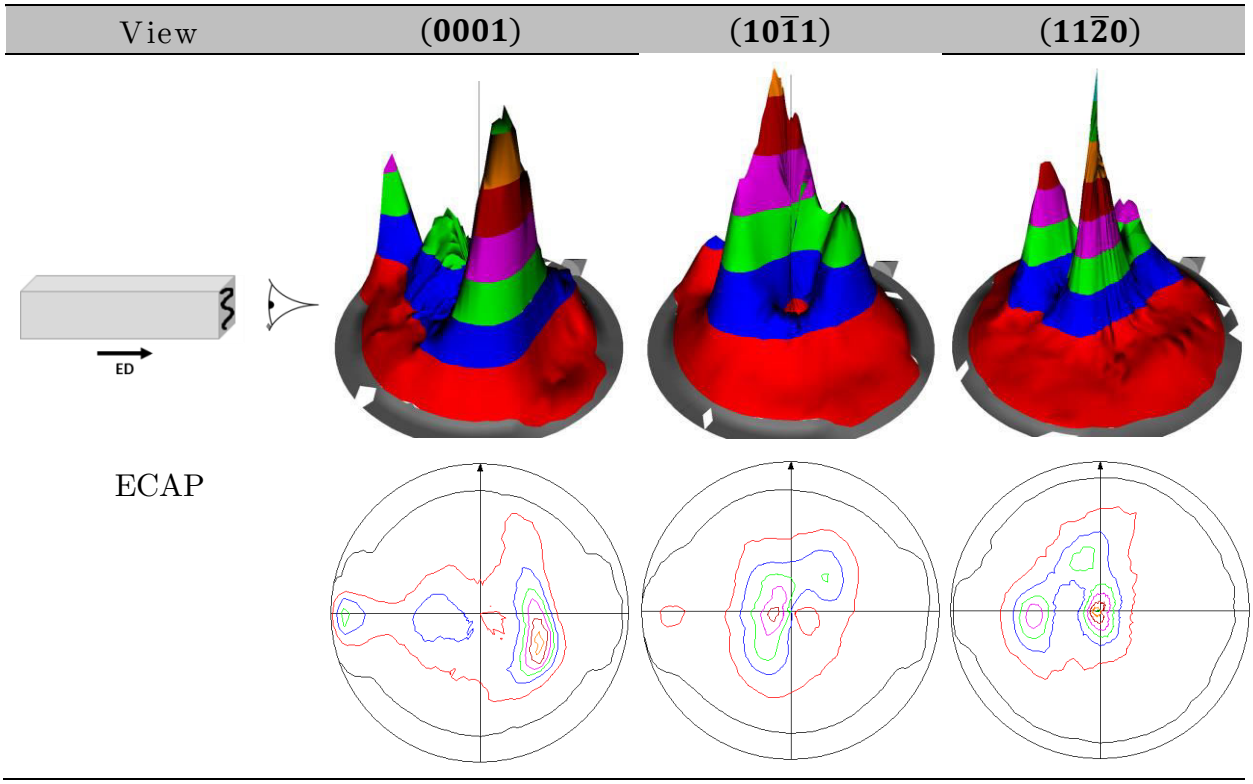

Figure 55: Pole figures of the sample processed by ECAP.

Figure 55 displays the pole figures of the sample processed by ECAP. In the present case, the pole figure of the plane $(11\bar{2}0)$ shows a central peak with high intensity with two peaks out of the centre. Such orientation of the $(11\bar{2}0)$ plane suggest the presence of basal planes perpendicular to the extrusion direction but also oriented between 0 ° to 90 ° with respect to the extrusion direction. Thus, the pole figure of the plane (0001) should possess some intensity at the periphery and also near the centre. Due to the dark area at the periphery, the intensity can't be checked at this location; only a small peak can be seen. However, a large peak near the centre is

accompanied by another one of lower intensity. The pole figure of the plane $(10\bar{1}1)$ also shows intense peak near the centre of the figure. Thus, these pole figures suggest that no preferential texture has been achieved by ECAP processing.

Route B_A used in the present work was chosen for the activation of different shear planes at each rotation, i.e. less redundant strain than with another route. As suggested by Wan et al. [164], formation of a strong texture with route A and C may be due to the accumulative shear strain on the same planes. Thus, in the present case, the weak texture may result from the alternation of shear plane.

4.6 Microstructure-property relationships

4.6.1 Microstructure and mechanical behavior

Relevant microstructural parameters for mechanical properties are the grain size, texture, density of dislocations, morphology and density of precipitates. From the present optical and SEM investigations some characteristics of these parameters are known. Table 12 gives a summary of the main microstructural features and the mechanical properties for the as-cast and thermomechanically processed materials.

Table 12: Microstructural features of the thermomechanically processed samples with the associated mechanical properties.

	Grain size	2nd phase	Texture	Hardness	Ultimate strength (MPa)	Maximum compression strain
As-cast	Several mm	Connected skeleton	-	40 ± 7	186	0.14
Rolled at 400 °C	≈ 25 µm + twins	Fragmented skeleton	Fibre	64 ± 7	-	-
Extruded at 200 °C	Several mm + twins	Fragmented + elongated skeleton	-	70 ± 6	277	0.02
Extruded at 400 °C	≈ 8 µm	Fragments + particles	Weak	46 ± 8	359	0.14
ECAP	≈ 2 µm	Particles [100–600 nm]	Weak	72 ± 3	325	0.20

The large grain size of the as-cast material is typical of the solidification microstructure and compatible with the measured low hardness. Each thermomechanical processing method has resulted in hardening. Concerning the rolled sample, different mechanisms may play a role in the hardness increase. Twins are known to reduce the dislocation motion in the basal direction [25]. Thus, the presence of twins may participate in the increase of hardness. Also, the rolled sample shows a strong texture with basal planes parallel to the rolling direction which was the indentation surface. This may have participated in the hardness increase as it has been reported the higher hardness of basal grains compared to non-basal grains [26]. The rolled sample was also subjected to short annealing which may has permitted the recrystallization process. However, the annealing was only 2 min and no annealing has been performed after the last pass. Thus, an additional effect due to work hardening may be suggested.

The sample extruded at 200 °C displays no recrystallization. This sample shows one of the highest hardness values and the lowest ductility. Thus, in this case, work hardening may be a major parameter, accounting for hardness increase. With SEM observations, it has also been noted that during the extrusion, an elongation of the second phase skeleton occur. This elongation leads to a reduction of the characteristic

width of the interdendritic space. Then, dislocation motion may be restricted by the proximity of the second phase rich area.

The sample extruded at 400 °C shows a small increase of hardness compared to the as-cast state. The microstructural characterization suggests that recrystallization has occurred leading to a rather small grain size. Thus, this hardness increase can be explained by a Hall-Petch effect.

By ECAP processing a finer grain size has been obtained than with extrusion at 400 °C. Then, the higher hardness of sample processed by ECAP would be in accordance to Hall-Petch law. However, in the case of ECAP sample, the second phase is dispersed in small particles of submicrometric size. Therefore, this material could behave as a magnesium matrix composite with enhanced mechanical properties (e.g. strength). Thus, in the present case, the particles of the Mg2Ca intermetallic may be seen as particles reinforcements.

The higher ductility of the sample processed by ECAP may also be related to a combination between grain size and texture. As described in Section 2.1.2.1, in magnesium there are dislocation slip planes available for deformation at room temperature (basal and prismatic). Due to the small grain size in the sample processed by ECAP these deformation mechanisms are easily blocked. Thus, a concurrent deformation mechanism may be activated at sufficient stress. Twinning during compression test in magnesium alloys is well-known and occur primary along the $\{10\bar{1}2\}$ plane [27]. Thus, twinning may occur in the favourably oriented grains. This twinning may be responsible of the inflection observed at approximatively 125 MPa in the compression curve of the sample processed by ECAP. Once twinning occurs, there is a reorientation of the crystallites (rotation by 86 °) with less favourable planes orientation for slipping [28]. In order to promote new deformation mechanisms, a higher level of stress has to be obtained. Koike et al. [29] have reported grain boundary sliding during deformation at room temperature of a AZ31 alloy with an average grain size of 8 µm. Thus, due to the small grain size of the sample processed by ECAP, in addition to dislocations sliding and twinning, grain boundary slipping may occur. This combination of different deformation mechanisms may take a part in the increase of strength and ductility.

To summarize, the microstructural investigation points out that the key features to account for the improvement in the mechanical behavior are probably the grain size reduction and the dispersion of the second phase particles in a fine scale distribution. Both features can be tuned by the thermomechanical processing, that appears as a very efficient tool for optimizing the mechanical properties of the studied Mg-2wt.%Ca alloy. It is worth noting that the ECAP treatment is particularly efficient because it is able to refine both the grain microstructure and the second phase particle distribution.

4.6.2 Microstructure and corrosion behavior

Table 13 reports the corrosion measurements of the as-cast and mechanically processed materials with the associated microstructural observations.

Table 13: Microstructural features of the thermomechanically processed samples with the associated corrosion measurements.

	Texture	Grain size	2^{nd} phase	Mass loss rate ($mg.cm^{-2}.day^{-1}$)	R_{tot} at t = 1H ($\Omega.cm^2$)
As-cast	-	Several mm	Connected skeleton	3.6	200
Rolled at 400 °C	Fibre	≈ 25 µm + twins	Fragmented skeleton	1.5	150
Extruded at 200 °C	-	Several mm + twins	Fragmented + elongated skeleton	0.4	-
Extruded at 400 °C	Weak	≈ 8 µm	Fragments + particles	0.6	2400
ECAP	Weak	≈ 2 µm	Particles [100 – 600 nm]	0.1	11500

As described in the literature review, the corrosion behavior may be impacted by the different parameters displayed in Table 13: grain size, second phase morphology and texture. However, thermomechanical processing modifies all these parameters at the same time. It is then difficult to isolate one effect for quantification. Nevertheless, in the present case, one can note that increasing the equivalent strain from rolling to extrusion and then ECAP processing, the associated mass loss rate decreases.

Concerning the textural evolution, only the rolling processing induces a strong texture. However, the grain size decreases (excepted for the sample extruded at 200 °C) and the skeleton of second phase is progressively refined. Indeed, the as-cast sample displays a connected skeleton and a very poor corrosion resistance while, for the thermomechanically processed samples, this skeleton is fragmented and even dispersed as very fine particles.

For magnesium-calcium alloys, Harandi et al. [30] have reported that, up to a certain limit, calcium addition increases the corrosion resistance of pure magnesium. Above 1wt.%, Harandi et al. have reported an increase in the degradation rate in simulated body fluid [30]. However, Seong et al. [31] have reported the possibility to reduce the corrosion rate of two Mg-Ca alloys (Mg-2wt.%Ca and Mg-3wt.%Ca) through high-ratio differential speed rolling. They account this enhancement to the significant refinement of the second phase Mg_2Ca [31]. As reported by Kim et al. [32], the second phase, Mg_2Ca, being more anodic than magnesium, a microgalvanic effect occurs. Jeong et al. [33] have proposed the following illustration of the microgalvanic effect to show the effect of a continuous or discontinuous distribution of Mg_2Ca in the Mg matrix, Figure 56. It is suggested that the same mechanisms apply to the present case.

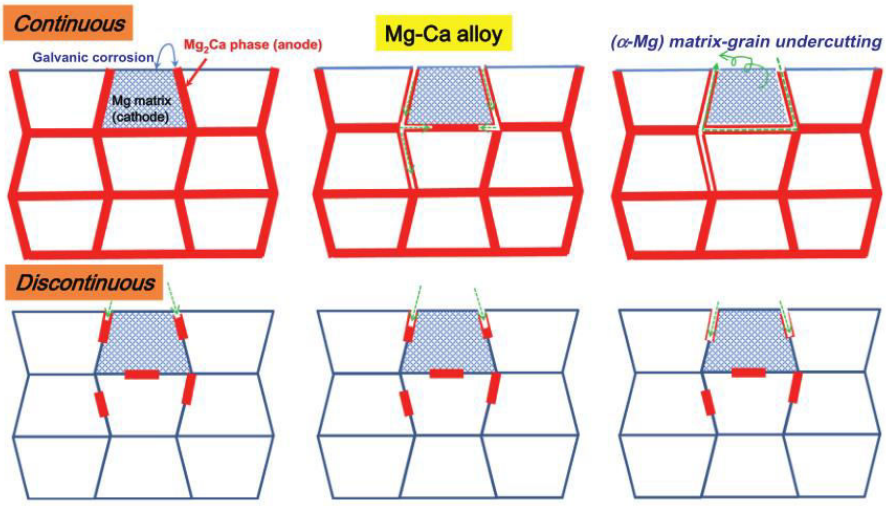

Figure 56: Schematic illustration of the morphologic impact of Mg2Ca phases in Mg-Ca alloys [33].

Thus, in the present case, to further examine the impact of the continuity/discontinuity of the second phase skeleton, two states (as-cast and extruded at 400 °C) were investigated after immersion in Hanks solution. Figure 57

displays the optical micrographs of these two samples after 7 days of immersion (for these observations, corrosion products were removed).

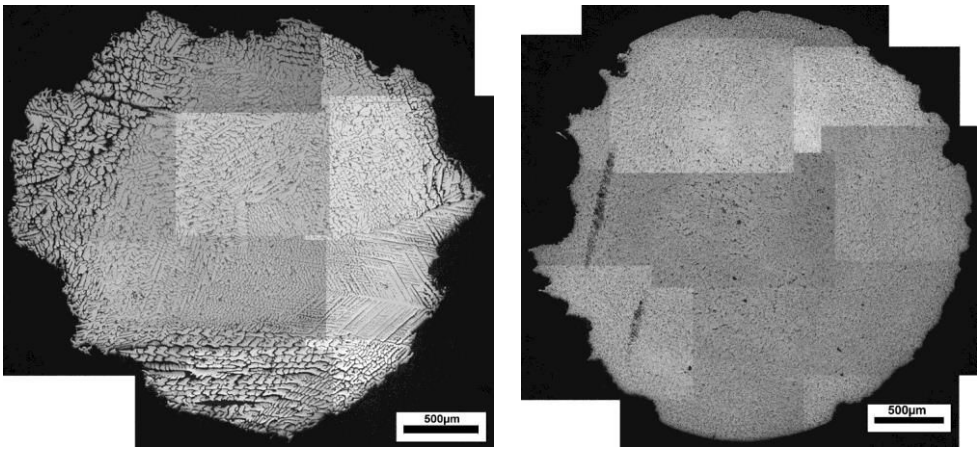

(a) (b)

Figure 57: Optical observation of the cross sections of the corroded samples after 7days of immersion in Hanks solution: (a) as-cast and (b) extruded at 400 °C. Note that the interdendritic zones appearing with a black contrast are empty.

Figure 57 (a) shows that in the as-cast sample after corrosion, the connected skeleton of the second phase is partly dissolved due to corrosion. In contrast to the sample extruded at 400 °C does not show the same feature due to corrosion (Figure 57 (b)). The as-cast sample, showed in Figure 57(a), exhibits extensive corrosion starting at the surface and following the interdendritic areas. As a consequence, the corrosion process has proceeded deeply inside the sample. The sample extruded at 400 °C (Figure 57(b)) shows limited corrosion, starting from the periphery and no penetration inside the sample. Figure 58 gives high magnification images of the subsurface area of the corroded as-cast sample.

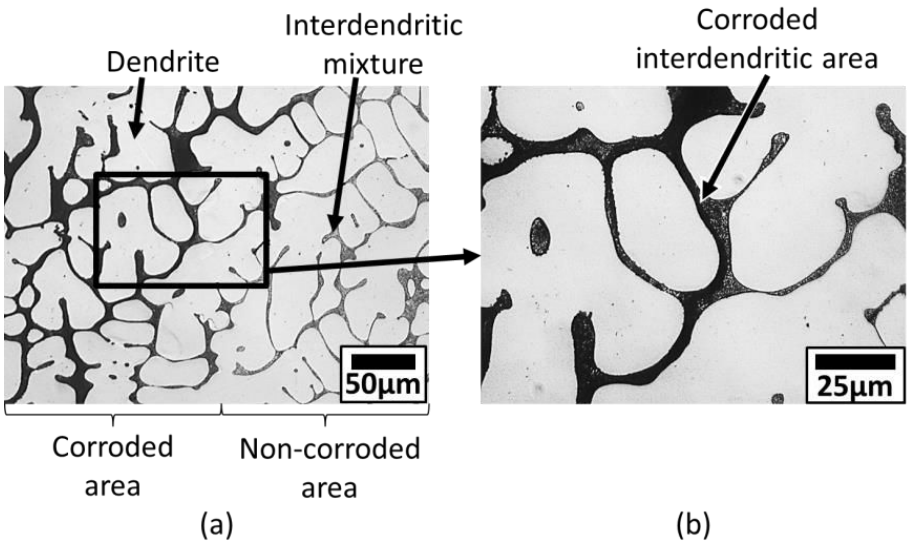

Figure 58: Optical microscopy observations: (a) Sub-surface area of a corroded as-cast sample after 7 days of immersion in Hanks solution and (b) a higher magnification image of a corroded area.

Figure 58(a) shows the corroded areas with empty interdendritic regions (black contrast) and non-corroded areas where the interdendritic region is still filled with the eutectic mixture. As pointed by zooming in the corroded part (Figure 58(b)), it appears that the corrosion process has occurred primarily in the eutectic mixture. The eutectic mixture is then corroded instead of magnesium and fell apart. When such microgalvanic effect takes place in the eutectic mixture contained in the interdendritic areas, corrosion can penetrate deeply into the sample. By refining this second phase rich skeleton, it is then possible to reduce this microgalvanic corrosion.

This kind of mechanism is corroborated by the evolution of the resistance of the different samples in function of the immersion time (Figure 43). The decrease of the resistance in the first hours of immersion for the as-cast and rolled samples may be due to the continuous reactivity of the eutectic mixture. The galvanic effect allows the corrosion to progress inside the material. In the case of the rolled sample, the corrosion process begins to decrease quickly. The sample extruded at 400 °C shows a slower decrease of the corrosion resistance. Indeed, compare to the rolled sample, in the sample extruded at 400 °C, the eutectic mixture is more fragmented and it is also elongated.

The sample processed by ECAP shows the highest corrosion resistance. In addition, this high corrosion resistance seems rather stable during the immersion time. Thus, in

addition to the drastic reduction of the galvanic effect due to the second phase refinement, the high corrosion resistance of the microstructure processed by ECAP, suggests that another parameter may enhance the corrosion behavior.

The other important microstructural parameter impacted by ECAP processing is the grain size. Several studies on different magnesium alloys have reported that the corrosion resistance improves with a reduction in the grain size [16], [34], [35], [36]. According to Kainer et al. [37], the high compression stresses between the magnesium lattice and the oxide layer may lead to cracks into the oxide layer. Birbilis et al. [34] have reported that a higher density of grain boundaries coupled with high misorientation angles may help the stability of the oxide layer. This phenomenon would account for a better corrosion resistance by grain refinement in the case of ECAP processing.

The present interpretation was focussed on the major microstructural features, namely grain size and second phase skeleton. However, texture is also known to impact the corrosion resistance of magnesium alloys For instance the basal plane orientation is suggested to provide a better corrosion resistance [38], [39]. In the present case, the strong basal texture of the rolled sample may account for the high increase of the corrosion resistance despite the limited fragmentation of the eutectic mixture skeleton. However, for the other states, no preferential texture has been observed thus it is not possible to conclude on the effect of texture in the present work.

The presence of dislocations and twins in the microstructures can also modify the corrosion behavior [36], [40]. Thermomechanical processes employed in this study have also probably modified the dislocation density in addition to other microstructural parameters. However, no obvious impact of dislocation density on corrosion behavior has been detected. From this investigation, grain size and second phase morphology appears as having the higher correlation with the corrosion enhancement.

4.7 Conclusions

As a conclusion of this chapter, it is possible to point out the following points:

- Thermomechanical processing appeared as an effective way to improve the mechanical properties and corrosion resistance of a Mg-2wt.%Ca alloy. These thermomechanical processing routes all result in tailoring the grain size and second phase microstructure into finer features.

- Comparison of the various processed samples indicates that the improvement in the mechanical strength and the corrosion resistance are strongly affected by the grain size evolution and the population of second phase particles. While different microstructural features (dislocations, twins, grain size) can account for the increase of the mechanical strength, the evolution of the corrosion resistance appears as primarily affected by the second phase microstructure and grain size. This influence results from the combination of a micro-galvanic effect, the dispersion of the second phase Mg_2Ca and possibly a more stable oxide layer.

- Severe plastic deformation induced by the ECAP process produces the finest microstructure: grains and second phase particles with a highly improved corrosion resistance in Hanks solution. In practice, the corrosion resistance is evaluated to be about 40 times higher in the sample processed by ECAP compared to the as-cast one. High level mechanical properties were also obtained using ECAP. This processing makes possible to improve both mechanical and corrosion behavior in a magnesium alloy containing only a small amount of calcium.

5. Surface functionalization using additive manufacturing

The goal of the present work is to improve the surface characteristics of a Mg-Ca alloy for biomedical application as degradable implants. For this purpose, surface functionalization is performed on thermomechanically processed samples with improved mechanical and corrosion behavior. ECAP processing was carried out in the last year of this thesis; thus the samples were not available for the surface functionalization studies. Therefore, the sample extruded at 400 °C was chosen for this study.

The surface functionalization process aims to provide an antibacterial capability to the material; using a silver deposition to the surface. Using an additive manufacturing technology, patterns of silver nanoparticles are deposited on the surface of the sample. This surface is then subjected to a heat treatment by laser to sinter the deposition. At first a systematic work had to be carried out in order to determine the parameters for optimizing the quality of the deposit. The preliminary results of patterning, as well as the related characterizations study are reported here. In addition, a simple finite element modelling study, which has been conducted to help future choices of patterning parameters, is reported. The input parameters of this model will be selected based on the previous microstructural observations. As in the previous chapter, this chapter is started with the literature focused on this subject and then continued with the results and discussion.

5.1 Focused literature review

During an implant surgery, a bacterial contamination may happen despite all the strict protocols taken to avoid it [165]. These infections can lead to serious complications involving surgery or drug treatments. Thus, surface functionalization aiming at a reduction of the risk of infection would provide a major improvement in implant performance. A first solution was to use antibacterial coatings [166]. They consisted of antibiotics integrated in coatings which could release them progressively [167]. Such localized drug administration targets the potentially infected area, permitting to use a lower amount of antibiotics. However, bacteria may develop a resistance against antibiotics making the coating not effective [168]. Silver could be considered as antibacterial agent to solve the infection issues related with surgeries. Silver is already used in medical applications such as dental procedures, catheters and burn wounds [169]. The antibacterial effect of silver is attributed to the silver ions binding to the bacteria membrane and finally causing its death [21] [170]. Due to the mechanisms involved, a bacterial resistance to silver ion has a low probability to occur [167] [170]. Another advantage of silver is to be efficient against the bacteria responsible for the majority of infections (Pseudomonas aeruginosa, Escherichia coli, Staphylococcus aureus, and Staphylococcus epidermidis) [168]. Moreover, it has been reported that silver coated materials did not show toxicity on osteoblast cells [171]. With all these beneficial effects, silver is a promising agent for biomedical usages. Therefore, silver containing coatings could be of high interest for implants applications.

The literature on silver-containing coatings reported on magnesium alloys is not rich. An antibacterial effect has been reported after silver ion implantation on a Mg-Ca-Zn alloy [172]. A continuous film of silver has also been achieved by plating on a AZ31 substrate, previously coated with an organic layer but no bacterial test were performed [173]. There are also some works on titanium based devices. For instance, titanium/silver coating deposited by physical vapour deposition on titanium has shown a good biocompatibility with an antibacterial effect [174].

In addition to surface functionalization targeting a reduction of the risk of infection, surface modification may also help to better implant-body integration. With a better

integration, complication (foreign body implant, implant loosening) may be avoided and the healing process may be faster.

To improve implant integration, specific designs of the surface topography at the nanoscale and microscale have been proven efficient [175]. Indeed protein adsorption is helped with a nanoscale roughness that allows for a better wettability by blood. On the other hand, cell adhesion is better on surface showing a microscale roughness. A beneficial impact on cells has been reported for topographic designs in the 10 to 100 µm range [176]. Figure 59(a) illustrates how microtopography can help the cell adhesion and further cell colonization during the healing process first steps. For instance, beneficial effects on cell proliferation have been reported for a magnesium-calcium alloy with a porous surface [150] Figure 59(b).

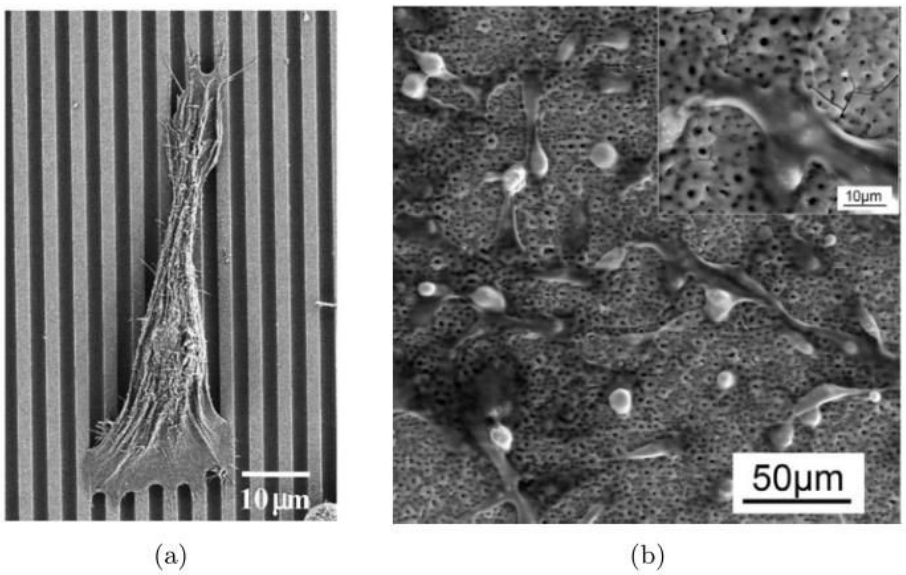

Figure 59: (a) SEM image of epithelial cells cultured on patterned silicon substrate [177] and (b) osteosarcoma cell line proliferation on a Mg-Ca sample treated by microarc oxidation [150].

Surface topography is commonly produced by polishing, sand blasting, etching or lithography. More sophisticated procedures, like laser texturing or patterning using electron beam evaporation have also been employed [178] [179] [180]. For instance, the osseointegration and bacterial adhesion of titanium alloys for dental and orthopaedic implants, processed using a multiscale femtosecond laser to produce a surface topography have been reported [179]. Sealy et al. [91] have also investigated patterning with a laser approach. It has been shown that by varying the beam

conditions, different patterns can be created on a Mg-08wt.%Ca alloy using a sequential laser shock peening process (Figure 60) [91].

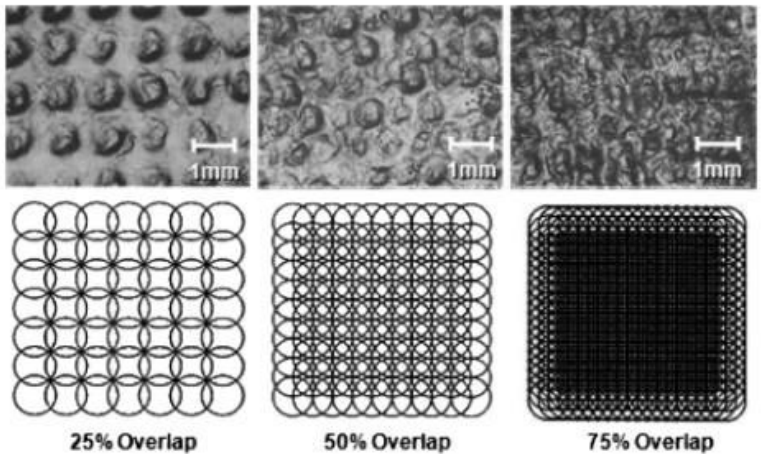

Figure 60: Comparison of experimental peening pattern with different beam overlapping [91].

Topographic patterns have also been obtained by template-assisted electrohydrodynamic atomization spraying [181]. This technique, which is based on spraying under high voltage of a liquid suspension on the substrate, has been investigated for metallic implant applications [181]. For instance, hydroxyapatite deposition showing different pattern geometry has been obtained on titanium as shown in Figure 61 [182]. According to *in vitro* cell culture, osteoblast cells are able to attach and grow on these patterns [182].

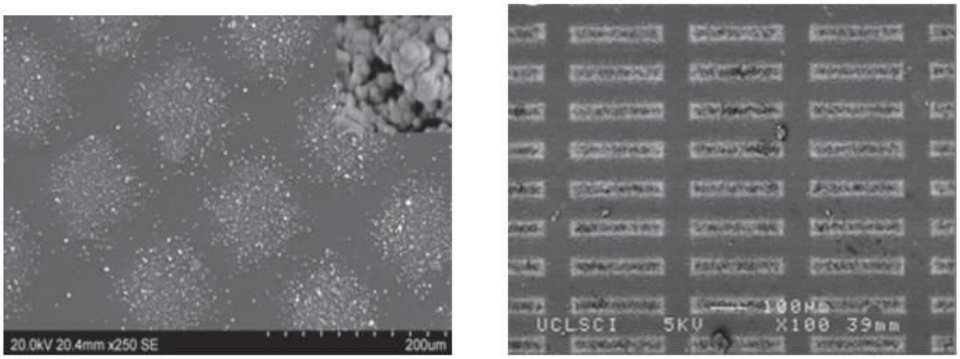

Figure 61: (a) SEM image of pillar pattern of nanoparticles of silicon-substituted hydroxyapatite after heat treatment at 600 °C and (b) SEM image of nanoparticles of a silicon-substituted hydroxyapatite pattern [182].

***

Based on the previous literature, in addition to the antibacterial effect, making a specific topography on the implant may help the healing process. A pattern with a design scale ranging from few micrometres to one hundred micrometres would help the cell adhesion. An additive manufacturing which can produce patterns of this scale on different kinds of materials has been reported [41]. This method, called laser-assisted maskless microdeposition (LAMM), is mainly used in micro-electronics to produce print circuit.

The LAAM technique is a layer-by-layer additive manufacturing method designed to create simple or complex geometrical patterns. It allows depositing a large variety of materials such as electronic inks, polymers, biomaterial materials, nanoparticles onto various surfaces [24]. Furthermore, this technique permits to deposit on both planar and non-planar surfaces [24]. It has been reported that the LAAM process can realize a continuous or discontinuous pattern with a specific geometry and a minimum width of 10 µm and a minimum thickness of 100 nm. It is also possible to obtain very thick layers by several passes on the same deposition or with a slow deposition velocity. Some examples of patterns are shown in Figure 62. During this deposition step, the sample is heated up to 80 °C using a hot plate integrated on the stage. This high substrate temperature aims at improving the wettability of the substrate and thus a better deposition.

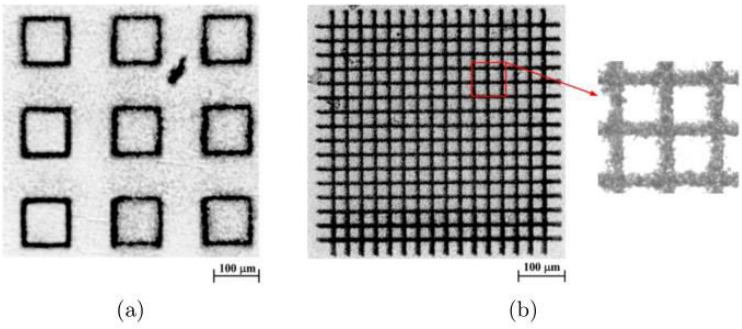

Figure 62: Patterns of nano-silver deposition on a magnesium substrates: (a) squared patterns with 10 layers of deposition and (b) cross-lines pattern with 20 layers of deposition [41].

As the term “laser-assisted” implies the deposition process includes a heat treatment by laser, contrary to furnace sintering, such a laser treatment has the advantage of a localized heating at the surface that normally keeps the bulk microstructure intact. Sintering of silver particles pattern has already been done successfully with a laser

source on a magnesium substrate [24] [41] [48]. However, these previous studies were done with a pulsed laser, contrary to the present case for which a continuous wave laser is used. For its potential to deposit silver nanoparticles onto the previously bulk improved Mg-Ca alloy it has then be chosen to use this additive manufacturing machine for the present work.

5.2 Materials and methods

5.2.1 Laser-assisted maskless microdeposition (LAMM)

In present study, the LAAM method was used to pattern a sample previously engineered by thermomechanical processing. An overview of the machine and its main parts is given in Figure 63, it consisted of the in-house build combination between an additive manufacturing machine (Optomec Maskless Mesoscale Material Deposition[6] (M^3D)) and a laser system added to the deposition machine. The LAMM process was carried in two steps: first the deposition of the selected ink onto the substrate using the M^3D system and second, the sintering of the deposited pattern using the laser.

In the present work, the selected ink was a suspension of silver nanoparticles from Cabot Corporation. The solution was made of 45 to 55 wt.% of silver nanoparticles (average size $<$ 60 nm) mixed with ethylene glycol. The ink was diluted as follows: 1 mL of the silver solution + 3 mL of distilled water [48]. This dilution permits to obtain a viscosity of 2.35 mPa.s and thus a good aerosol atomization. Micro-droplets were created inside the ink vial using the ultrasonic bath, combined with a gas injection system to form an aerosol, and then carried to the deposition head. In the deposition head, the aerosol was focused by an aerodynamic system.

[6] This machine can be found under the reference *Aerosol Jet 300 Series Systems* on Optomec website: www.optomec.com

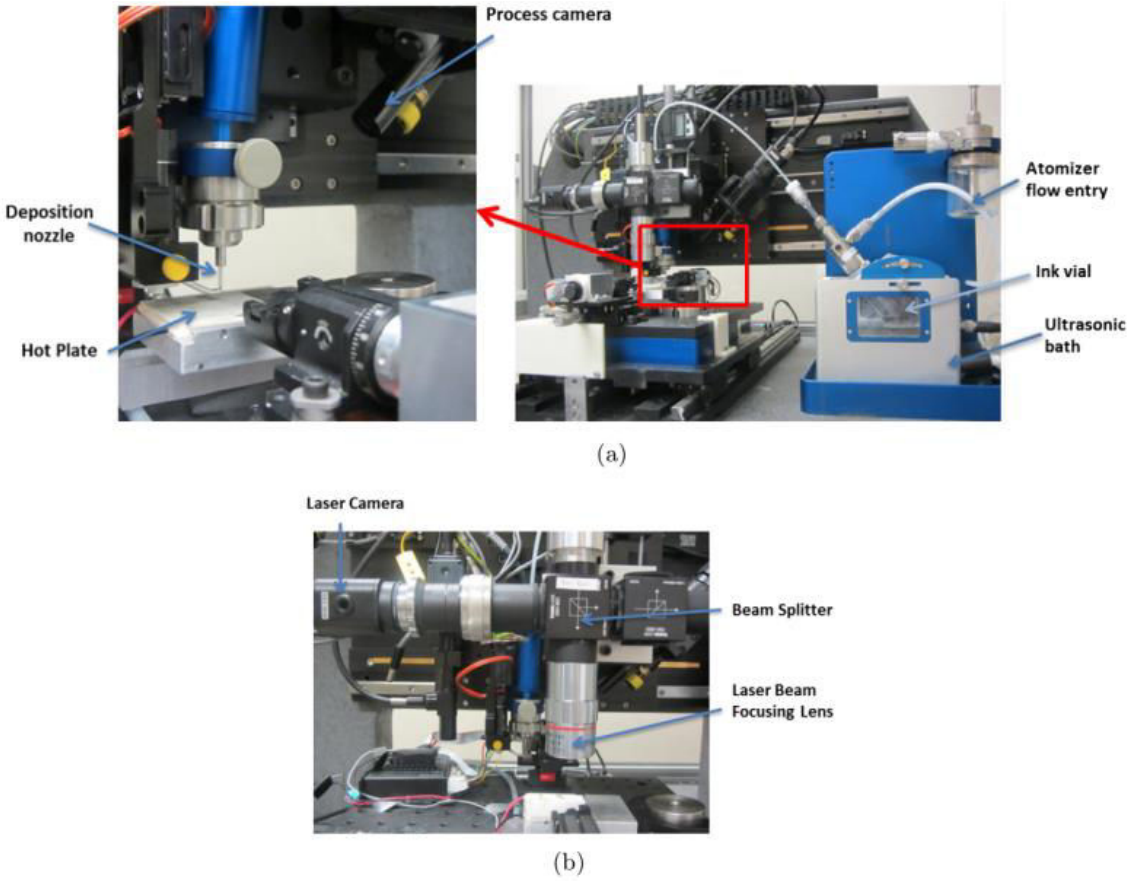

Figure 63: (a) Images of the Optomec Maskless Mesoscale Machine and (b) laser system for sintering [49].

As represented in Figure 64, there were two gas entries within the deposition head: one for the aerosol flow and the other one for a neutral gas (nitrogen), i.e. sheath gas. The sheath gas was used to reduce the size of the aerosol flow to a tenth of the nozzle's internal diameter and guide the aerosol onto the substrate. A 150 µm diameter nozzle was used permitting to reduce up to 15 µm diameter the aerosol flux. The pattern is then created by the motion of the substrate during the aerosol flow. The motion of the stage in the x and y directions was monitored using a trajectory file made with the 2D application of the AutoCAD software.

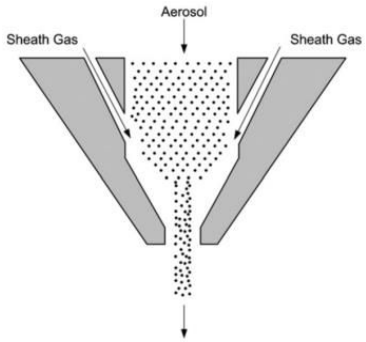

Figure 64: Focusing of the aerosol stream in the deposition head of the LAMM machine [24].

Before patterning, the samples were polished using abrasive papers up to 4000 grit and ethanol for the last step. The samples were cleaned in ultrasound with ethanol for 1 min and then set-up in a sample holder to avoid any displacement during the deposition due to table vibrations or air flux on the edges (Figure 65).

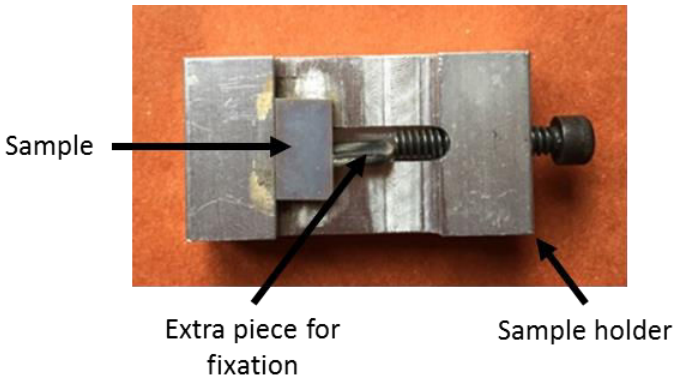

Figure 65: The aluminium sample holder system used for the silver deposition process.

The deposition quality depended on many adjustable parameters concerning the atomization and the deposition steps:

- the liquid atomization set-up with the power input and the quantity of water for the ultrasound bath, the position of the vial, the level of ink inside the vial,
- the deposition set-up with the flow of the carrier gas for the nanoparticles, the flow of the sheath gas, the deposition velocity and the distance between the nozzle and the substrate

These settings were adjusted during a period of tests. Several depositions were performed in order to determine the experimental parameters and achieve a reproducible silver nanoparticles pattern. These parameters will be detailed in Section 4.3.

Once the pattern is achieved, a laser treatment can be applied to heat treat the deposited ink and ensure a better adhesion. A continuous wave Erbium fiber laser from IPG Photonics is used to sinter the nanoparticles. This laser is characterized by a TEM_{00} transverse mode with a wavelength of 1550 nm. It can deliver a power ranging from 0.5 W to 20 W and the beam radius is 15 µm at the focused point.

Different levels of sintering can be achieved. In Figure 66, copper particles agglomerations after different process conditions are depicted. When the sintering is complete, a fully dense coating, which has a smoother surface, is obtained. A partial sintering process, stopped at the necking stage, preserves a part of the nanoparticles morphology allowing for nanotopography.

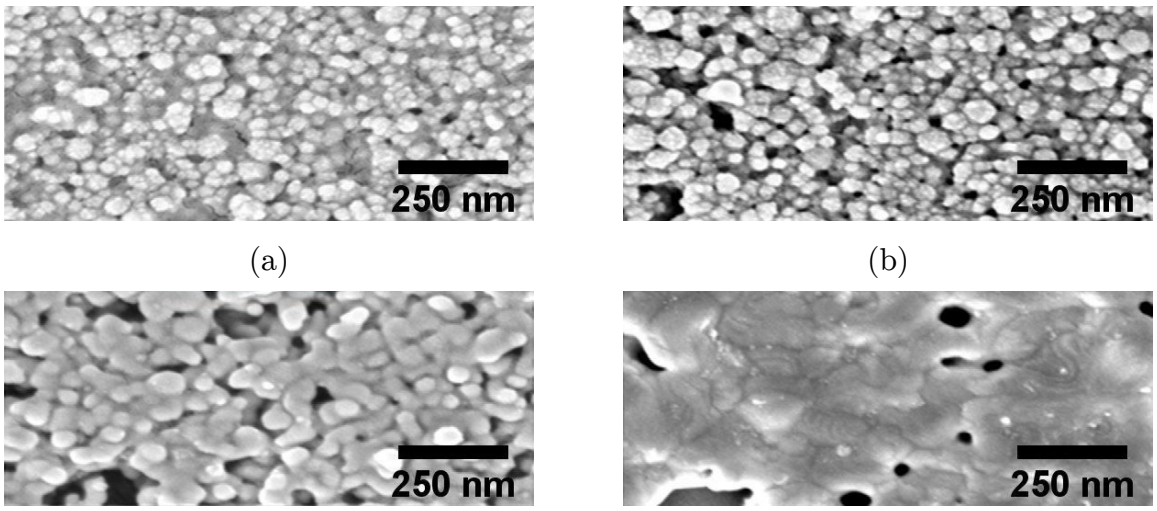

Figure 66: SEM images of an ink containing nanoparticle mixture of copper deposited by spin-coating on a glass substrate: (a) unsintered, (b) organics partly removed, (c) nanoparticles necking takes place and (d) grain growth, i.e. extensive sintering – Images adapted from [183].

For biomedical applications, nanotopography may improve proteins adsorption which would enhance cell interaction. In the present project, SEM observations were performed to determine the laser parameters allowing fine scale topography on the surface of the deposited tracks, i.e. sintering performing necking between nanoparticles but not a complete densification. This sintering condition would then provide to the silver deposition a fine scale topography that can be of interest with respect to the cell interaction. This beneficial effect would be combined with the potential beneficial impact of the pattern itself to the cell adhesion. Thus, in the present case, the pattern would provide microscale topography on the surface of the

substrate and nanoscale topography would be provided by the surface of the deposited pattern.

5.2.2 Profilometry

Optical profilometry, which is a non-contact method, was used to determine the surface roughness of the samples. This method provides information at different scales of the topography of the studied sample. The WYKO NT1100 optical profiler, from the Center for Advanced Materials Joining at the University of Waterloo, was used to evaluate the quality of the deposit. The system possessed three different magnifications (x 5, x 20 and x 50) and double magnifying removable lens. After data acquisition (here using the software Vision) a 3D mapping of large areas (square millimetre) was obtained with a submicrometric resolution.

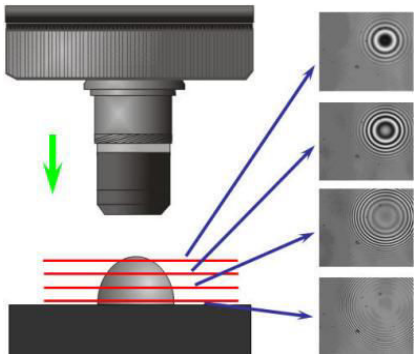

Figure 67: Interference patterns of a spherical object at different heights of the objective [184].

5.2.3 SEM and TEM techniques

Top surface evolution of the silver nanoparticles patterns under laser treatment was studied using SEM on a LEO FESEM 1530.

Cross section characterizations were carried out after Focused Ion Beam (FIB) nano-machining. The FIB nano-machining was obtained by scanning a focussed gallium ion beam on the material using a ZEISS NVision 40 FIB system operated by the Consortium des Moyens Technologiques Communs (CMTC) from Grenoble Institute of Technology. Thus, direct SEM observations were realized *in situ* on the samples. Using this technique, it was then possible to have a cross section view of the

deposition, the deposit/substrate interface and the sublayer of the substrate just under the deposition.

In addition, thin sections of a patterned sample with the following dimensions: 15 µm * 5 µm * 2 µm were performed. Indeed, the FIB technique allows for cutting of cross sections adequate for SEM or TEM observations. Conventional TEM imaging on bright field and dark field have been carried out on these thin sections.

TEM was also used for very dedicated microstructural analysis since this microscope JEOL 2100F equipped with a field emission gun is fitted with an automatic phase and orientation mapping device. This so called ASTAR/ACOM [185] equipment is based on the scanning of the electron beam coupled with an automatic indexation software that allows for the creation of a map, showing either the distribution of the phases or the orientation for a specific phase. Chemical mapping can also be performed on this instrument.

5.3 Patterning process

The optimization of the deposition parameters was based on multiple deposition tests. The trajectory file, used for monitoring the deposition, described a cross-line pattern as represented below (Figure 68), the variable distance (x) between the lines allows for various coverage percentages of the surface. The width of the lines was determined by the nozzle (see Section 4.2.1). The design of the pattern would allow investigating the impact of the distance between the lines on cell behavior. Different surface coverage could also be performed to investigate the impact on corrosion behavior.

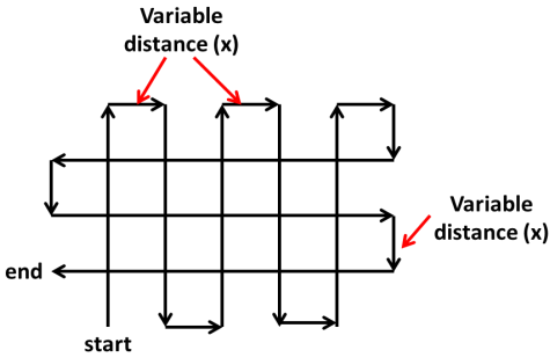

Figure 68: Deposition template used to perform a cross-line pattern with a variable distance (x) between the centres of the deposited lines.

In the first step of the patterning effort, a range of settings has been determined to obtain continuous deposition. Figure 69 (a) shows an optical micrograph of one of the first deposition tests. Obviously, this deposition (Figure 69 (a)) does not have a good quality: the deposition is spotty and the width of the lines is not homogeneous.

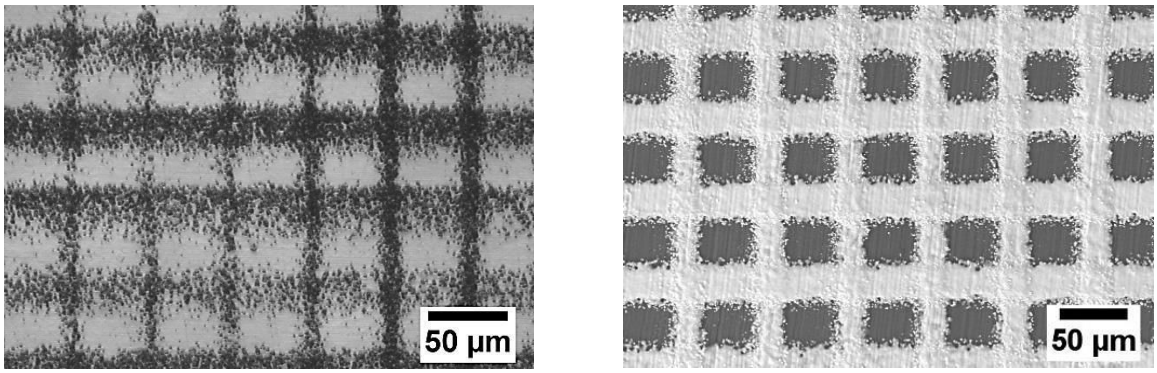

(a) (b)

Figure 69: (a) Optical micrograph of an initial deposition test during the optimization deposition campaign and (b) SEM image of patterned deposition with optimized parameters.

Further optimization of the machine settings (for instance, location of ink vial relative to the ultrasonic actuator, and atomizer voltage) and deposition parameters has been performed to improve the aerosol atomization process. Owing to these optimization efforts, it is possible to reliably produce patterns with continuous lines using only one layer compared to the 10 or 20 layers required in previous work [41], Figure 69(b). Some overspray on the side of the deposited lines can be observed; however, it is limited in comparison with the initial conditions. For the pattern in Figure 69(b), the average width of the lines is about 20 µm. This optimized deposition has been obtained with the following parameters:

Table 14: LAMM process parameters for the deposition of Ag nanoparticles on Mg-2wt.%Ca substrate (cross-line pattern in Figure 69(b)).

Parameter	Value
Atomizer gas flow rate ($cm^3.min^{-1}$)	20
Sheath gas flow rate ($cm^3.min^{-1}$)	48
Ultrasonic atomizer voltage (V)	50
Deposition velocity ($mm.s^{-1}$)	0.7
Deposition tip diameter (µm)	150
Hot plate temperature (°C)	80

After deposition of the silver nanoparticles on the surface, a local heat treatment has been employed on the samples. Thermal treatment has been achieved by scanning the surface with a moving laser source. The laser power has been set to 8 W. An offset of 2 mm was applied to the height of the laser allowing a spot size of approximatively 85 µm. The spatial distribution of the intensity of the laser beam, having a Gaussian shape on the substrate, the pattern for the laser path has been set-up to obtain 25 % overlapping. Before laser sintering, it is possible to distinguish nanoparticles on the deposited line, Figure 70. These nanoparticles form a layer of distinct particles.

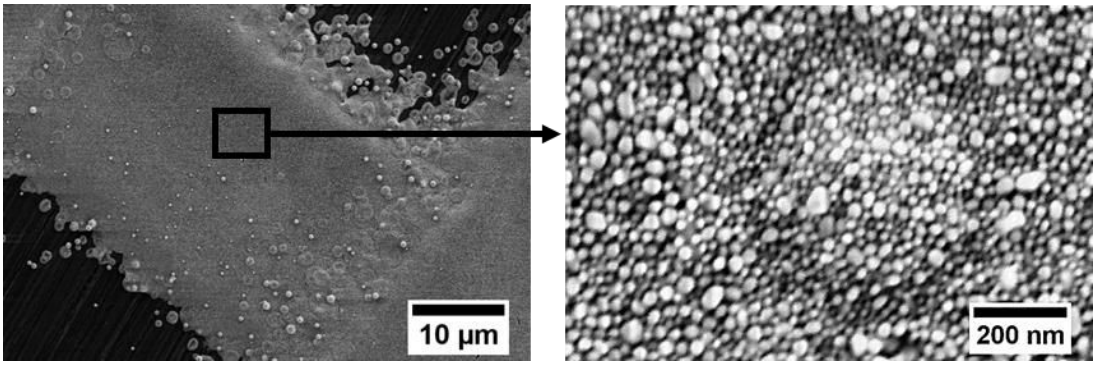

Figure 70: SEM images of deposited lines of silver nanoparticles without laser sintering (low and high magnification).

In the present work, our interest is oriented towards the sintering kinetics (evolution of the density with time) rather than on the fundamentals sintering mechanisms. A simple mechanism showing the necking process is represented in Figure 71. At the beginning, a layer of solvent wets the nanoparticles and prevents their interaction. In a first step, the laser beam evaporates the solvent. Then, in a second step, interconnections can be formed between nanoparticles. These interconnections

produce necking between the particles. If heating treatment continues, interconnections can grow to form agglomeration of nanoparticles and even lead to silver melting [24].

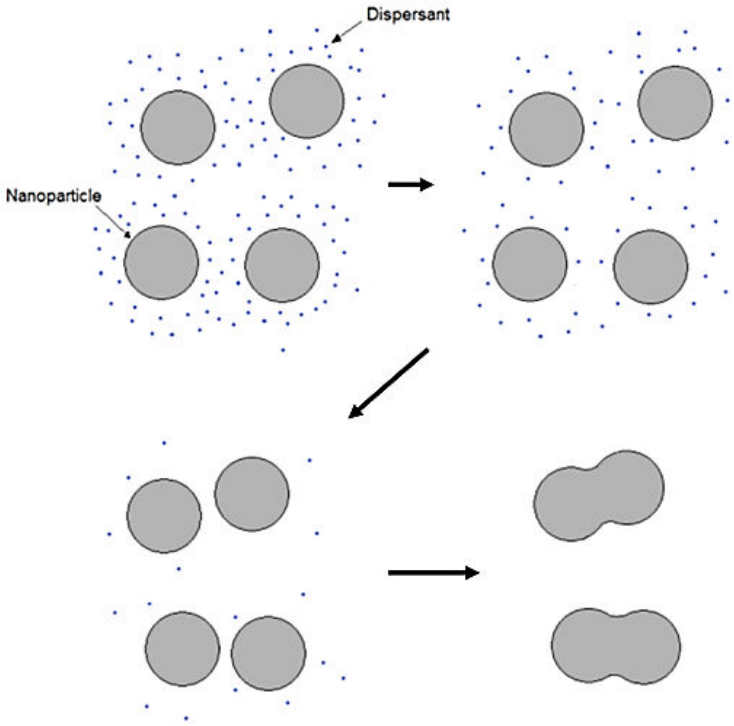

Figure 71: Laser sintering mechanism of nanoparticles. Adapted from [24].

An important parameter for sintering process is the laser beam power. As described above, by sintering, interconnection between nanoparticles appeared. It is then possible to detect if sintering has occurred by SEM images. After a series of trial and error, 8 W power has been determined as sufficient to produce silver nanoparticles sintering, Figure 72.

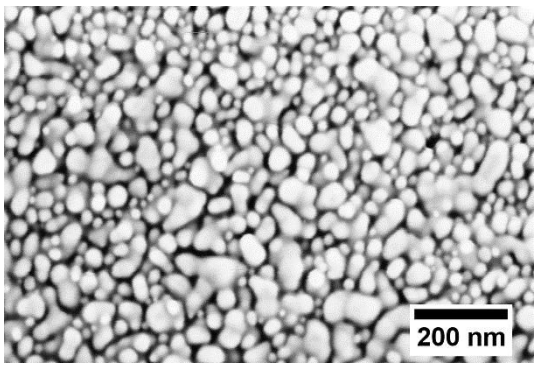

Figure 72: SEM micrograph of silver nanoparticles deposition after laser sintering with 8 W power, 0.3 mm.s^{-1} laser velocity and 85 µm laser beam spot size.

5.4 Patterning characterization

In the previous step, it has been determined the deposition parameters to obtain a pattern of continuous lines and to achieve an appropriate sintering. After these parameters were determined, patterning on a large scale has been performed. Profilometry has been done to characterize the regularity of the deposition on large scale (mm). Further investigations have been carried out to examine the impact of laser beam velocity parameter on sintering. These investigations have been carried out on cross sections by SEM and TEM.

5.4.1 Profilometry

The profilometry result of the test carried out on a cross-line pattern is shown Figure 73. According to the colour scale used for the z dimension, the pattern thickness is homogeneous over the whole deposition. The deposition thickness is about 1 µm for a single line, and about 2 µm at lines intersection. The 20 µm width previously measured by SEM images on a cross-line pattern deposition is verified on a larger scale. One can also note the rather smooth surface of the substrate.

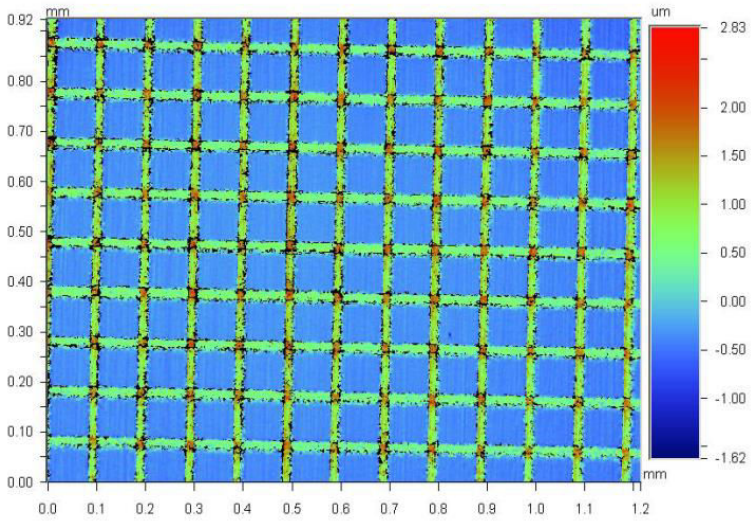

Figure 73: Profilometry observation of a patterned sample.

For comparison, profilometry measurement has been done on another sample, Figure 74. These two patterns have been obtained using the same parameters for the deposition; only the pattern geometry has been modified. As for the previous sample, the general view shows a homogeneous deposition. However, by taking a closer look at the patterned area, one can note that the thickness of the deposition is ranging between hundreds of nanometres to micrometres. Compared to Figure 73, it can also be noted that the lines intersection seems thinner (less than the previous 2 µm). Thus, if the deposition looks homogeneous on a large scale for a deposition, the thickness of the deposition may be slightly variable from one deposition to another. The thickness of the deposition is also variable along its width.

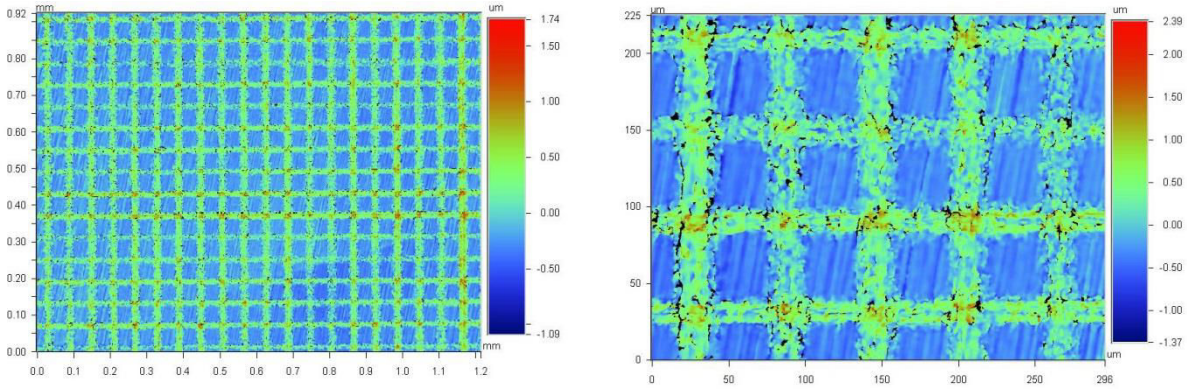

(a) (b)

Figure 74: (a) Profilometry observation of a patterned sample and (b) a zoom on a patterned area.

5.4.2 Heat treatment impact

The power of the laser has been fixed to 8 W, thus an important parameter for sintering is laser beam velocity. Indeed, for the same laser settings, a lower velocity increases the interaction time. In order to investigate the impact of velocity on sintering process, complete sintering of patterned samples has been obtained for various scanning rates, Table 15.

Table 15: Laser processing parameters.

Parameter	Value
Laser average power (W)	8
Laser scanning speed ($mm.s^{-1}$)	0.1 – 0.7
Laser average beam size (µm)	85

SEM images with the secondary electron contrast were realized to investigate the sintering progress. Figure 75 displays the SEM micrographs of the surface of the deposition after sintering at 0.1 $mm.s^{-1}$ and 0.7 $mm.s^{-1}$. On both micrographs, necking and even agglomeration of few nanoparticles of silver can be observed. The general topography looks rather similar for both conditions.

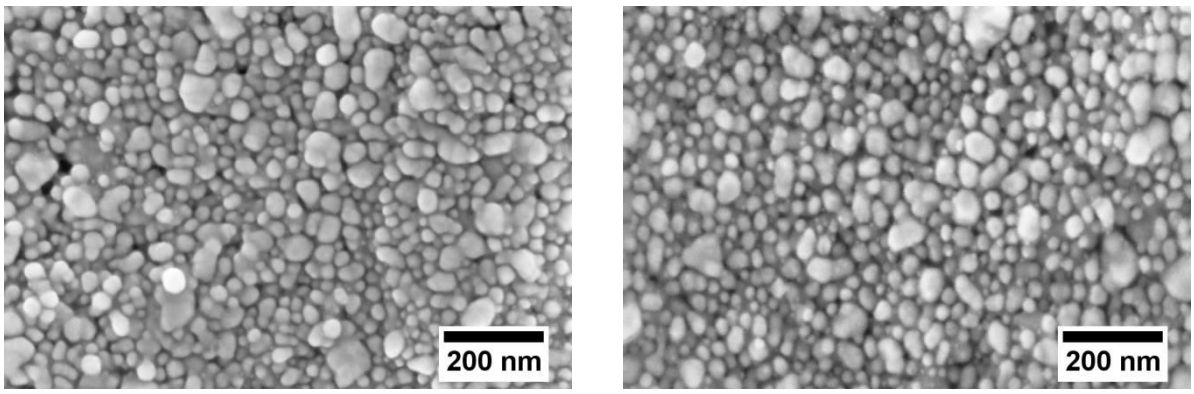

(a) (b)

Figure 75: SEM images of deposited lines of silver nanoparticles after laser sintering with 8 W power and different velocity: (a) 0.1 mm.s^{-1} and (b) 0.7 mm.s^{-1}.

To complete the characterization of the deposition, a cross section of the patterned sample has been made by FIB cutting and further examined by SEM. Figure 76 (a) shows the location of the cross section taken by FIB cutting and Figure 76 (b) shows an associated high magnification SEM image of the FIB section. One can note the presence of interfaces defaults. According to slice and view imaging realized during the FIB cutting, the non-cohesive areas at interface are not due to sample preparation.

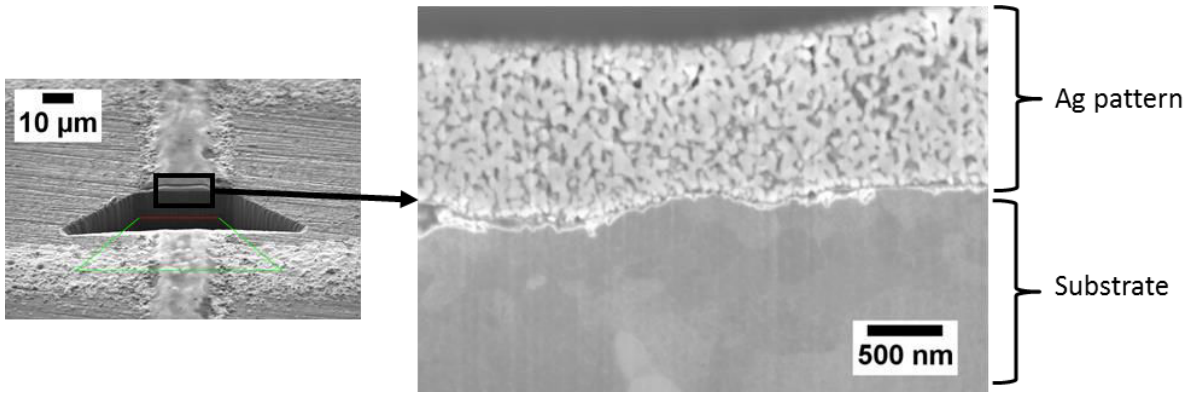

(a) (b)

Figure 76: (a) FIB section area and (b) SEM image of a cross section of a heat treated depositions of nanosilver particles with 8 W power, 85 µm spot size and 0.1 mm.s^{-1} laser beam velocity.

A comparison of the deposition quality, by cross sections, for different laser beam velocity (0.1 mm.s^{-1} and 0.7 mm.s^{-1}) is displayed in Figure 77. In both condition, the deposited layer presents a homogeneous evolution of its morphology through the thickness. Sintered nanoparticles create porous interconnected structures. Following

the different stages proposed in the previous simple sintering mechanism, usually a densification occurs during heat treatment [186].

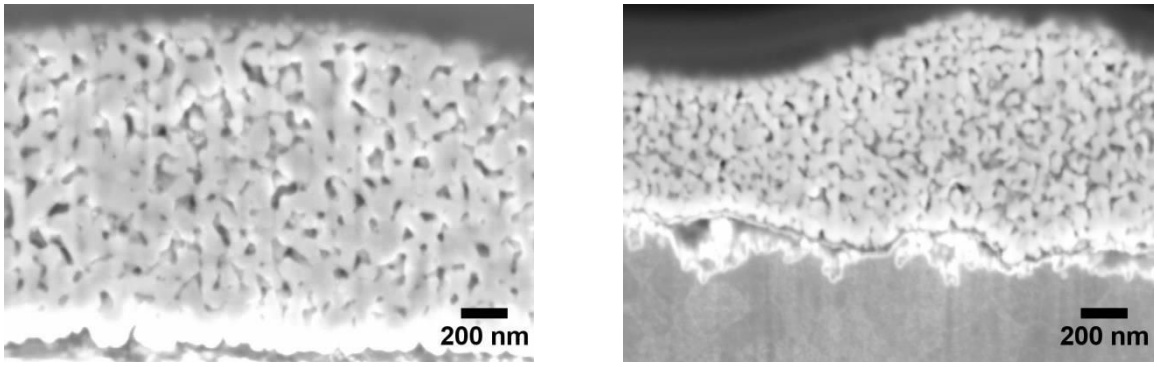

(a) (b)

Figure 77: SEM micrographs of a cross section of sintered deposition of silver nanoparticles with 8 W power, 85 µm spot size and (a) 0.1 $mm.s^{-1}$, (b) 0.7 $mm.s^{-1}$.

Different measurements have been realized using ImageJ on SEM micrographs for both conditions, Table 16. The average porosities of a heat treated deposition are 31 % and 34 % for a laser velocity of 0.1 $mm.s^{-1}$ and 0.7 $mm.s^{-1}$ respectively. As for a random packing of spheres, the theoretical porosity is approximately 38 % [42], the densification obtained during the heat treatment appears as low. The microporous structure has previously been reported after sintering of silver nanoparticles, [43] [44]. The possibility to decrease the amount of porosity of a heat treated silver nanoparticle deposition by increase the heating time has also been reported [45].

The average pore size has been determined by image analysis for both laser beam velocity condition, Table 16. Densification during sintering process may be impacted by different parameters. Particles size and morphology as well as the initial porosity will have an impact on the densification process [46]. During the first steps of necking, large particles will grow at the expense of the smaller contacting particles [46]. These agglomerations of nanoparticles participate in the formation of large pores in the structure. It has been reported that such agglomeration may slow down severely the subsequent densification process [46].

Before heat treatment, the deposition is composed of particles sizes ranging 30 nm to 60 nm. By image analysis, it has been determined the average size of silver arms after heat treatment: 81 nm and 48 nm for respectively a laser velocity of 0.1 $mm.s^{-1}$ and 0.7 $mm.s^{-1}$. Thus, agglomerations of few particles may be created. With a longer

interaction time, the agglomeration is more advanced as the average size increases. This phenomenon is corroborated by the average pore size measured on the cross section. Particles agglomeration involves an increase of the distance between the silver arms, which implies that the pores size increases. Thus, with the present heating times, it is estimated that the beginning of sintering has been achieved. However, the densification process has not occurred completely (up to a dense deposition). This is in accordance with the short interaction time by the laser heat treatment.

Table 16: The results of the image analysis of the heat treated surfaces.

Image analysis	Laser velocity at 0.1 $mm.s^{-1}$	Laser velocity at 0.7 $mm.s^{-1}$
Average porosity	31 %	34 %
Average pore size	46 nm	28 nm
Average silver arms size	81 nm	48 nm

5.4.3 Deposit/substrate interface

In the following section, the results of the characterization of the deposit/substrate interface are reported.

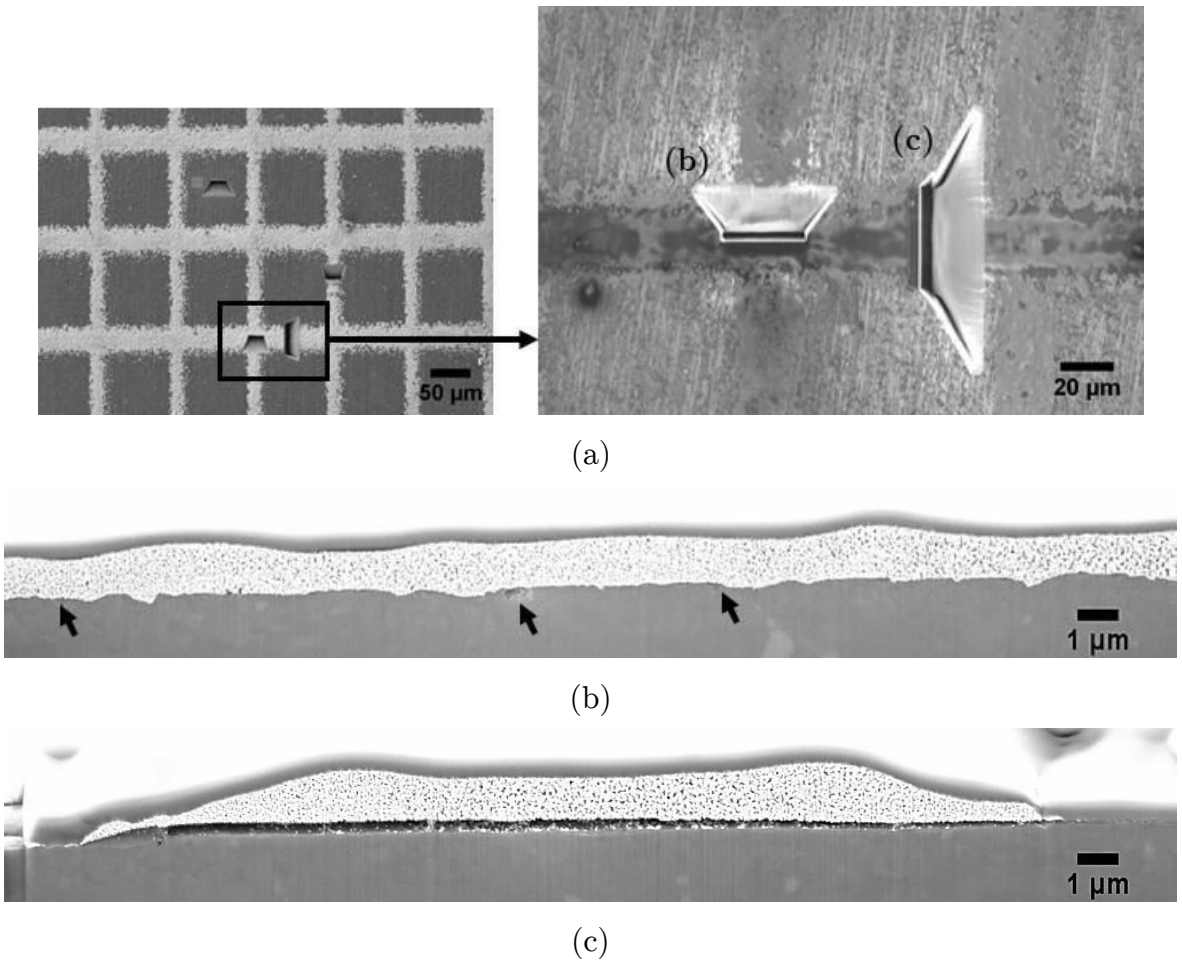

Figure 78: (a) SEM image of the location of FIB sections and the associated cross sections of sintered deposition of silver nanoparticles with 8 W power, 85 µm spot size and 0.1 mm.s^{-1}: (b) intersection of 2 lines and (c) transverse direction to a deposited.

Figure 78 shows two cross sections of sintered silver nanoparticle deposits. In Figure 78 (b), the deposition follows the topography of the substrate: the grooves from polishing are filled of deposition. Thus except for local points shown by arrows, on this image the deposition has a good contact with the substrate. However, the deposition shown in Figure 78 (c) does not have a bond with the substrate. A gap of around 400 nm is in-between the substrate and the deposition.

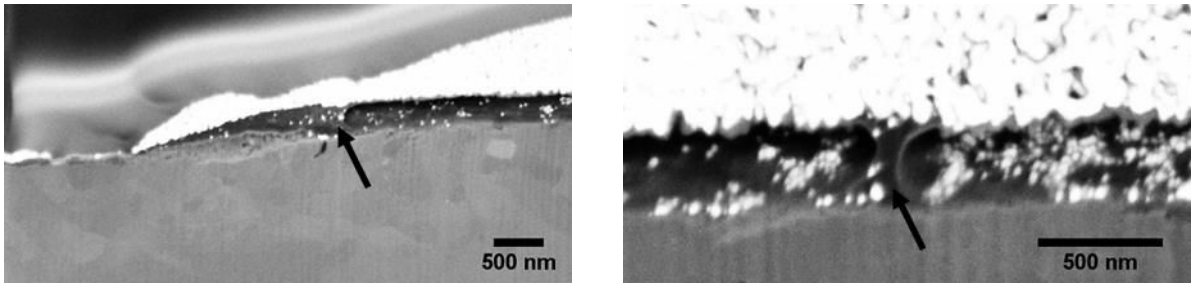

(a) (b)

Figure 79: Z-contrast SEM images of a cross section of a sintered silver deposit.

Figure 79 shows an SEM image of a cross section of sintered silver nanoparticles deposition with Z-constrast. The bright area represents silver deposition and medium grey represents the magnesium substrate. In between there is an area not bounded to the substrate. The microstructural details pointed by black arrows shows curving shapes. These details suggest the evaporation of a liquid or viscous element in this area. A possible origin may be the presence of the mixture of ethylene glycol/water used as solvent in the deposited ink. This is also supported by the dark or light grey contrast consistent with the organic compound.

5.4.4 Sublayer

On the SEM cross section image, Figure 80, three areas can be distinguished. At the top, there is the previously described deposition with its partially cohesive interface. Under the deposition there is a sublayer of substrate with a fine grain size microstructure. This sublayer is located near the surface of the sample and is also present at areas without deposition (Figure 80). This sublayer has a thickness of approximately 1 µm and contains magnesium grains with sizes ranging from about 100 nm to 1 µm. At the bottom, there is the substrate with the microstructure obtained by thermomechanical treatment: grain size of 8 µm and second phase fragments or particles (sample extruded at 400 °C, see Section 3.5.1).

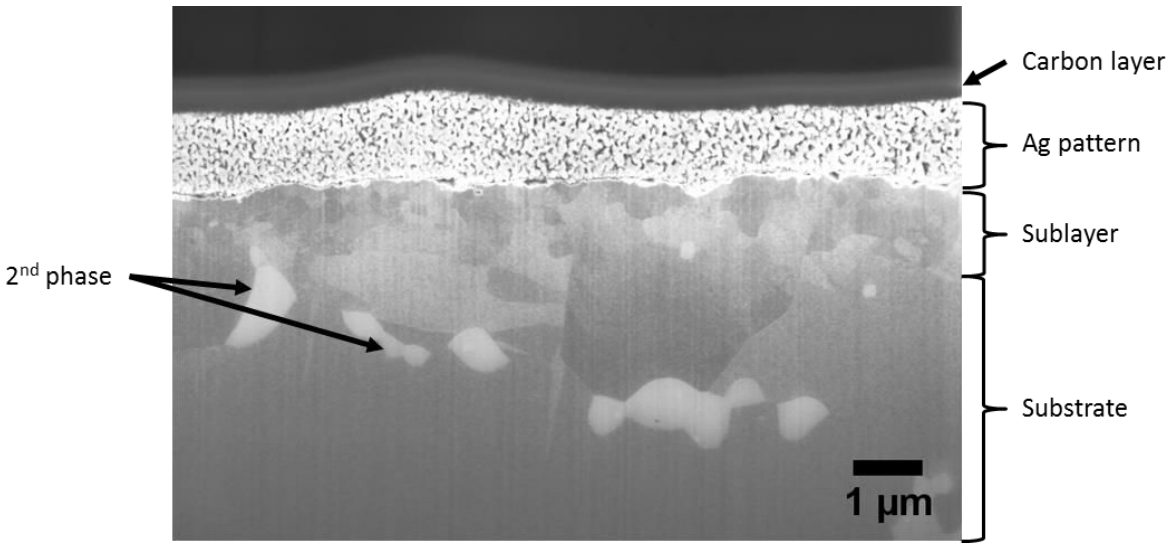

Figure 80: SEM image of a cross section of a sintered surface deposition obtained using a laser beam with 8 W power, 85 µm spot size and 0.1 mm.s^{-1} beam velocity.

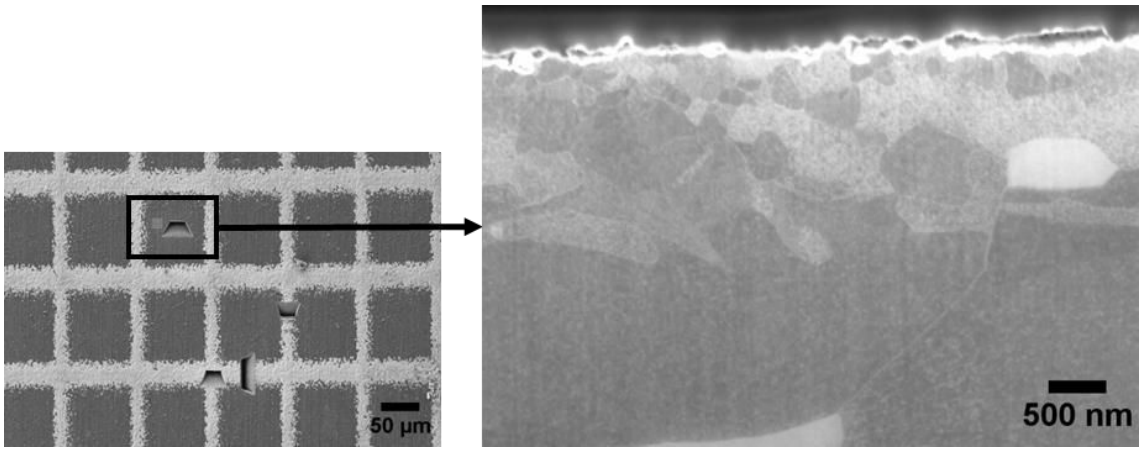

(a) (b)

Figure 81: (a) Location of the FIB cross sections and (b) SEM image of a cross section of a laser treated sample extruded at 400 °C obtained using a laser beam with 8 W power, 85 µm spot size and 0.1 mm.s^{-1} beam velocity.

This sublayer reveals the existence of a laser affected zone which seems to have a limited thickness. However, this sublayer seems to have the same characteristics under silver nanoparticles deposition or in non-covered areas. Thus, the thermal treatment induced by the laser should be approximately the same in both areas.

Further investigations of this sublayer have been carried out by TEM on a thin section. In Figure 82 (a) a global view for location of the investigated area is displayed. The ACOM crystallographic mapping and its associated bright field numeric are displayed in Figure 82 (b) and (c), respectively. Observation of the ACOM mapping reveals the smallest magnesium grains (≈ 100 nm) are in the vicinity

of the surface. The size of the grains gradually increases in this sublayer and there is a clear separation between the coarser microstructure of the substrate. The ACOM crystallographic mapping did not reveal any preferential crystallographic orientation.

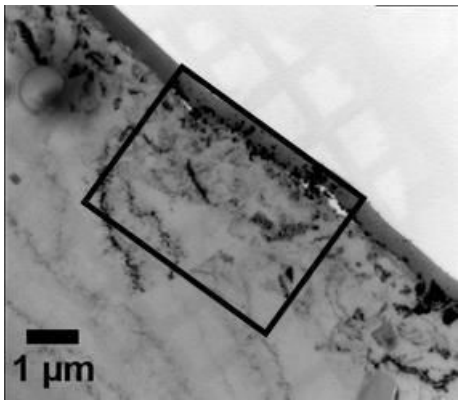

(a)

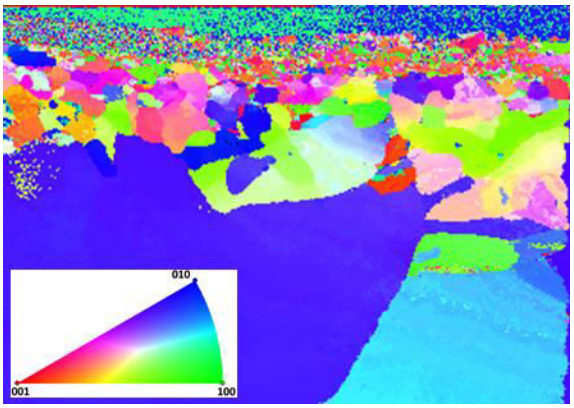

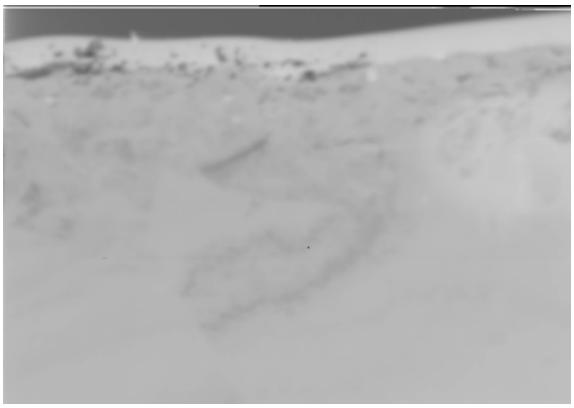

(b) (c)

Figure 82: (a) A TEM image of the investigated area; (b) ACOM mapping of the substrate sublayer indexed on magnesium and (c) the associated bright field.

The microstructural observations of this sample in Section 3.5.1 reveal a recrystallized microstructure with 8 µm grain size. The mechanical properties study on this sample has shown good ductility. Thus, the density of dislocation should be low which lead to low driving forces for recrystallization. Thus, this fine grains sublayer is unlikely to happen by heat treatment.

The preparation of the substrate for deposition implies a mechanical polishing to 4000 grit. The equivalent particles size on these polishing disks is approximately 4 µm. Thus it can be expected a roughness of 2 µm on the surface of the substrate. However, based on the previous observations done by profilometry or SEM on cross section the roughness of the material is very low: around 0.2 µm. Thus, during the polishing, plastic deformation at the vicinity of the surface may have occurred. The

presence of twins in the vicinity of the surface is in accordance with this phenomenon, Figure 83. Also, in the course of the TEM characterization of samples prepared by mechanical polishing and ion milling, it has been noticed a high density of dislocations due to the mechanical polishing process. Indeed, the sample studied is very soft due to the very low solubility of calcium in magnesium, and structural defects are common during mechanical polishing steps [187].

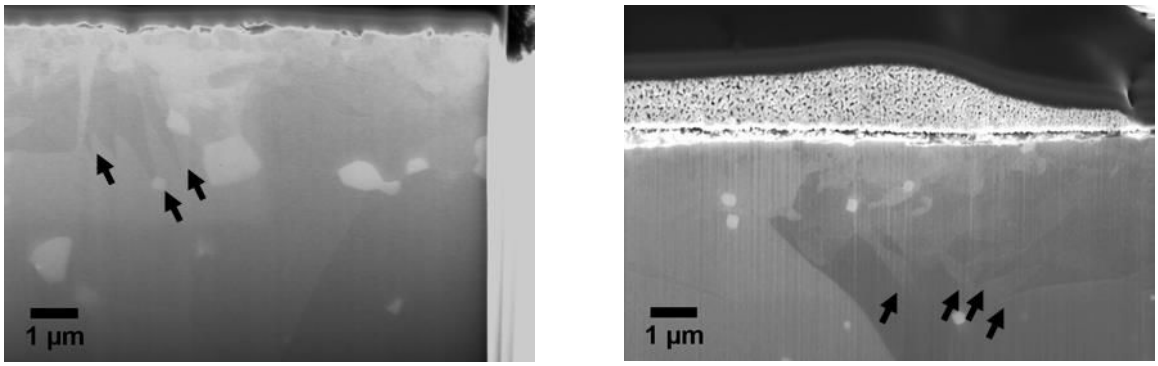

(a) (b)

Figure 83: SEM image of a cross section of a laser treated sample extruded at 400 °C with 8 W power, 85 µm spot size and 0.1 mm.s^{-1} laser beam velocity; twins pointed by arrows.

In conclusion, a work hardened sublayer may have been created during the polishing stage of samples preparation. The laser treatment for deposition sintering may have then created the recrystallization of this sublayer.

5.5 Thermal effect study by finite element simulation

In the previous section, the process for surface functionalization has been described. In this process, firstly, there is deposition of silver nanoparticles on the substrates using an additive manufacturing technology; and in a second time, sintering of the deposited layer is done by a laser treatment. The cross section observations have permitted to characterize the sintering quality. The deposition presents a porous microstructure with no bounding to the substrate at some points. These observations have been realized on two different conditions of sintering with only a variation of the laser beam velocity: 0.1 mm.s^{-1} and 0.7 mm.s^{-1}. Other parameters might also help to improve the sintering of the deposition like the laser power or the spot size.

Another point to take in account is that the functionalization process has been carried out for a chosen substrate and defined deposition characteristics (topography of the deposition and specific nanoparticles ink). However, depending on the final requirements of the application, these parameters may vary. Using a finite element modelling, it is possible to simulate the thermal evolution of the substrate and deposition due to the sintering laser treatment for selected parameters. Such model would provide a basis to investigate the impact of different input parameters. This may be used for further optimization of the functionalization process.

Owing to the "heat transfer in solids" module of COMSOL Multiphysics software, it is possible to simulate thermal effects for the system "sample holder / sample / Ag deposition". Specific thermo-physical properties have to be used to take in account the composition of the alloy and the porous nature of the deposition. The existing literature on laser interactions with solids [47] provides the basis to model the different thermal interactions with the help of specific references toward sintering of silver nanoparticles [48] [49]. Then, the model can be run with the different parameters and thermal information can be retrieved from the results. The previous section on microstructural characterization gave information on the sintering impact: quality of the sintered deposition and presence of a sublayer of fine grains at the surface of the substrate indicating a thermally affected zone. The validity of the simulation will be discussed with respect to this information.

5.5.1 Thermal model

Modelling the thermal evolution during laser treatment requires taking into account the system "sample holder / sample / Ag deposition", as shown in Figure 84 (a). The sample holder and sample sizes are represented at a 1:1 scale in the model. As shown in Figure 84 (b), the path of the laser follows a straight line between point "a" and point "c". This laser beam power input, considered as a power supply associated with the substrate and the silver deposition, is applied as a boundary condition. At the beginning, between points "a" and "b" the laser is above an area of the substrate without silver deposition. This domain allows reaching a stable thermal state. Between points "b" and "c" there is an area of the substrate with silver deposition in its centre. The deposition is modelled by a domain of 200 µm length, 20 µm width

and 1 µm thick. The length of the deposition has been intentionally reduced to diminish greatly the total number of elements after meshing. The modelling results obtained in these domains will be used to evaluate the thermal impact of the sintering process on the substrate and on the silver deposition.

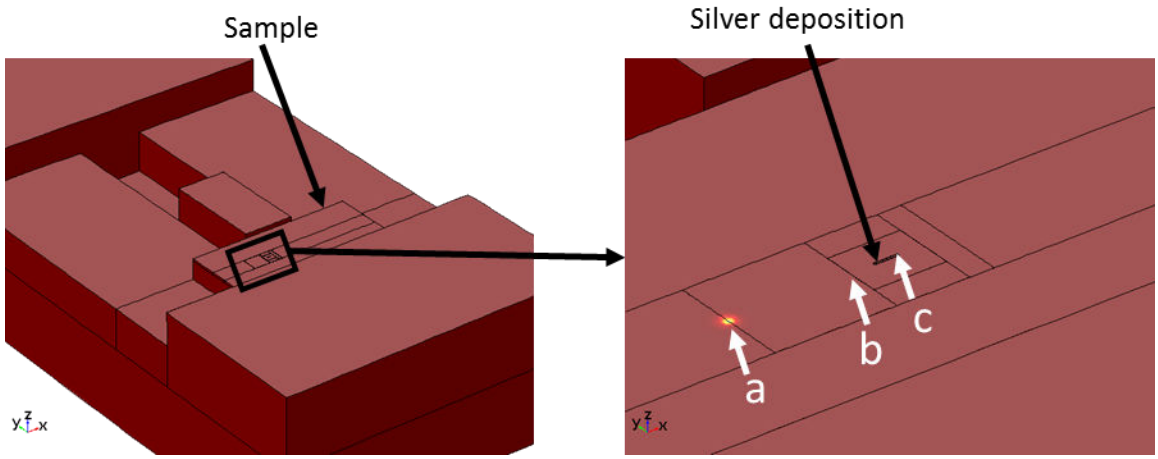

(a) (b)

Figure 84: (a) Three-dimensional representation of the system "sample holder / sample / Ag deposition" and (b) a focus on the simulated laser path: straight line between point "a" and point "b".

The meshing of these surfaces is of importance to apply the correct input of energy per elements. Indeed, a fluctuation in the impact of the thermal effect can happen for coarse meshing. Thus, the meshing of these surfaces needs to be fine enough to properly simulate the thermal flux at the investigated scale. For the deposition, the maximum element size is limited by the thickness of the deposition. Thus the maximum size of the elements for this domain is 1 µm which is fine enough for the present study.

Concerning the top surface of the sample, it has been chosen to incorporate smaller domains in order to reduce progressively the element size at the processing area. Thus, the model has been run with different meshing sizes for this area and the associated maximum surface temperature retrieved. By decreasing the meshing, there is an increase in the maximum temperature due to the refinement of the local energy input. This increase of temperature rises up to a maximum when the effect of the meshing becomes negligible. Thereafter, the associated mesh size of maximum 20 µm has been used.

Figure 85 shows the different mesh geometry of the model. The total number of domain elements is around 250 000 after meshing optimization.

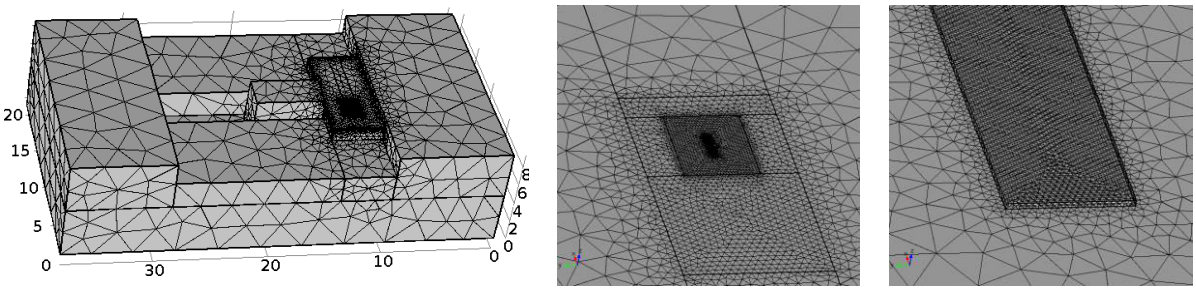

(a) (b) (c)

Figure 85: Mesh plots of the model: (a) global view, (b) a zoom around the deposition and (c) a zoom on the front of the deposition.

Under the "heat transfer in solids" module in COMSOL Multiphysics, the following equation is considered for governing heat transfer for an immobile solid:

$$\rho C_p \frac{\partial T}{\partial t} + \nabla \cdot (-k\nabla T) = Q \qquad (9)$$

where ρ, C_p, k and Q are respectively, the density, the specific heat capacity, thermal conductivity and the power generation per unit volume for each domain considered.

Boundary conditions

In order to solve the heat equation, boundary conditions need to be defined. In the present case, different boundary conditions are applied based on their location. According to the experimental work, the temperature is low (below the Mg-Mg_2Ca eutectic point), thus the radiation are considered as negligible. Therefore, four different boundary conditions need to be used to describe the thermal transfer:

- convective heat transfer
- thermal contact
- moving power input
- constant temperature

Convective heat transfer

All the surfaces, except the surfaces with contact and the bottom of the sample holder, are subjected to convective heat transfer. In these cases, the boundary condition is given by:

$$-k\nabla Tn = -h_s(T_{ext} - T) \qquad (10)$$

where n is the vector normal to the surface boundary and h_s the convective heat transfer coefficient associated to the surface.

Thermal contact

The sample holder helps to maintain the sample during the sintering process. Thus, there is contact between the sample and the sample holder at some areas. The surfaces in contact are designated by the black arrows in Figure 86.

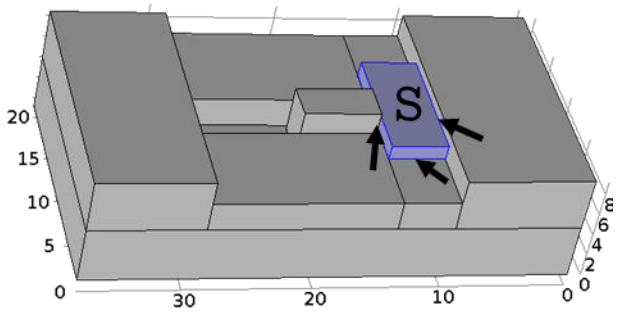

Figure 86: Sample (S) mounted on the holder: surfaces with thermal contact are pointed by black arrows.

In these cases, the boundary condition is given by:

$$-k\nabla Tn = -h_c(T_2 - T) \qquad (11)$$

where h_c is the joint conductance which takes into account two contributions: the contact spots conductance and the gap conductance due to the roughness. In the present case, samples were polished to 4000 grit. From cross section characterizations, it has been estimated that the surface roughness (defined here by an asperities average height) was less than 0.2 µm.

Moving power input

The top surface of the substrate and the silver deposition are subjected to the laser beam power input. The top surface of the sample is considered as plane and the average deposition thickness is 1 µm. It is assumed that z dimension is small enough that the intensity of the laser can be considered as constant along z. Thus, the moving power input is given by:

$$q = \beta_M I(x, y, t) \tag{12}$$

where β_M is the absorption coefficient of the considered material (substrate or silver deposition). Details on the absorption coefficients of the present materials will be given further in this section.

The laser used in the present work laser is characterized by a TEM_{00} transverse mode. Thus, the intensity of distribution is characterized by:

$$I(x, y, t) = \frac{2P_l M^2}{\pi r_l^2} exp\left(\frac{-2r^2 M^2}{r_l^2}\right) \tag{13}$$

where P_l is the laser power, M^2 is the beam factor quality, r_l the spot size at the process zone and r the distance from the centre of the spot size. The laser has a spot size of 85 µm at the process zone and in Cartesian coordinates, r can be written as follow:

$$r = \sqrt{(x - v_l t - x_0)^2 + (y - y_0)^2} \tag{14}$$

where (x_0, y_0) is the Cartesian coordinates of the centre of laser beam at $t = 0$ and v_l is the laser beam velocity.

Constant temperature

The bottom surface of the sample holder is in contact with the stage of the machine. Due to the large size of the stage the bottom surface of the sample holder will be considered to be at a constant temperature (ambient temperature).

Materials properties

As seen above in the equations, several material properties values are needed to perform the simulation. These material parameters describe the thermo-physical properties and absorbance of materials. Using the existing literature, the most

appropriate values will be considered. However, based on the experimental observations, the expected temperature increase is small (below Mg-Mg_2Ca eutectic point) for both materials. Therefore, the effect of temperature on properties will be assumed as negligible.

Mg-2wt.%Ca substrate

Concerning the heat capacity at constant pressure and the thermal conductivity of the sample, they are dependent of the composition of the alloy. Pan et al. [188] have reported the evolution of thermal and electrical conductivity of binary magnesium alloys, included Mg-Ca alloys. Thus in the present model, the thermo-physical properties of Mg-1.4wt.%Ca reported by Pan et al. [188] will be used, Table 17.

In the literature, absorbance of magnesium and magnesium alloys for the infrared region around 1550 nm has been reported in the range of 0.1 to 0.23 [189] [190]. Magnesium alloys are usually covered by a thin layer of oxide (MgO) due to their reactivity with oxygen. It has been reported that MgO on the surface of magnesium alloys would be transparent in the infrared (0.7 – 3.0 µm) region [191]. Thus, the impact of oxide layer on the absorbance may be considered as negligible. Substrate preparation includes polishing to 4000 grit and profilometric measurements have been done on polished samples. The measured RMS roughness for polished samples is approximately 0.2 µm which is at the same order as the laser beam wavelength. Thus, the roughness should not impact the absorbance of the substrate. Table 17 displays a summary of the thermo-physical properties used in the model for the substrate.

Table 17: Thermo-physical properties of the substrate [188].

Property	Value
Heat capacity at constant pressure	1008 $J.Kg^{-1}.K^{-1}$
Thermal conductivity	122 $W.m^{-1}.K^{-1}$
Density	1736 $Kg.m^{-3}$
Absorbance	0.1 – 0.23

Silver deposition

The thermo-physical properties of bulk silver are displayed in Table 18. In the present work, the deposition can be described as a porous material made of a packing

of silver nanoparticles. Thus, estimation of the thermo-physical properties has been done using this simplified description.

Table 18: Thermo-physical properties of silver as a bulk material [189] [192].

Property	Value
Heat capacity at constant pressure	244 $J.Kg^{-1}.K^{-1}$
Thermal conductivity	428 $W.m^{-1}.K^{-1}$
Density	10500 $Kg.m^{-3}$
Absorbance	0.021

The density of the material can be adjusted according to the amount of porosity contained in the layer at the initial state. The porosity for a random packing of spheres is approximately 38 % [42]. Thus, the density of the deposition is considered equal to 6563 $Kg.m^{-3}$.

To calculate the thermal conductivity, the initial porosities of deposition should be taken into account as porosities have an impact on the thermal flux inside the deposition. For this calculation of the equivalent thermal conductivity, the deposition will be considered as a porous material with spherical porosities. Using this assumption, the thermal conductivity can be calculated as follows [193]:

$$k_p = k_s(1-\varphi)^{3/2} \qquad (15)$$

where k_s and φ are, respectively, the thermal conductivity of the solid material and the ratio of porosities. Under these assumptions, the thermo-physical properties used for the silver deposition are displayed in Table 19.

To verify if the roughness of the deposition may have an impact on the absorbance the root mean square (RMS) roughness has to be determined. Indeed, if the RMS roughness is several orders of magnitude under the wavelength of the laser beam the absorption is enhanced [194]. According to the manufacturer, the silver nanoparticles is made of particles with an average size under 60 nm. According to image analysis, the size of the majority of particles ranges between 30 nm and 60nm. To account for this microstructure, the nanoparticles deposition is considered as an arrangement of spheres, Figure 87. Based on the measured size of nanoparticles, the root mean square (RMS) roughness would likely ranges between 30 nm and 60 nm. This range is

very small compared to the wavelength of the laser beam, thus, the absorbance of the deposition will be adjusted accordingly.

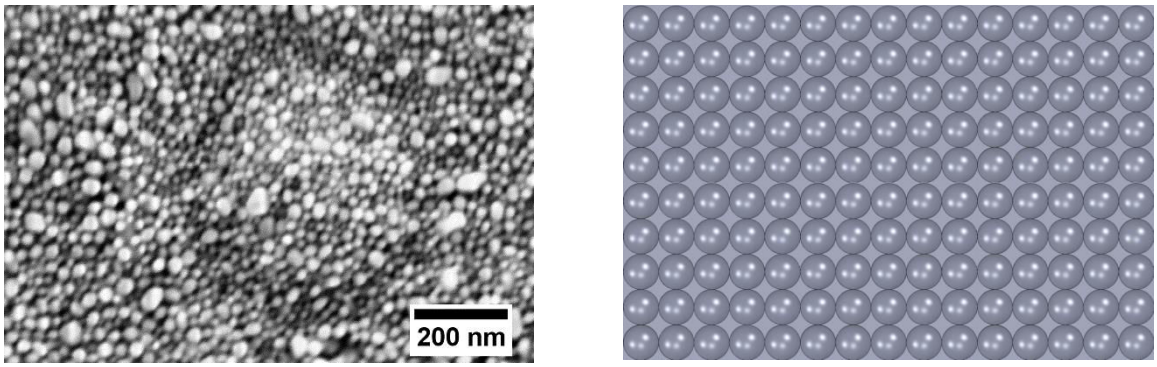

(a) (b)

Figure 87: (a) SEM micrographs of unsintered silver nanoparticles deposition and (b) assumed arrangement of the particles for roughness estimation [48].

The effective absorbance due to the roughness of the material can be determined using the following expression [195]:

$$A_r = 1 - (1 - A)e^{-\left(\frac{4\pi\delta}{\lambda}\right)^2} \qquad (16)$$

where A is the absorbance of the material, δ is the RMS roughness and λ is the wavelength of the incident beam. The calculated effective absorbance using the previous estimation of the RMS roughness, 30 nm to 60 nm, ranges between 0.08 and 0.23, respectively. It is worth noting that compared to the bulk property of silver, the roughness of the deposition significantly changes the absorbance. All the different properties of silver deposition are summarized in Table 19.

Table 19: Thermo-physical properties of the silver nanoparticles deposition.

Property	Value
Heat capacity at constant pressure	244 $J.kg^{-1}.K^{-1}$
Thermal conductivity	209 $W.m^{-1}.K^{-1}$
Density	6563 $Kg.m^{-3}$
Absorbance	0.08 – 0.23

5.5.2 Modelling

The boundary conditions and materials properties are then introduced in the previously described thermal model. At this stage, the absorbance of the substrate and the deposition could not be defined precisely but a possible range has been estimated for these values. Thus, in order to determine the appropriate absorbance values to describe the studied system, the following set of absorbance coefficients concerning the substrate, β_S, and the deposition, β_D, will be used in computation:

Table 20: Description of the sets of absorbance coefficients used for computation

		β_S		
		0.1	0.17	0.23
β_D	0.08	x	x	x
	0.1	x	x	x
	0.17	x	x	x
	0.23	x	x	x

The model has been run with the different parameters. It is then possible to evaluate the silver deposition temperature for each condition. Figure 88 displays the silver deposition temperature obtained for each set of absorbance coefficients (β_S, β_D) with a laser beam velocity of 0.1 mm.s^{-1}.

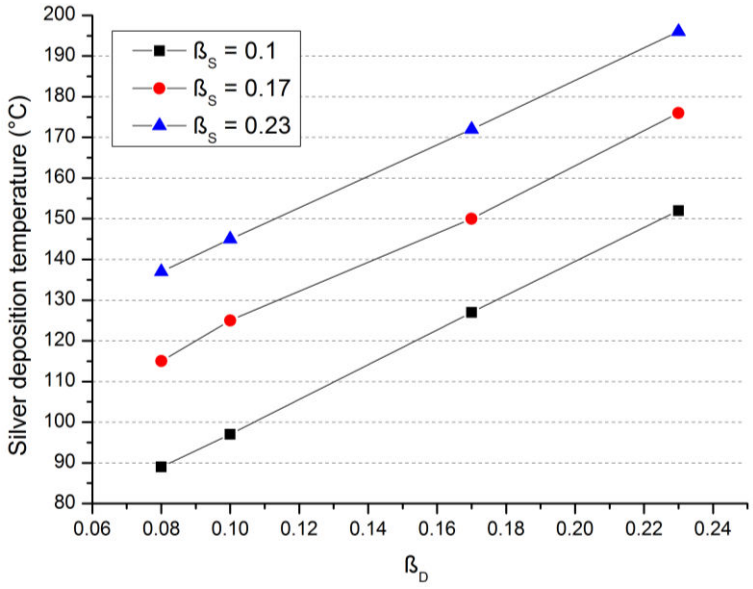

Figure 88: Maximum temperature in a silver deposition as function of the sets of absorbance coefficients (β_S, β_D) and with a laser beam velocity of 0.1 mm.s^{-1}.

Each line in Figure 88 represents the silver deposition temperature as a function of the absorbance of the silver deposition; the absorbance of the Mg-2wt.%Ca substrate is fixed. The predicted temperature values are found in a large range: from 90 °C to 195 °C. As expected, the higher are the absorbance coefficients; the higher is the resulting temperature in the silver deposition. However, an important effect of the absorbance of the substrate on the silver deposition temperature can be noted. An increment by 0.07 of the substrate absorbance increases the silver deposition by 20 °C. This large range of temperature needs to be compared with existing literature in order to determine whether or not they are consistent with our observations, i.e. sintering progress of the silver nanoparticles deposition.

Sintering of silver nanoparticles, with an average size between 24 nm to 40 nm, has previously been studied at 150 °C [45] [196]. Thus, it is considered that the sets of absorbance involving a minimum temperature of 150 °C during the laser treatment may be able to sinter the silver nanoparticles. Considering Figure 88, there are only five cases which have the maximum temperature in silver deposition equal or higher than 150 °C with a laser velocity of 0.1 mm.s^{-1}. These sets of absorbance coefficients are displayed in Table 21.

Table 21: Sets of absorbance coefficients allowing for a minimum of 150 °C for the deposition temperature

		β_S		
		0.1	0.17	0.23
β_D	0.17		x	x
	0.23	x	x	x

According to the microstructural characterization results, partial sintering has also occurred with a laser velocity of 0.7 mm.s^{-1}. Thus the maximum temperature obtained in the silver deposition for the two velocities: 0.1 mm.s^{-1} and 0.7 mm.s^{-1} can be compared, Figure 89.

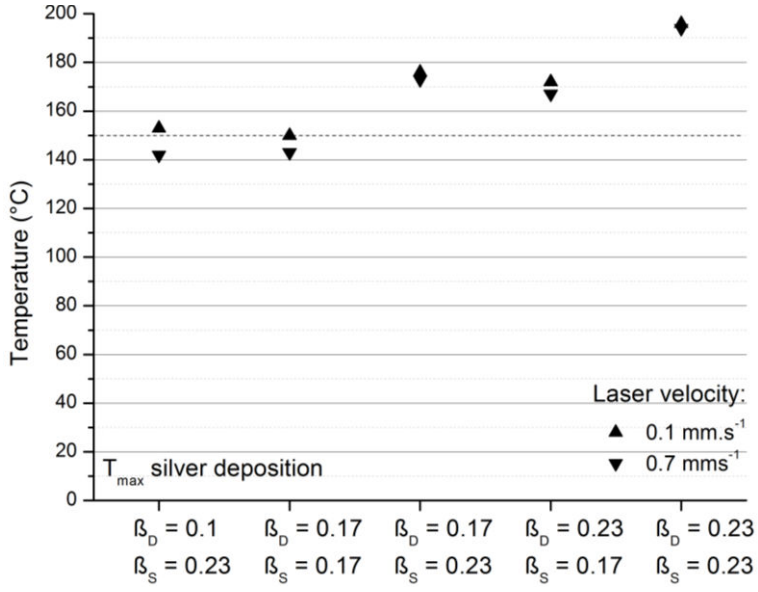

Figure 89: Maximum temperature obtained in silver deposition during heat treatment by laser at two different velocities: 0.1 mm.s^{-1} and 0.7 mm.s^{-1}.

From Figure 89 it is possible to note the low impact of the laser velocity on the maximum temperature obtained in the silver deposition. The relatively high thermal conductivity of the deposition may rapidly dissipate the heat. However, for two different sets of absorbance coefficients, $(\beta_S = 0.1; \beta_D = 0.23)$and $(\beta_S = 0.17; \beta_D\ 0.17)$ the maximum temperature of the deposition obtained during the heat treatment is lower than the previously reported 150 °C. Thus with these sets of absorbance coefficients a partial sintering is unlikely to happen. It is then possible to restrict the sets of absorbance coefficients, Table 22.

Table 22: Possible sets of absorbance coefficients allowing the characterized sintering quality.

		β_S	
		0.17	0.23
β_D	0.17		x
	0.23	x	x

In the microstructural characterizations, it has been noted different pore sizes for different velocities. The evolution of pore size results from the progress of the sintering: the agglomeration of nanoparticles creates larger pores with time before densification. Thus, these differences suggest a different interaction time of the laser on the silver deposition to allow the sintering process to progress. Using COMSOL, for a discrete location, it is possible to retrieve the temperature profile as a function of time. Figure 90 shows the temperature profile of a point at the top surface of the deposition for $(\beta_S = 0.23; \beta_D = 0.23)$ and different velocities: 0.1 mm.s^{-1} and 0.7 mm.s^{-1}.

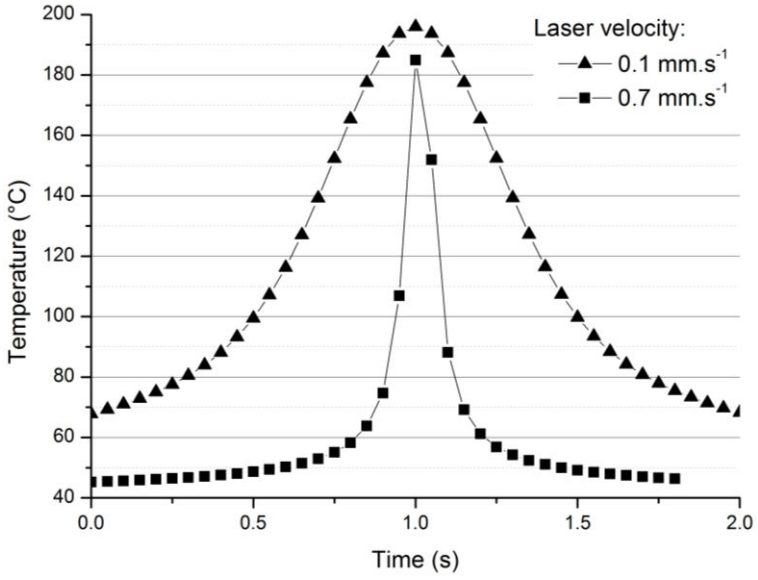

Figure 90: Temperature profile during sintering of a point on the top surface of the silver deposition with $(\beta_S = 0.23; \beta_D = 0.23)$ and for different velocities: 0.1 mm.s^{-1} and 0.7 mm.s^{-1}.

According to the simulation, using a 0.7 mm.s^{-1} laser velocity, the temperature in the deposition rises rapidly and decreases rapidly. By decreasing the laser velocity to 0.1 mm.s^{-1}, the predicted temperature profile shows a gradual increase up to the maximum temperature and the symmetrical decrease for the cooling part. As mentioned in the previous paragraph, these two temperature profiles would impact

the porosities of the deposition. These predictions can then be useful to optimise the microstructure of the deposition with respect to specific applications.

Using the predicted data of temperature from COMSOL, compared the evolution of temperature of the top and bottom surfaces of the silver deposition during the heat treatment have been compared. For instance, for the set $(\beta_S = 0.23; \beta_D = 0.23)$, Figure 91 shows that the maximum temperature of the bottom surface is only a few degrees below the maximum of the top surface. Thus, the heating rate can also be assumed to be the same at both locations. This is in accordance with the homogeneous sintering quality observed previously by cross section characterization.

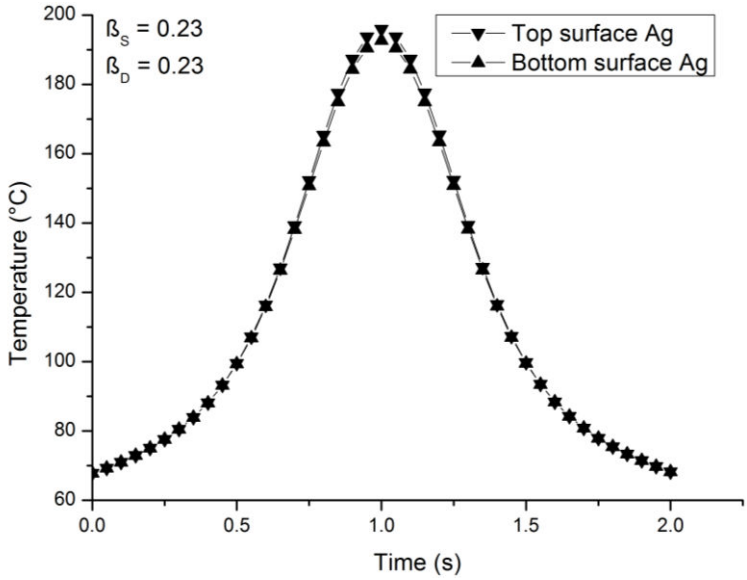

Figure 91: Temperature evolution during sintering of the top and bottom surfaces of silver deposition at the same (x,y) coordinates with $\beta_D = 0.23$, $\beta_S = 0.23$ and with a laser beam velocity of 0.1 mm.s^{-1}.

After comparison between simulation and microstructural information of the deposition, the possibilities for the set of absorbance values have been reduced to three, Table 22. Then other experimental information has been considered to further reduce this set.

As reported in the microstructural characterization section, the laser sintering treatment also affects the microstructure of the substrate. A sublayer of fine grains has been observed at the surface of the substrate. This sublayer has been observed under the deposition and outside the deposition. No obvious difference has been detected between these two conditions (zone below or outside the deposition layer).

Then, it is of interest to consider the predicted temperature gradient inside the substrate to obtain additional information, Figure 92.

$\beta_S = 0.17$ and $\beta_D = 0.23$

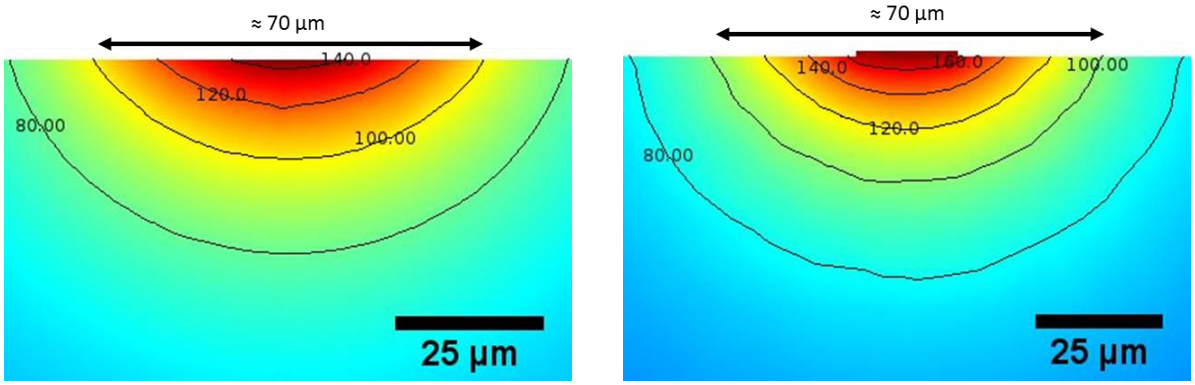

(a) (b)

$\beta_S = 0.23$ and $\beta_D = 0.17$

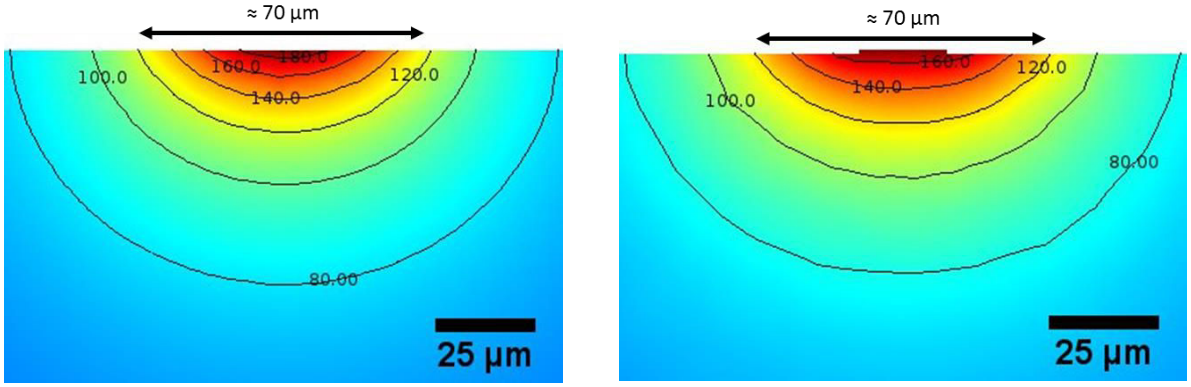

(c) (d)

$\beta_S = 0.23$ and $\beta_D = 0.23$

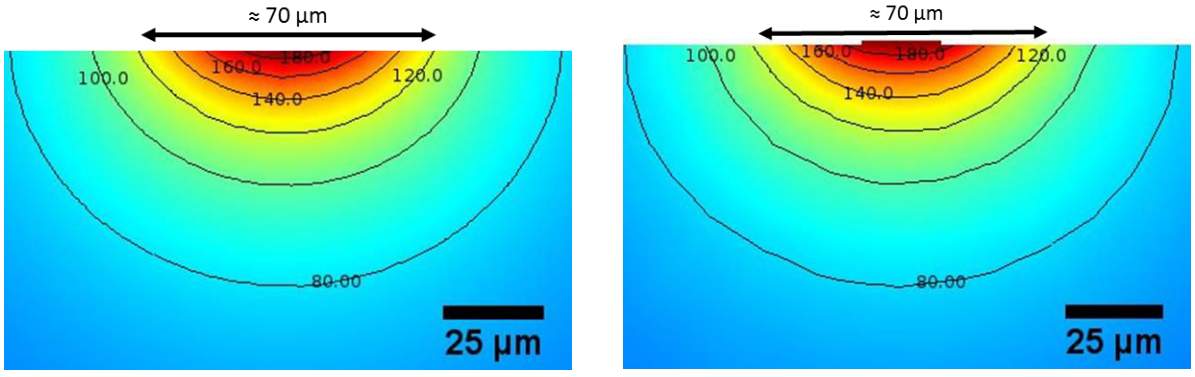

(e) (f)

Figure 92: Temperature profiles of substrate cross sections or silver deposition/substrate during sintering with a laser beam velocity of 0.1 mm.s^{-1} and for (a) and (b) $\beta_S = 0.17$, $\beta_D = 0.23$; for (c) and (d) $\beta_S = 0.23$, $\beta_D = 0.17$; (e) and (f) $\beta_S = 0.23$, $\beta_D = 0.23$.

In the laser treatment, an overlapping of the laser beam has been realized. The spot size at the process zone equals to 85 µm. However, the laser path lines are at a

distance of 70 µm from each other. The distance between lines is represented on each image in Figure 92. According to the simulation, the thermal impact of the laser sintering is not restricted to a band of 1 µm below the surface. High temperatures are reached at the first micrometre below the surface: from 100 °C to 180 °C. The temperature rapidly decreases with the thickness of the substrate. The microstructural evolution can occur only in the area with high driving forces for recrystallization. Therefore, the microstructural observations only give a low limit to the thickness of the thermally affected area below the surface of the substrate.

It has been reported that recrystallization could occur in pure magnesium between room temperature to 200 °C [197]. In the present alloy, calcium solubility is very low. Thus the sublayer presenting a fine microstructure: 100 nm to 600 nm, may be the result of recrystallization. This recrystallization would take place in a work hardened area resulting from the mechanical polishing (see Section 4.4.4).

5.5.3 *In situ* temperature measurement

For complementary experimental information, *in situ* temperature measurement has been performed. A thermocouple has been set up at the bottom of a sample and the laser process has been performed on the top surface, Figure 93.

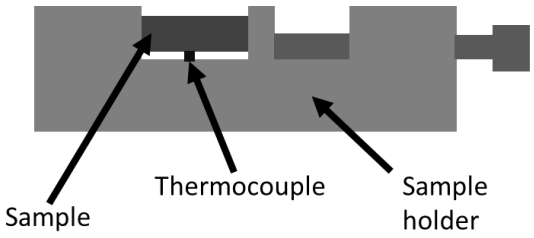

Figure 93: Schema of the *in situ* temperature measurement.

An average temperature of 85 °C has been measured when the laser beam processed the top sample surface. The thermal model has been adapted to this configuration by taking in account, an external convection without contact instead of a thermal contact on the bottom surface. This adapted model has been used to predict the bottom temperature of the sample for different substrate absorbance coefficient, Figure 94.

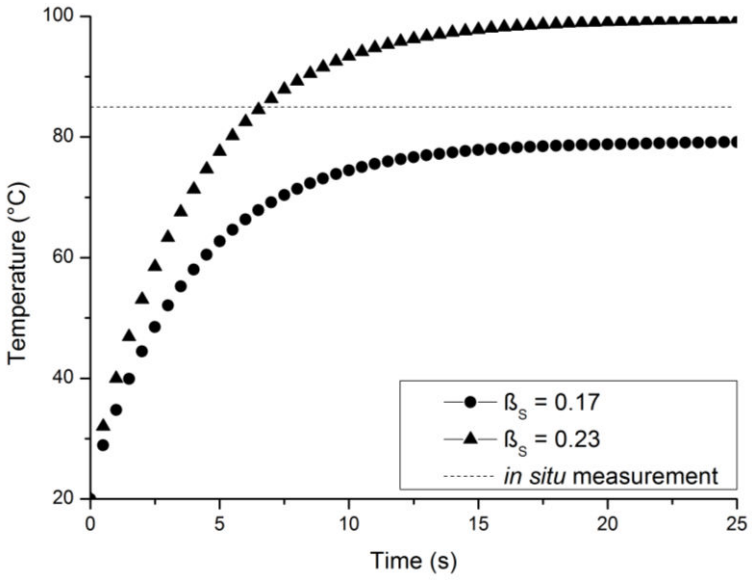

Figure 94: Predicted bottom substrate temperature for different substrate absorbance coefficients.

This *in situ* measurement is in the range of temperature predicted by the model with this sample configuration for a substrate absorbance coefficient ranging between 0.17 and 0.23. This suggests a higher substrate absorbance coefficient than 0.17. However, more detailed investigation is required to restrict the range of values for the substrate absorbance.

***

As a conclusion for this part, the comparison of the microstructural observations and the predicted temperatures of the model has permitted to limit the range of possible values for the absorbance coefficients of the substrate and the silver nanoparticles deposition. It is difficult to give definitive values; both substrate and silver deposition absorbance coefficients range between 0.17 and 0.23. However, this first estimation may be sufficient to allow using the thermal model for further optimization of the deposition process.

5.6 Conclusions

The second part of this thesis was focused on the deposition of silver nanoparticles which could help to design magnesium implants with antibacterial surfaces. Using an additive manufacturing technology, silver nanoparticles are deposited on the surface of the substrate. The deposition follows any geometrical pattern previously designed

by computer-aided design software. After deposition, a laser assisted sintering is processed onto the material.

In a first step of this part, the patterning process parameters have been optimized for controlled deposition. These parameters have been determined using general characteristics of the deposition examined by optical microscopy, profilometry and SEM. The following deposition characteristics have been obtained after this first step:

- The optimization of the deposition process had permitted to obtain a reproducible deposition line of 20 µm width. The thickness of this line ranges between few hundreds of nanometres and one micrometre.
- The optimization of the laser heat treatment of the patterned samples permitted to obtain a homogeneous sintering with surface roughness in nano-scale on the deposition.

On a second step, a microstructural study of the deposition has been carried out to characterize the sintering quality. The interface, as well as the subsurface of the substrate, has also been characterized. Detailed investigations have been carried out on cross sections realized by FIB nano-machining of samples and using different techniques: SEM, TEM and ACOM/ASTAR. The following observations can be pointed out:

- The impact of laser beam velocity, on a range from 0.1 $mm.s^{-1}$ to 0.7 $mm.s^{-1}$, during the sintering process has been carried out by the microstructural observations. It appears that at both velocities, the deposition presents a homogeneous sintering progress through the thickness of the deposition.
- At the surface of the substrate, a sublayer of fine grains with size ranging between 100 nm to 600 nm has been observed. It is suggested that this sublayer results from the recrystallization of a deformed area due to mechanical polishing during sample preparation. This microstructural information provides evidence of the thermal impact of the laser on the substrate.
- The deposition layer was found to have no bounding to the substrate in the studied location. It is suggested that it is coming from the evaporation of the

ink solvents during the sintering process. Thus, a drying time may be required after deposition to improve the bonding of the deposition to the substrate.

The third and last step was to provide a model using COMSOL Multiphysics, to predict the thermal exchange occurring during the laser treatment. Using the previous microstructural characterizations, the input parameters have been adjusted and the predicted temperatures by thermal model have been compared to the previous characterizations.

- On the investigated range, the laser velocity greatly impacts the temperature profile during the sintering process. Modifying this parameter could lead to variable porosity structure of the deposition.
- The model has permitted to show that the thermal impact from the sintering process occurs deep into the substrate. The fine grains sublayer thickness only gives a low limit of the thickness of this thermally affected area.

As a conclusion, this model can provide a basis to investigate the impact of different input parameters. This may be used for further optimization of the functionalization process using different pattern geometries or substrates.

6. Summary and recommendations for future work

6.1 Summary

The present study has been carried out to obtain a framework to design biodegradable devices with antibacterial surfaces for biomedical applications. The final application involves different fields of study: mechanical properties, degradation behavior, surface functionalization, *in vivo* interaction. Thus, depending on the point of view, there are different directions for enhancing properties in view of this application. In the present work, it has been chosen to work from a material point of view. The composition of the alloy has been chosen in accordance with *in vivo* requirements. Then, the material improvement has been carried out following a two steps approach: first, on the bulk and in a second time, on the surface of the material.

The first part of this work was to tailor the bulk microstructure of the selected alloy. To achieve this goal, thermomechanical treatments have been used. After the different thermomechanical processing, the microstructure of the processed samples has been characterized: grain size, intermetallic morphology and texture. Owing to the existing literature, the main mechanisms responsible for the improvement of mechanical and corrosion properties have been identified. Concerning the mechanical properties, the increase of strength can be accounted to different microstructural features like dislocations, twins, grain size and morphology of the intermetallic. Concerning the corrosion behavior, the dispersion and the size of the Mg_2Ca intermetallic appear to be also key parameters to reduce the corrosion rate. Dispersing the Mg_2Ca intermetallic into fine particles permits to avoid a detrimental

galvanic corrosion between the matrix and these particles. In addition to this effect, the finer grain size may also have helped to improve the corrosion resistance. This would be due to the higher density of grain boundaries which would decrease the mismatch between the matrix lattice and the oxide lattice. From the present investigations, ECAP appears as the most efficient thermomechanical process to improve the mechanical and corrosion behavior of the Mg-2wt.%Ca alloy.

The second part of this work was aiming to functionalize the surface. Using an additive manufacturing technology, it is possible to produce a deposition of silver nanoparticles that should provide an antibacterial effect. After optimization of the processing parameters it was possible to produce patterns of continuous lines of silver nanoparticles with a controlled geometry. A thermal treatment by laser has been carried out in the aim to provide cohesion of the deposition and with the substrate. Cross sections on samples after deposition and thermal treatment have allowed characterizing the interface of deposition. The porous microstructure of the deposited layer is characteristic of a partial sintering of the silver nanoparticles. In addition, non-contact areas between the deposition and the substrate suggest a low interaction between the deposited layer and the substrate. It has also been observed that the thermal treatment affects the substrate: a 1 µm sublayer of fine grains has been observed under the surface. For further optimization, a thermal model using COMSOL Multiphysics has been realized. Using this model, it is then possible to predict the thermal effect for different input parameters like the laser power or the velocity of the laser beam. Thus, this model can be used for further improvement of the deposition and more specifically to estimate the interaction between the deposition and the substrate.

6.2 Recommendations for future work

Further refinement of the microstructure

During this work the beneficial impact of the refinement of the microstructure has been shown. Thus, in a future study, it may be worth to investigate the possibilities to decrease grain size and improve the dispersion of the intermetallic particles. In the present work, ECAP was performed at relatively high temperature: 280 °C. This

temperature allowed the sample to recrystallize into fine grains with average size of 2 µm. Decreasing the temperature may lead to a finer microstructure, as for instance, grain size around 1 µm has been reported in a AZ91 magnesium alloy by processing with ECAP at 175 °C [58]. In the present case, at temperatures less than 280 °C the material was broken. A possibility suggested by Mussi [141] is to decrease the temperature step by step along the passes. The improved microstructure at each pass permit to decrease the temperature for the next pass. Another possibility suggested in the literature is to pre-process by extrusion the material before using ECAP [114]. In addition, another beneficial effect that may be obtained by using extrusion before ECAP would be to allow a more dispersed distribution of the intermetallic particles as it has been reported in a magnesium alloy AE21 [198].

Optimization of the deposition

Through the cross section observations, it has been noticed that the deposition was not bounded with the substrate. It has been suggested that during heat treatment by laser, the remains of solvent may have created these gaps. Thus, a drying period using the hot plate at moderate temperature to avoid any microstructural evolution of the material may help to improve the contact of the deposit. In addition, using the thermal simulation established in the present work, laser parameters to obtain different temperature levels and laser interaction times can be determined. For instance, a series of conditions of laser power and velocity can be determined using the simulation. These conditions can be used to find the optimum condition for the adhesion of the deposit.

Biological tests

Preliminary cell viability tests have been performed in collaboration with Pr. J. Gough at the University of Manchester. These tests have been done on the thermomechanically processed samples using a cell culture of human osteoblasts in a culture medium. These first tests have shown no negative effect of the microstructure tailoring on the cell viability. However, these tests were carried out for only 3 days in a controlled environment. Thus, after further optimization of the material with the above recommendations, *in vivo* tests could be carried out on laboratory animals. Indeed, the corrosion behavior between the *in vivo* and *in vitro* environment is different, thus this *in vivo* tests will be needed to allow for better optimization. In

addition, the effect of the silver patterning on degradation, cell viability and adhesion will have to be investigated. In particular, tuning the pattern geometry or using a sublayer between the substrate and the deposition might be of interest in view of the degradable implant applications.

List of bibliography

[1] B. D. Ratner, "Biomaterials science: an interdisciplinary endeavor," in *Biomaterials Science: An Introduction to Materials in Medicine.*: Academic Press, 1997.

[2] D. Gibbons, "Introduction to medical implant materials," in *ASM Handbook - Materials for medical devices.*: ASM International, 2012, vol. 23.

[3] B. D. Ratner, A. S. Hoffman, F. J. Schoen, et al., *Biomaterials science - An introduction to materials in medicine.*: Academic Press, 1997.

[4] L. Matthew, R. J. E. Busam, W. T. Obremskey, "Hardware removal: Indications and expectations.," *Journal of the American*, vol. 14, pp. 113-120, 2006.

[5] M. P. Staiger, A. M. Pietak, J. Huadmai, et al., "Magnesium and its alloys as orthopedic biomaterials: A review," *Biomaterials*, vol. 27, pp. 1728-1734, 2006.

[6] A. Denkena and B. Lucas, "Biocompatible magnesium alloys as absorbable implant materials – Adjusted surface and subsurface properties by machining Processes," *CIRP Annals - Manufacturing Technology*, vol. 56, pp. 113-116, 2007.

[7] J. C. Middleton and A. J. Tipton, "Synthetic biodegradable polymers as orthopedic devices," *Biomaterials*, vol. 21, pp. 2335-2346, 2000.

[8] H.G. Seiler, *Handbook on Toxicity of Inorganic Compounds, 1st ed.*: CRC Press: Boca Raton, 1987.

[9] F. Witte, "The history of biodegradable magnesium implants: A review," *Acta Biomateriala*, vol. 6, pp. 1680-1692, 2010.

[10] S. C. Cowin, A. E. Goodship, J. L. Cunningham, "Bone adaptation," in *Bone Mechanics Handbook, Second Edition.*: Taylor and Francis, 2001, ch. 5.

[11] M. E. Müller, M. Allgöwer, S. M. Perre, *Manual of INTERNAL FIXATION: Techniques Recommended by the Ao-Asif Group.*: Springer Science & Business Media, 1991.

[12] M. M. Avedesian and H. Baker, "Properties of unalloyed magnesium," in *ASM Specialty handbook - Magnesium and Magnesium Alloys.*: ASM International, 1999.

[13] Y. H. An, R. A. Draughn, E. Bonucci, *Mechanical testing of bone and the bone-implant interface.*: CRC Press, 1999.

[14] X.-N. Gu and Y.-F. Zheng, "A review on magnesium alloys as biodegradable materials," *Frontiers of Materials Science in China*, vol. 4, pp. 111-115, 2010.

[15] L. E. Claes, "Mechanical characterization of biodegradable implants," *Clinical Materials*, vol. 10, pp. 41-46, 1992.

[16] H. Wang, Y. Estrin, H. F. Fu, "The effect of pre-processing and grain structure on the bio-corrosion and fatigue resistance of magnesium alloy AZ31," *Advanced Engineering Materials*, vol. 9, pp. 967-972, 2007.

[17] H. Wang, Y. Estrin, Z. Zúberová, "Bio-corrosion of a magnesium alloy with different processing histories," *Materials letters*, vol. 62, pp. 2476-2479, 2008.

[18] D. Song, A.B. Ma, J. Jiang, "Corrosion behavior of equal-channel-angular-pressed pure magnesium in NaCl aqueous solution," *Corrosion Science*, vol. 52, pp. 481-490, 2010.

[19] M. Salahshoor and Y. Guo, "Biodegradable orthopedic magnesium-calcium (mgca) alloys, processing, and corrosion performance," *Materials*, vol. 5, pp. 135-155, 2012.

[20] Z. Pu, G.-L. Song, S. Yang, "Grain refined and basal textured surface produced by burnishing for improved corrosion performance of AZ31B Mg alloy," *Corrosion Science*, vol. 57, pp. 192-201, 2012.

[21] J.L. Clement and P.S. Jarett, "Antibacterial Silver," *Metal-Based Drugs*, vol. 1, pp. 467-482, 1994.

[22] F. Witte, N. Hort, C. Vogt, et al., "Degradable biomaterials based on magnesium corrosion," *Current Opinion in Solid State and Materials Science*, vol. 12, pp. 63-72, 2008.

[23] B. Langelier, X. Wang, S. Esmaeili, "Evolution of precipitation during non-isothermal ageing of an Mg–Ca–Zn alloy with high Ca content," *Materials Science and Engineering: A*, vol. 538, pp. 246-251, 2012.

[24] H. Alemohammad, O. Aminfar, E. Toyserkani, "Morphology and microstructure analysis of nano-silver thin films deposited by laser-assisted maskless microdeposition," *Journal of Micromechanics and Microengineering*, no. 18, 2008.

[25] M.O. Pekguleryuz, "Current developments in wrought magnesium alloys," in *Advances in wrought magnesium alloys - Fundamentals of processing, properties and applications.*: Woodhead Publishing, 2012.

[26] S. K. Sahoo, R. K. Sabat, S. Panda, et al., "Mechanical Property of Pure Magnesium: From Orientation Perspective Pertaining to Deviation from Basal Orientation," *Journal of Materials Engineering and Performance*, vol. 24, pp. 2346-2353, 2015.

[27] M. R. Barnett, "Twinning and the ductility of magnesium alloys Part I: “Tension” twins," *Materials Science and Engineering A*, vol. 464, pp. 1-7, 2007.

[28] S. R. Agnew, J. A. Horton, T. M. Lillo, et al., "Enhanced ductility in strongly textured magnesium produced by equal channel angular processing," *Scripta Materialia*, vol. 50, pp. 377-381, 2004.

[29] J. Koike, R. Ohyama, T. Kobayashi, et al., "Grain-Boundary Sliding in AZ31 Magnesium Alloys at Room Temperature to 523 K," *Materials Transactions*, vol. 44, pp. 445-451, 2003.

[30] S. E. Harandi, M. Mirshahi, S. Koleini, et al., "Effect of Calcium Content on the Microstructure, Hardness and In-Vitro Corrosion Behavior of Biodegradable Mg-Ca Binary Alloy," *Materials Research*, pp. 11-18, 2013.

[31] J. W. Seong and W. J. Kim, "Development of biodegradable Mg–Ca alloy sheets with enhanced strength and corrosion properties through the refinement and uniform dispersion of the Mg2Ca phase by high-ratio differential speed rolling," *Acta Biomaterialia*, vol. 11, pp. 531-542, 2015.

[32] W.-C. Kim, J.-G. Kim, J.-Y. Lee, et al., "Influence of Ca on the corrosion properties of magnesium for biomaterials," *Materials Letters*, pp. 4146-4148, 2008.

[33] Y. S. Jeong and W. J. Kim, "Enhancement of mechanical properties and corrosion resistance of Mg–Ca alloys through microstructural refinement by indirect extrusion," *Corosion Science*, vol. 82, pp. 392-403, 2014.

[34] N. Birbilis, K. D. Ralston, S. Virtanen, "Grain character influences on corrosion of ECAPed pure magnesium," *Corrosion Engineering, Science and Technology*, vol. 45, pp. 224-230, 2010.

[35] M. Alvarez-Lopez, M. D. Pereda, J. A. Del Valle, "Corrosion behaviour of AZ31 magnesium alloy with different grain sizes in simulated biological fluids," *Acta Biomaterialia*, vol. 6, pp. 1763-1771, 2010.

[36] N. N. Aung and W. Zhou, "Effect of grain size and twins on corrosion behaviour of AZ31B magnesium alloy," *Corrosion Science*, vol. 52, pp. 589-594, 2010.

[37] K. U. Kainer, *Magnesium Alloys and Technologies*, John Wiley & Sons, Ed., 2006.

[38] G-.L. Song, R. Mishra, Z.Q. Xu, "Crystallographic orientation and electrochemical activity of AZ31 Mg alloy," *Electrochemistry Communications*, vol. 12, pp. 1009-1012, 2010.

[39] G.-L. Song and Z. Xu, "Crystal orientation and electrochemical corrosion of polycrystalline Mg," *Corrosion Science*, vol. 63, pp. 100-112, 2012.

[40] M. Ben-Haroush, G. Ben-Hamu, D. Eliezer, "The relation between microstructure and corrosion behavior of AZ80 Mg alloy following different extrusion temperatures," *Corrosion Science*, vol. 50, pp. 1766-1778, 2008.

[41] J. D. Loveless, H. Alemohammad, J. Li, et al., "Laser-assisted maskless microdeposition of silver nano-particles on a magnesium substrate," *Materials Letters*, vol. 63, pp. 1397-1400, 2009.

[42] F. Dullien, *Porous Media - Fluid Transport and Pore Structure*, Elsevier, Ed., 2012.

[43] T. G. Lei, J. N. Calata, G.-Q. Lu, "Low-Temperature Sintering of Nanoscale Silver Paste for Attaching Large-Area (>100mm^2) Chips," *IEEE Transaction on Components and packing technology*, vol. 33, pp. 98-104, 2010.

[44] K. Park, D. Seo, J. Lee, "Conductivity of silver paste prepared from nanoparticles," *Colloids and Surfaces A: Physicochemical and Engineering Aspects*, vol. 313-314, pp. 351-354, 2008.

[45] J. R. Greer and R. A. Street, "Thermal cure effects on electrical performance of nanoparticle silver inks," *Acta Materialia*, vol. 55, pp. 6345-6349, 2007.

[46] Z. Z. Fang and H. Wang, "Densification and grain growth during sintering of nanosized particles," *International Materials Reviews*, vol. 53, pp. 326-352, 2008.

[47] E. Toyserkani, A. Khajepour, S. Corbin, *Laser Cladding*, CRC Press, Ed., 2004.

[48] E. Foroozmehr, H. Alemohammad, X. Wan, et al., "Laser-assisted surface patterning of magnesium with silver nanoparticles: synthesis, characterization and modelling," *Journal of Physics D: Applied Physics*, vol. 44, 2011.

[49] E. Jabari, S. Tong, A. Azhari, et al., "Non-planar interconnects in double-sided flexible Cu-PET substrates using a laser-assisted maskless microdeposition process: 3D finite element modeling and experimental analysis," *Optics and Lasers in Engineering*, vol. 54, pp. 117-127, March 2014.

[50] D. A. Kramer, "Magnesium," *2011 Minerals Yearbook*, 2013.

[51] Roskill, Magnesium Metal: Global Industry Markets and Outlook 2012, 2012.

[52] Z. Yang, J. P. Li, J. X. Zhang, et al., "Review on research and development of magnesium alloys," *Acta Metallurgica Sinica (English Letters)*, vol. 21, pp. 313-328, 2008.

[53] I. Polmear, "The light metals," in *Light Alloys (Fourth Edition) - From Traditional Alloys to Nanocrystals.*: Butterworth-Heinemann, 2005.

[54] A. Azushima, R. Kopp, A. Korhonen, et. al., "Severe plastic deformation (SPD) processes for metals," *CIRP Annals - Manufacturing Technology*, vol. 57, pp. 716-735, 2008.

[55] R. Abbaschian, L. Abbaschian, R. Reed-Hill, *Physical metallurgy principles, Fourth edition.*: Wadsworth Publishing Co Inc, 2008.

[56] F. C. Campbel, *Elements of Metallurgy and Engineering Alloys.*: ASM International, 2008.

[57] R. Kaibyshev, M. Barnett, C. Bettles, *Advances in wrought magnesium alloys - Fundamentals of processing, properties and applications*, Woodhead Publishing, Ed., 2012.

[58] M. Mabuchi, H. Iwasaki, K. Higashi, "Low temperature superplasticity of Magnesium Alloys Processed by ECAE," *Materials Science Forum*, vol. 243-245, pp. 547-552, 1997.

[59] Hall E. O., "The deformation and ageing of mild steel: III - Discussion of results," *Proceedings of the Physical Society*, pp. 747-752, 1951.

[60] R. M. Aikin, "The mechanical properties of in-situ composites," *The Journal of The Minerals, Metals & Materials Society*, vol. 49, pp. 35-39, 1997.

[61] C. S. Smith, *Transactions of the Metallurgical Society of AIME*, vol. 175, p. 47, 1948.

[62] NC, "3. The deformed state of metals (II). Structure," *Progress in Materials Science*, vol. 25, pp. 135-271, 1980.

[63] D. Orlov, K.D. Ralston, N. Birbilis, et al., "Enhanced corrosion resistance of Mg alloy ZK60 after processing by integrated extrusion and equal channel angular pressing," *Acta Materialia*, vol. 59, pp. 6176-6186, 2011.

[64] J. F. Nie, "Effects of precipitate shape and orientation on dispersion strengthening in magnesium alloys," *Scripta Materialia*, vol. 48, pp. 1009-1015, 2003.

[65] Polmear I., "Grades and alloys," in *ASM Specialty handbook - Magnesium and Magnesium Alloys.*: ASM International, 1999.

[66] J.-L. Crolet and G. Béranger, "Corrosion en milieu aqueux des métaux et alliages," in *Corrosion et vieillissement: phénomènes et mécanismes.*: Techniques de l'Ingenieur, 1998.

[67] E. E. Stansbury and R. A. Buchanan, *Fundamentals of Electrochemical Corrosion.*: ASM International, 2000.

[68] G. L. Song and A. Atrens, "Corrosion mechanisms of magnesium alloys," *Advanced engineering materials*, vol. 1, pp. 11-33, 1999.

[69] G. Song and A. Atrens, "Understanding magneisum corosion - A framework for improved alloy performance," *Advanced Engineering Materials*, vol. 5, pp. 837-858, 2003.

[70] E. Gali, "Part 1 - Electrochemical fundamentals and active-passive corrosion behaviors," in *Corrosion Resistance of Aluminum and Magnesium Alloys: Understanding, Performance, and Testing.*: Wiley, 2010.

[71] Polmear I., "Magnesium alloys and applications," *Materials Science and Technology*, vol. 10, pp. 1-16, 1994.

[72] G. L. Song, "Corrosion behavior and prevention strategies for magnesium (Mg) alloys," in *Corrosion Prevention of Magnesium Alloys.*: Woodhead Publishing Series, 2013, ch. 1.

[73] P. Kurze, "Corrosion and Corrosion Protection of Magnesium," in *Magnesium - Alloys and Technologies.*: Wiley-VCH, 2004, ch. 13.

[74] Rolled Alloys. rolledalloys.com. [Online]. http://www.rolledalloys.com/technical-resources/blog/pitting-corrosion?blogID=9e7f7bf0-e670-4e25-a5fc-0f9cfd6eb7e3

[75] R.-C. Zeng, J. Zhang, W.-J. Huang, et al., "Review of studies on corrosion of magnesium alloys," *Transactions of nonferrous metals society of China*, vol. 16, pp. 763-771, 2006.

[76] E. Gali, "Part 3 - Properties, use, and performance of magnesium and its alloys," in *Corrosion Resistance of Aluminum and Magnesium Alloys Understanding, Performance.*: Wiley, 2010b.

[77] G. L. Makar and J. Kruger, "Corrosion of magnesium," *International Materials Reviews*, vol. 38, pp. 138-153, 1993.

[78] S. Abela, "Protective Coatings for Magnesium Alloys," in *Magnesium Alloys - Corrosion and Surface Treatments.*: InTech, 2011, ch. 10.

[79] Polmear I., "Magnesium alloys," in *Light Alloys (Fourth Edition) - From Traditional Alloys to Nanocrystals.*: Butterworth-Heinemann, 2005b.

[80] H. Hornberger, S. Virtanen, A.R. Boccaccini, "Biomedical coatings on magnesium alloys – A review," *Acta Biomaterialia*, vol. 8, pp. 2442-2455, 2012.

[81] K. Y. Chiu, M. H. Wong, F. T. Cheng, et al., "Characterization and corrosion studies of fluoride conversion coating on degradable Mg implants," *Surface & Coatings*

Technology, vol. 202, pp. 590-598, 2007.

[82] M. Carboneras, M. C. Garcia-Alonso, M. L. Escudero, "Biodegradation kinetics of modified magnesium-based materials in cell culture medium," *Corrosion Science*, vol. 53, pp. 1433-1439, 2011.

[83] H. M. Wong, K. W.K. Yeung, K. O. Lam, al. et, "A biodegradable polymer-based coating to control the performance of magnesium alloy orthopaedic implants," *Biomaterials*, vol. 31, pp. 2084-2096, 2010.

[84] and Draughn R. A., An Y. H., "Mechanical properties of bone," in *Mechanical testing of bone and the bone-implant interface.*: CRC Press, 1999.

[85] W. Jee and S. Cowin, "Integrated Bone Tissue Physiology: Anatomy and Physiology," in *Bone mechanics handbook - Second edition.*: CRC Press, 2001.

[86] J. B. Park and R. S. Lakes, *An introduction to biomaterials - Second edition.*: Plenum Press, 1992.

[87] B. Cummings, Bone fracture healing process, 2004, Pearson Education, Inc.

[88] W. R. Fordham, S. Redmond, A. Westerland, et al., "Silver as a bactericidal coating for biomedical implants," *Surface & coatings technology*, vol. 253, pp. 52-57, 2014.

[89] R. Marsell and T. A. Einhorn, "The biology of fracture healing," *Injury*, vol. 42, pp. 551-555, 2011.

[90] (2015, Aug.) larapedia.com. [Online]. http://www.larapedia.com/ortopedia_fratture/fratture_i_fattori_che_influenzano_il_consolidamento_delle_fratture.html

[91] M.P. Sealy and Y.B Guo, "Fabrication and Characterization of Surface Texture for Bone Ingrowth by Sequential Laser Peening Biodegradable Orthopedic Magnesium-Calcium Implants," *Journal of Medical Devices*, 2011.

[92] Y. Yun, Z. Dong, D. Yang, et al., "Biodegradable Mg corrosion and osteoblast cell culture studies," *Materials Science and Engineering: C*, vol. 29, pp. 1814-1821, 2009.

[93] N. T. Kirkland, Birbilis, N., "Developments in Mg-based alloys for biomaterials," in *Magnesium Biomaterials - Design, Testing, and Best Practice.*: Springer, 2013.

[94] Standing Committee on the Scientific Evaluation of Dietary Reference Intakes, Food and Nutrition Board, Institute of Medicine, *Dietary Reference Intakes.*: National Academies Press, 1999, vol. 565, DRI for Calcium, Phosphorus, Magnesium, Vitamin D, and Fluoride.

[95] M. Moravej and D. Mantovani, "Biodegradable metals for cardiovascular stent application: interests and new opportunities," *International Journal of Molecular Sciences*, vol. 12, pp. 4250-4270, 2011.

[96] O. Dejean, *Orthopédie, traumatologie.*: Med-Line, 2001.

[97] Hofmann G. O., "Biodegradable implants in traumatology: a review on the state-of-the-art," *Archives of Orthopaedic and Trauma Surgery*, vol. 114, pp. 123-132, 1995.

[98] C. K. Seal, K. Vince, M. A. Hodgson, "Biodegradable Surgical Implants based on Magnesium Alloys - A Review of Current Research," *IOP Conf. Series: Materials Science and Engineering*, vol. 4, 2009.

[99] H. S. Brar, J. Wong, M. V. Manuel, "Investigation of the mechanical and degradation properties of Mg–Sr and Mg–Zn–Sr alloys for use as potential biodegradable implant materials," *Journal of the mechanical behavior of biomedical materials*, vol. 7, pp. 87-95, 2012.

[100] J. Kubásek, D. Vojtěch, J. Lipov, et al., "Structure, mechanical properties, corrosion behavior and cytotoxicity of biodegradable Mg–X (X=Sn, Ga, In) alloys," *Materials Science and Engineering C*, vol. 33, pp. 2421-2432, 2013.

[101] A. L. Boskey, "Bone mineralization," in *Bone Mechanics Handbook - Second Edition.*: CRC Press, 2001.

[102] Z. Li, X. Gu, S. Lou, et al., "The development of binary Mg-Ca alloys for use as biodegradable materials within bone," *Biomaterials*, pp. 1329-1344, 2008.

[103] B. L. Mordike and P. Lukac, "Physical Metallurgy," in *Magnesium Technology - Metallurgy, Design Data, Applications.*: Springer, 2006, ch. 3.

[104] D. J. Zuliani and B. Cloasset, "Magnesium-calcium alloys for debismuthizing lead," US5041160 A, 1991.

[105] P. Vilars and K. Cenzual, Pearson's Crystal Data: Crystal Structure Database for Inorganic Compounds, 2008/09.

[106] J. F. Nie and B. C. Muddle, "Precipitation hardening of Mg-Ca(-Zn) alloys," *Scripta Materiala*, pp. 1475-1481, 1997.

[107] A. Drynda, T. Hassel, R. Hoehn, et al., "Development and biocompatibility of a novel corrodible fluoride-coated magnesium-calcium alloy with improved degradation kinetics and adequate mechanical properties for cardiovascular applications," *Journal of Biomedical Materials Research Part A*, pp. 763-775, 2010.

[108] Y. Murakoshi, K. Kikuchi, M. Katoh, et al., "Fabrication and Property of Degradable Magnesium-Calcium Alloy Composites with Hydroxyapatite," *IFMBE Proceedings*, pp. 1226-1229, 2010.

[109] H.-S. Han, Y. Minghui, H.-K. Seok, et al., "The modification of microstructure to improve the biodegradation and mechanical properties of a biodegradable Mg alloy," *Journal of the Mechanical Behavior of Biomedical Materials*, pp. 54-60, 2013.

[110] M. Furukawa, Z. Horita, M. Nemoto, et al., "Review - Processing of metals by equal-channel angular pressing," *Journal of Materials Science*, pp. 2835-2843, 2001.

[111] R. E. Goforth, K. T. Hartwing, L. R. Cornwell, "Severe Plastic Deformation of Materials by Equal Channel Angular Extrusion (ECAE)," in *Investigations and Applications of Severe Plastic Deformation.*: Kluwer Academic Publishers, 2000.

[112] Y. Iwahashia, Z. Horita, M. Nemoto, et al., "The process of grain refinement in equal-channel angular pressing," *Acta Materiala*, vol. 46, pp. 3317-3331, 1998.

[113] S. Biswas, S. S. Dhinwal, S. Suwas, "Room-temperature equal channel angular extrusion of pure magnesium," *Acta Materiala*, pp. 3247-3261, 2010.

[114] K. Matsubara, Y. Miyahara, Z. Horita, et al., "Developing superplasticity in a magnesium alloy through a combination of extrusion and ECAP," *Acta Materialia*, pp. 3073-3084, 2003.

[115] R. Lapovok, Y. Estrin, M. V. Popov, et al., "Enhanced Superplasticity in a Magnesium Alloy Processed by Equal-Channel Angular Pressing with a Back-Pressure," *Advanced Enginering Materials*, vol. 10, pp. 429-433, 2008.

[116] A. Mussi, J.J. Blandin, L. Salvo, et al., "Resistance to strain-induced damage of an ultrafine-grained magnesium alloy deformed in superplastic conditions," *Acta Materialia*, vol. 54, pp. 3801-3809, 2006.

[117] M. Furukawa, Y. Iwahashi, Z. Horita, et al., "The shearing characteristics associated with equal-channel angular pressing," *Materials Science and Engineering A*, vol. 257, pp. 328-332, 1998.

[118] M. Nemoto, Z. Horita, M. Furukawa, et al., "Microstructural Evolution for Superplasticity Using Equal-Channel Angular Pressing," *Materials Science Forum*, vol. 304-306, pp. 59-66, 1999.

[119] R. B. Figueiredo and T. G. Langdon, "Principles of grain refinement in magnesium alloys processed by equal-channel angular pressing," *Journal of Materials Science*, vol. 44, pp. 4758-4762, 2009.

[120] Y. T. Zhu and T. C. Lowe, "Observations and issues on mechanisms of grain refinement during ECAP process," *Materials Science and Engineering A*, pp. 46-53, 2000.

[121] Z. Horita, K. Matsubara, K. Makii, et al., "A two-step processing route for achieving a superplastic forming capability in dilute magnesium alloys," *Scripta Materialia*, vol. 47, pp. 255-260, 2002.

[122] K. Matsubara, Y. Miyahara, Z. Horita, et al., "Achieving Enhanced Ductility in a Dilute Magnesium Alloy through Severe Plastic Deformation," *Metallurgical and materials transactions A*, vol. 35, pp. 1735-1744, 2004.

[123] B. Beausir, S. Suwas, L. S. Toth, et al., "Analysis of texture evolution in magnesium during equal channel angular extrusion," *Acta Materialia*, vol. 56, pp. 200-214, 2008.

[124] W.J. Kim, S.I. Hong, Y.S. Kim, et al., "Texture development and its effect on mechanical properties of an AZ61 Mg alloy fabricated by equal channel angular pressing," *Acta Materialia*, vol. 51, pp. 3293-3307, 2003.

[125] Y. Yoshida, L. Cisar, S. Kamado, et al., "Effect of Microstructural Factors on Tensile Properties of an ECAE-Processed AZ31 Magnesium Alloy," *Materials Transactions*, vol. 44, pp. 468-475, 2003.

[126] E. Zhang and L. Yang, "Microstructure, mechanical properties and bio-corrosion properties of Mg–Zn–Mn–Ca alloy for biomedical application," *Materials Science and Engineering A*, vol. 497, pp. 111-118, 2008.

[127] Y. Wan, G. Xiong, H. Luo, et al., "Preparation and characterization of a new biomedical magnesium–calcium alloy," *Materials and Design*, vol. 29, pp. 2034-2037, 2008.

[128] N. T. Kirkland, N. Birbilis, J. Walker, et al., "In-vitro dissolution of magnesium–calcium binary alloys: Clarifying the unique role of calcium additions in bioresorbable magnesium implant alloys," *Journal of Biomedical Materials Research Part B: Applied Biomaterials*, pp. 91-100, 2010.

[129] N.T. Kirkland, J. Lespagnol, N. Birbilis, et al., "A survey of bio-corrosion rates of magnesium alloys," *Corrosion science*, pp. 287-291, 2010.

[130] H. R. Bakhsheshi Rad, M. H. Idris, M. R. A. Kadir, et al., "Microstructure analysis and corrosion behavior of biodegradable Mg–Ca," *Materials and Design*, vol. 33, pp. 88-97, 2012.

[131] K. V. Kutniy, I. I. Papirov, M. A. Tikhonovsky, et al., "Influence of grain size on mechanical and corrosion properties of magnesium alloy for medical implants,"

Materialwissenschaft und Werkstofftechnik, vol. 40, pp. 242-246, 2009.

[132] M.H. Idris, H. Jafari, S.E. Harandi, et al., "Characteristics of As-Cast and Forged Biodegradable Mg-Ca Binary Alloy Immersed in Kokubo Simulated Body Fluid," *Advanced Materials Research*, pp. 301-306, 2012.

[133] N.T. Kirkland, N. Birbilis, M.P. Staiger, "Assessing the corrosion of biodegradable magnesium implants: A critical review of current methodologies and their limitations," *Acta Biomaterialia*, pp. 925-936, 2012.

[134] B. M. Kannan and R.K. Singh Raman, "In vitro degradation and mechanical integrity of calcium-containing magnesium alloys in modified-simulated body fluid," *Biomaterials*, pp. 2306-2314, 2008.

[135] W. A. Badawy, N. H. Hilala, M. El-Rabiee, et al., "Electrochemical behavior of Mg and some Mg alloys in aqueous solutions of different pH," *Electrochimica Acta*, vol. 55, no. 6, pp. 1880-1887, 2010.

[136] A. S. Bondarenko and G. A. Ragoisha, *Progress in Chemometrics Research*, Pomerantsev A. L., Ed. New York: Nova Science Publishers, 2005, The program is available online at http://www.abc.chemistry.bsu.by/vi/analyser/.

[137] W. S. Rasband. (1997-2015) ImageJ. [Online]. http://imagej.nih.gov/ij/

[138] ASTM, "General Intercept Procedures," in *Standard Test Methods for Determining Average Grain Size.*, 2013.

[139] The Open University. (2010) [Online]. http://core.materials.ac.uk/search/detail.php?id=3270

[140] L. Dupuy, "Comportement mécanique d'un alliage d'aluminium hyper-déformé," 2000.

[141] A. Mussi, "Affinage de la microstructure et amélioration des propriétés mécaniques d'un alliage de magnésium par hyper-déformations," 2003.

[142] S. E. Harandi, M. Mirshahi, S. Koleini, et al., "Effect of Calcium Content on the Microstructure, Hardness and In-Vitro Corrosion Behavior of Biodegradable Mg-Ca Binary Alloy," *Materials Research*, pp. 11-18, 2013.

[143] Y.N. Wang and J.C. Huang, "The role of twinning and untwinning in yielding behavior in hot-extruded Mg–Al–Zn alloy," *Acta Materialia*, pp. 897-905, 2007.

[144] N.T. Kirkland, M.P. Staiger, D. Nisbet, et al., "Performance-driven Design of Biocompatible Mg Alloys," *Journal of the Minerals, Metals & Materials Society*, pp. 28-34, 2011.

[145] Y. Zong, G. Yuan, X. Zhang, et al., "Comparison of biodegradable behaviors of AZ31 and Mg–Nd–Zn–Zr alloys in Hank's," *Materials Science and Engineering B*, pp. 395-401, 2012.

[146] M. Anik and G. Celikten, "Analysis of the electrochemical reaction behavior of alloy AZ91 by EIS technique in H3PO4/KOH buVered K2SO4 solutions," *Corrosion Science*, vol. 49, no. 4, pp. 1878-1894, 2007.

[147] G. Baril, G. Galicia, C. Deslouis, et al., "An Impedance Investigation of the Mechanism of Pure Magnesium Corrosion in Sodium Sulfate Solutions," *Journal of The Electrochemical Society*, vol. 154, no. 2, pp. C108-C113, 2007.

[148] Z. Wen, C. Wu, C. Dai, et al., "Corrosion behaviors of Mg and its alloys with different Al contents in a modified simulated body fluid," *Journal of Alloys and Compounds*, pp. 392-399, 2009.

[149] R. Pinto, M. G. S. Ferreira, M. J. Carmezim, et al., "The corrosion behaviour of rare-earth containing magnesium alloys in borate buffer solution," *Electrochimica Acta*, vol. 56, pp. 1535-1545, 2011.

[150] X.N. Gu, N. Li, W.R. Zhou, et al., "Corrosion resistance and surface biocompatibility of a microarc oxidation coating on a Mg–Ca alloy," *Acta Biomaterialia*, pp. 1880-1889, 2011.

[151] J. Eckert, S. Scudino, M. Stoica, et al., "Mechanical Engineering Properties of CMAs," in *Complex Metallic Alloys: Fundamentals and Applications.*: Wiley-VCH, 2011, p. 274.

[152] C. W. Chung, R. G. Ding, Y. L. Chiu, et al., "Effect of ECAP on microstructure and mechanical properties of cast AZ91 magnesium alloy," *Journal of Physics: Conference Series*, vol. 241, pp. 1-4, 2010.

[153] M. Y. Zheng, X. G. Qiao, S. W. Xu, et al., "In-situ quasicrystal-reinforced magnesium matrix composite processed by equal channel angular extrusion (ECAE)," *Journal of Material Science*, vol. 40, pp. 2587-2590, 2005.

[154] Y. Watanabe, P.D. Sequeira, O. Sitdikov, et al., "Effect of processing route on microstructure and texture development in ECAP of Al-Ti alloy.," *Materials Science Forum*, vol. 561-565, pp. 251-254, 2007.

[155] K. Oh-ishi, Y. Hashi, A. Sadakata, et al., "Microstructural control of an Al-Mg-Si alloy using Equal-Channel Angular Pression," *Materials Science Forum*, pp. 333-338, 2002.

[156] M. Zha, Y. Li, R. H. Mathiesen, et al., "Dispersion of soft Bi particles and grain refinement of matrix in an Al–Bi alloy by equal channel angular pressing," *Journal of Alloys and Compounds*, vol. 605, pp. 131-136, 2014.

[157] G. Min, H. Cui, Q. Lu, et al., "Grain Refinement and Dispersion Precipitation of I-Phase in Mg-Zn-Y Alloy Processed by ECAP," *Materials Science Forum*, vol. 667-669, pp. 593-598, 2010.

[158] M. Barnett, M. R. Barnett, C. Betles, "Twinning and its role in wrought magnesium alloys," in *Advances in wrought magnesium alloys - Fundamentals of processing, properties and applications*, Woodhead Publishing, Ed., 2012.

[159] R. G. Sambasiva and Y. V. R. K. Prasad, "Grain boundary strengthening in strongly textured magnesium produced by hot rolling," *Metallurgical Transactions A*, vol. 13, 19822219-2226.

[160] P. Haden, I. L. Dillamore, D. J. Stratford, "Texture control and the yield anisotropy of plane strain magnesium extrusion," *Texture*, vol. 1, pp. 17-29, 1972.

[161] Y. Uematsu, K. Tokaji, M. Kamakura, et al., "Effect of extrusion conditions on grain refinement and fatigue behaviour in magnesium alloys," *Materials Science and Engineering A*, vol. 434, pp. 131-140, 2006.

[162] S. R. Agnew, M. H. Yo, C. N. Tome, "Application of texture simulation to understanding mechanical behavior of Mg and solid solution alloys containng Li or Y," *Acta Materialia*, vol. 49, pp. 4277-4289, 2001.

[163] T. Al-Samman and G. Gottstein, "Dynamic recrystallization during high temperature deformation of magnesium," *Materials Science and Engineering A*, vol. 490, pp. 411-420, 2008.

[164] W. M. Gan, M. Y. Zheng, H. Chang, et al., "Microstructure and tensile property of the ECAPed pure magnesium," *Journal of Alloys and Compounds*, vol. 470, pp. 256-262, 2009.

[165] A. Trampuz and A. F. Widmer, "Infections associated with orthopedic implants," *Current Opinion in Infectious Diseases*, vol. 19, pp. 349-356, 2006.

[166] P. Zhang, Z. Zhang, W. Li, "Antibacterial TiO2 Coating Incorporating Silver Nanoparticles by Microarc Oxidation and Ion Implantation," *Journal of Nanomaterials*, 2013.

[167] L. Zhao, P. K. Chu, Y. Zhang, et al., "Antibacterial coatings on titanium implants," *Journal of Biomedical Materials Research Part B: Applied Biomaterials*, vol. 91B, pp. 470-480, 2009.

[168] E. M., Schoenfisch, M. H. Hetrick, "Reducing implant-related infections: active release strategies," *Chemical Society Reviews*, vol. 35, pp. 780-789, 2006.

[169] J. S. Kim, E. Kuk, K. N. Yu, et al., "Antimicrobial effects of silver nanoparticles," *Nanomedicine: Nanotechnology, Biology and Medicine*, vol. 3, pp. 95-101, 2007.

[170] D. Lee, R. E. Cohen, M. F. Rubner, "Antibacterial properties of Ag nanoparticle loaded multilayers and formation of magnetically directed antibacterial microparticles," *Langmuir*, vol. 21, pp. 9651-9659, 2005.

[171] M. Bosetti, A. Masse, E. Tobin, et al., "Silver coated materials for external fixation devices: in vitro biocompatibility and genotoxicity," *Biomaterials*, vol. 23, pp. 887-892, 2002.

[172] M. Lihe, W. Yulin, W. Yizao, et al., "Corrosion Resistance of Ag-ion Implanted Mg-Ca-Zn Alloys in SBF," *Rare Metal Materials and Engineering*, vol. 39, pp. 2075-2078, 2010.

[173] H. Zhao and J. Cui, "Electroless plating of silver on AZ31 magnesium alloy substrate," *Surface and Coatings Technology*, vol. 201, pp. 4512-4517, 2007.

[174] A. Ewald, S.K. Glückermann, R. Thull, et al., "Antimicrobial titanium/silver PVD coatings on titanium," *BioMedical Engineering OnLine*, vol. 5, 2006.

[175] J. M. Schakenraad, "Biology, biochemestry, and medecine - Some background concepts," in *Biomaterials science - An introduction to materials in medecine.*: Elsevier, 1996, ch. 3.

[176] Eglin D., Rohde K., Roach P., "Modern biomaterials: a review - Bulk properties and implications of surface modifications," *Journal of Materials Science: Materials in Medicine*, vol. 18, pp. 1263-1277, 2007.

[177] A. I. Teixeira, G. A. McKie, J. D. Foley, et al., "The effect of environmental factors on the response of human corneal epithelial cells to nanoscale substrate topography," *Biomaterials*, vol. 27, pp. 3945-3954, 2006.

[178] A. B. Novaes, S. L. S. De Souza, R. R. M. De Barros, et al., "Influence of Implant Surfaces on Osseointegration," *Brazilian Dental Journal*, vol. 21, pp. 471-481, 2010.

[179] A. Cunha, "Multiscale Femtosecond Laser Surface Texturing of Titanium and Titanium Alloys for Dental and Orthopaedic Implants," PhD thesis 2015.

[180] S. Puckett, R. Pareta, T. J. Webster, "Nano rough micron patterned titanium for directing osteoblast morphology and adhesion," *Internation Journal of Nanomedecine*, vol. 3, pp. 229-241, 2008.

[181] X. Li, J. Huang, M. J. Edirisinghe, "Novel patterning of nanobioceramics template-assisted electrohydrodynamic atomization spraying," *Journal of the Royal Society Interface*, vol. 5, pp. 253-257, 2008.

[182] G. Munir, G. Koller, L. Di Silvio, et al., "The pathway to intelligent implants: osteoblast response to nano silicon-doped hydroxyapatite patterning," *Journal of the Royal Society Interface*, vol. 8, pp. 678-688, 2011.

[183] M. Zenou, O. Ermak, A. Saar, et al., "Laser sintering of copper nanoparticles," *Journal of Physics D: Applied Physics*, vol. 47, 2014.

[184] The University of Alabama. [Online]. http://www.me.ua.edu/PMRF/dceducational.htm

[185] E. F. Rauch and M. Véron, "Automated crystal orientation and phase mapping in TEM," *Materials Characterization*, vol. 98, pp. 1-9, 2014.

[186] K. Lu, W. Li, B. Chen, "Sintering of Porous Materials," in *Sintering - Mechanisms of Convention, Nanodensification and Field, Assisted Processes*, R. Castro and K. Van Benthem, Eds.: Springer, 2013.

[187] W. F. Gale and T. C. Totemeier, *Smithells Metals Reference Book*, Butterworth-Heinemann, Ed., 2003.

[188] H. Pan, F. Pan, R. Yang, et al., "Thermal and electrical conductivity of binary magnesium alloys," *Journal of Materials Science*, vol. 49, pp. 2107-3124, 2014.

[189] E. D. Palik, *Handbook of Optical Constants of Solids II*, Academic Press, Ed., 1991.

[190] W. E. Forsythe, *Smithsonian physical tables. 9th rev. ed.*, Smithsonian Institution, Ed., 1964.

[191] X. Cao, M. Jahazi, J. P. Immrigeon, et al., "A review of laser welding techniques for magnesium alloys," *Journal of Materials Processing Technology*, vol. 171, pp. 188-204, 2006.

[192] J. F. Shackelford and W. Alexander, *CRC Materials Science and Engineering Handbook, Third Edition.*: CRC Press 2000, 2000.

[193] F. Cernuschi, S. Ahmaniemi, P. Vuoristo, et al., "Modelling of thermal conductivity of porous materials: application to thick thermal barrier coatings," *Journal of the European Ceramic Society*, vol. 24, pp. 2657-2667, 2004.

[194] M. S. Brown and C. B. Arnold, "Fundamentals of Laser-Material Interaction and Application to Multiscale Surface Modification," in *Laser Precision Microfabrication.*: Springer Series in Materials Science , 2010.

[195] H. E. Bennett, J. M. Bennett, E. J. Ashley, et al., "Verification of the Anomalous-Skin-Effect Theory for Silver in the Infrared," *Physical Review*, vol. 165, pp. 755-764, 1968.

[196] K.-S. Kim, Y. Kim, S.-B. Jung, "Microstructure and adhesion characteristics of a silver nanopaste screen-printed on Si substrate," *Nanoscale Research Letters*, vol. 7, pp. 1-6, 2012.

[197] O. Sitdikov and R. Kaibyshev, "Dynamic recrystallization in pure magneisum," *Materials Transactions*, vol. 42, pp. 1928-1937, 2001.

[198] P. Minarik, R. Kral, M. Janecek, "Effect of ECAP processing on corrosion resistance of AE21 and AE42 magnesium alloys," *Applied Surface Science*, vol. 281, pp. 44-48, 2013.

[199] B.A. Shaw, R.C. Wolfe, et al., "Corrosion of Magnesium and Magnesium-Base Alloys," in *ASM Handbook - Corrosion: Materials.*: ASM International, 2005, vol. 13B.